

Self assembled nano-structures of Pb on Si(111) studied by SPA-LEED: Quantum Size
Effect driven Pb islands and the “Devil’s Staircase”

by

Michael Keith Yakes

A dissertation submitted to the graduate faculty
in partial fulfillment of the requirements for the degree of

DOCTOR OF PHILOSOPHY

Major: Condensed Matter Physics

Program of Study Committee:
Michael C. Tringides, Major Professor
David C. Johnston
Joerg Schmalian
Steve Kawaler
Rohit Trivedi

Iowa State University
Ames, Iowa
2006

Copyright © Michael Keith Yakes, 2006. All rights reserved.

UMI Number: 3243839

Copyright 2006 by
Yakes, Michael Keith

All rights reserved.

UMI[®]

UMI Microform 3243839

Copyright 2007 by ProQuest Information and Learning Company.
All rights reserved. This microform edition is protected against
unauthorized copying under Title 17, United States Code.

ProQuest Information and Learning Company
300 North Zeeb Road
P.O. Box 1346
Ann Arbor, MI 48106-1346

TABLE OF CONTENTS

CHAPTER 1: INTRODUCTION	1
CHAPTER 2: EXPERIMENTAL DETAILS	15
PART I: DEVILS STAIRCASE OF LINEAR PHASES ON PB/SI(111)	21
CHAPTER 3: SELF-ORGANIZATION AT FINITE TEMPERATURES OF THE DEVIL'S STAIRCASE IN PB/SI(111)	22
CHAPTER 4: PHASE DIAGRAM OF PB/SI(111) FOR $1.2 \text{ ML} < \theta < 1.33 \text{ ML}$	42
PART II: PROPERTIES OF QSE ISLANDS GROWN ON SI(111) SURFACES WITH METAL ADSORBATES	65
CHAPTER 5: COVERAGE DEPENDENT ANISOTROPY IN FCC STACKING SEQUENCE OF PB ISLANDS GROWN ON SI(111)-PB($\sqrt{3} \times \sqrt{3}$)- α PHASE	66
CHAPTER 6: DEPENDENCE OF RELATIVE ROTATION ON COVERAGE OF PB OVERLAYERS ON SI(111)-PB($\sqrt{3} \times \sqrt{3}$)- α PHASE	79
CHAPTER 7: UNUSUAL TEMPERATURE STABILITY OF PB NANOWIRES GROWN ON SI(111)-IN(4x1) PHASE	101
CHAPTER 8: CONCLUSIONS	115
ACKNOWLEDGMENTS	117

CHAPTER 1: INTRODUCTION

Nanotechnology refers to any device fabrication which has size on the order of nanometers (10^{-9} meters). With the electronics industry focused on continuing the miniaturization of everyday tools, electronic components are becoming smaller and smaller. In recent years, nanotechnology has become one of the most important and visible technological terms in science. For example, in his 2006 State of the Union address, President Bush proposed the American Competitiveness Initiative which called for a \$50 billion increase in nanotechnology research.[1] Included in this budget proposal was a doubling of the budget for the National Science Foundation (NSF), the Department of Energy's Office of Science, and the National Institute for Standards and Technology (NIST). These agencies are all cited as world leaders in nanotechnology research. A major question is why are people so interested, and more importantly willing to invest so much money in nanotechnology?

Simply put, when the size of a system is reduced to the atomic scale a variety of interesting new properties can be revealed which do not exist in larger systems. As the size of an object approaches the nanoscale, the description of crystal structures by classical methods begins to break down, and many device characteristics begin to be governed by quantum effects. One class of devices which have many potential interesting technological applications is called quantum dots. Quantum Dots (QDs) are bulk crystalline structures whose sizes approach a few thousand atoms and are confined in three dimensions. In addition to their small size, QDs show a variety of interesting quantum effects, including discrete energy levels and interdot coupling that could allow for their potential applications in lasers,[2] sensors,[3] detectors,[3] and quantum computing.[4] The small size and novel features of these structures offer many opportunities for new technologies.

To be ideally suited for nanoelectronic applications, the size distribution of QDs must be very narrow, because the electronic properties for QDs on a surface are strongly dependent on their size. One method for growing uniform size nanostructures is lithography. In a typical lithographic technique, a pattern is externally created on a surface by selectively

removing material from certain locations on a crystal thus resulting in structures of a known size on the surface. These methods allow for exceptional control of dot size, spacing, and position; however, QDs created by lithographic techniques are often damaged, have high concentrations of defects, or have surface electronic states which make them unsuitable for many device applications.

In heteroepitaxial growth, strain is often introduced at the interface between the substrate and the overlayer due to a mismatch in the lattice constant of the two crystal structures. This strain is usually relieved by the formation of small crystallites (islands) on the surface instead of smooth overlayers. In many systems it is energetically favorable to have one or more strained layers of the overlayer separating the substrate and the islands, resulting in a hybrid growth mode usually referred to as the Stranski-Kratonov (SK) growth mode.[6] Self-assembled QDs grown in the SK growth mode, as described previously, have far less defects than QDs created by lithographic techniques; however, it is far more difficult to control the QD size, shape, and spacing distributions.[6] Due to the importance of these physical quantities, a great deal of research has been performed to try to improve the uniformity of the size, shape, and spacing distributions of self-assembled quantum dots.[7,8]

To achieve maximum uniformity of the QDs, a number of growth parameters can be adjusted including the amount of QD material put on the surface, the flux of incoming atoms, growth temperature, and composition of the deposited layers.[9] To improve results, self-assembly techniques can be combined with lithographic techniques to improve the distribution of the QDs.[10] For example: lithography can be used to create uniformly spaced defects (such as holes) on the substrate, and then these holes can act as preferred nucleation sites for the self-assembled QDs.[11] Another avenue to improve the uniformity of self-assembled nanostructures is to grow islands on patterned substrates.

Whenever a crystal is cleaved exposing a surface, the atomic structure on the surface may rearrange in order to minimize the energy of the exposed surface. There are two general types of atomic rearrangement, relaxation and reconstruction. In relaxation the topmost layer has the same structure as the bulk crystal; however, there is usually a change in the interlayer

spacing at the surface. When a surface reconstructs the atomic structure on the surface rearranges to minimize the energy, which changes the morphology on the surface layer with respect to the bulk. One of the most famous examples of surface reconstruction, the 7×7 reconstruction, is shown in Figure 1. On many surfaces a variety of different structures can be induced by adding an additional amount of a material onto a surface in the appropriate conditions. These surface adsorbate structures can act as preferred nucleation sites for island growth on a surface or can be used to alter the growth morphologies of the grown islands.[12] As such, it is very important to learn how to control the morphologies of these reconstructions to potentially create “designer” self-assembled surfaces to be used as templates for nanostructure growth.

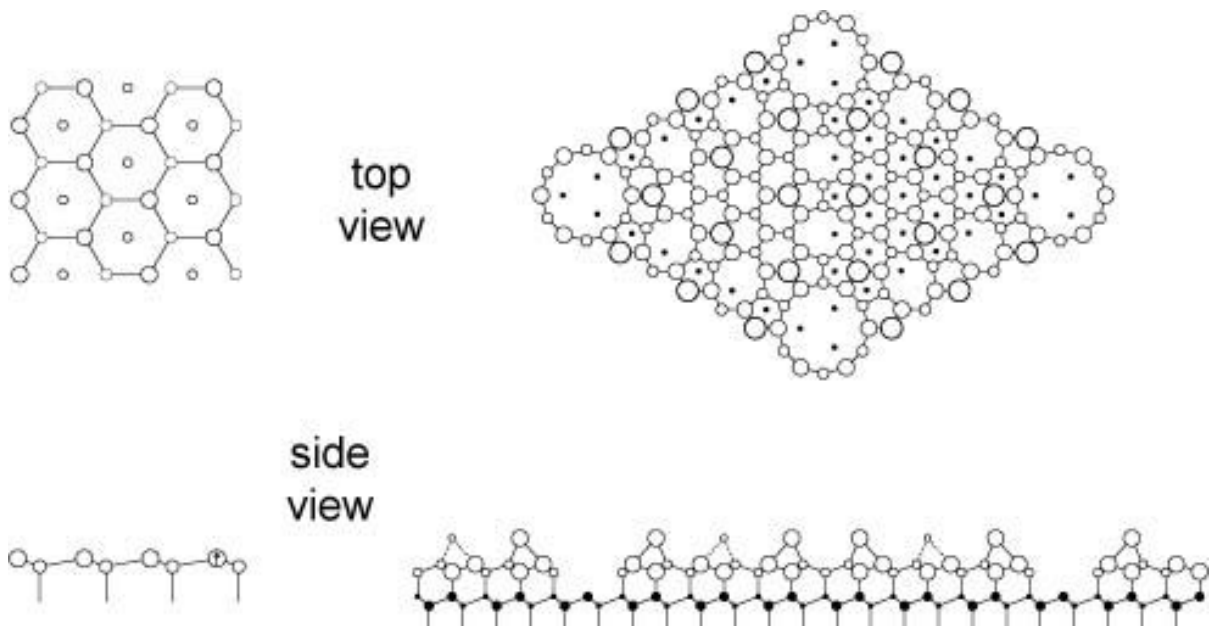


Figure 1: Si(111) 7×7 reconstruction. The regular periodicity of the bulk is replaced on the surface by a new structure which minimizes the surface energy. Figure taken from [13]

To accurately characterize the structure of surfaces it is often beneficial to use complimentary techniques in order to get a full picture of the surface. Usually one technique involves some form of microscopy, for this work the microscope is the scanning tunneling microscope (STM). Other examples of microscopy techniques which are commonly found in

surface science labs are Atomic Force Microscopy (AFM), Scanning Electron Microscopy (SEM), Transmission Electron Microscopy (TEM), or Low Energy Electron Microscopy (LEEM). These techniques provide images of what the surface morphology looks like in real space. When combined with microscopy, a statistical probe such as Low Energy Electron Diffraction (LEED) may be used which gives accurate statistics over macroscopic distances. Other common statistical probes include Surface X-ray Diffraction (XRD) and Reflection High Energy Electron Diffraction (RHEED). When combined, microscopy and statistical probes are a powerful tool to examine surface structures on both local and global scales.

The STM has become a workhorse of many world class surface physics laboratories, and it has the highest resolution of any microscopy technique currently available. The STM contains an atomically sharp, conductive tip. By moving the tip very close to a sample and creating a potential difference between the tip and a conductive sample, a current will be induced between the tip and the sample. A current passes through the vacuum between the tip and sample by quantum tunneling, and is therefore exponentially sensitive to the distance between the tip and the sample. Piezoelectric crystals can be used to adjust the sample position across a surface, mapping out the density of states of a surface with atomic level resolution. The STM has many advantages for surface science research, most notably atomic scale resolution, but it is limited to studying metal and semiconductor surfaces and is difficult to get accurate statistics over large length scales with the STM.[14]

To get additional information over macroscopic surfaces we can use a statistical probe like Low Energy Electron Diffraction. In LEED an electron gun is used to send a beam of low energy (typically 10-200 eV) electrons toward a sample. Since the mean free path of low energy electrons is similar to the atomic spacing in a crystal, the electrons preferentially interact with the atoms on the crystal surface. The wavelength of electrons is also similar to the atomic spacing of the crystal, meaning that they will diffract from the crystal surface. LEED can be used to get very accurate measurements of a crystal surface over macroscopic distances (~0.5 mm). One drawback to LEED is the difficulty of interpreting the diffraction pattern. Unlike x-ray diffraction where the diffraction pattern can

be adequately interpreted using the kinematic (single-scattering) approximation, in order to accurately determine a LEED pattern requires a full dynamic (multiple scattering) theory. This theory necessitates a good idea of the surface structure before analysis in order to get the most accurate results.

Due to its drawbacks, often LEED is used in surface science labs solely to determine the quality of the long range order on a crystal in situ. In laboratories that want to use LEED for more quantitative research, higher resolution is necessary than is available in most conventional LEED systems. To improve the resolution one technique that can be used is spot profile analysis LEED (SPA-LEED). In a SPA-LEED system octopole electric fields are used to deflect the incoming and outgoing electron beams, such that one small piece of reciprocal space is directed toward a high resolution detector. By adjusting the electric fields with a computer, it is possible to probe a large fraction of reciprocal space. The high resolution allows the quantitative spot profile to be investigated as well as the spot position and peak intensity. The spot profiles contain additional information of the structure of a surface not often available with conventional LEED including information on steps, terraces and defects. This information also does not generally require full dynamic calculations in order to extract meaningful results.[15]

Self-assembled nanostructures of Pb on Si(111) can be grown using molecular beam epitaxy (MBE). In MBE, a gas of some material (in this case Pb) is deposited onto a surface from an evaporated source of atoms. This insures uniform deposition of atoms over the whole surface. For materials such as Pb which have a high vapor pressure and low melting point a Knudsen cell can be used to control the beam of atoms. The vapor pressure is very sensitive to temperature so by heating the liquid Pb in a radiation shielded crucible a well controlled uniform flux of atoms can be directed toward the sample through a small opening. By controlling features of this growth such as the total amount deposited, temperature of the surface, and the rate of deposition, different configurations of atoms can be grown on the surface. Pb deposited on Si(111) and adsorbate covered Si(111) has attracted a great deal of attention due to the novel physics discovered there.

This dissertation primarily focuses on two interesting features of this system. In Part I of the dissertation, the focus is on the devil's staircase of linear phases present when the total surface coverage of Pb is 1.2-1.33 ML (1 ML=the amount of lead with bulk structure necessary to cover a surface with one atomic layer of Pb atoms). Part II discusses various features, such as the morphology and temperature dependence, of Pb islands grown on different metal induced reconstructions of the Si(111) surface. These islands show special properties, known as quantum size effects (QSE), that are a manifestation of physics only observed at the nanoscale.

The Devil's Staircase (DS) is one of the outstanding phase diagrams in theoretical physics. Generally, the DS is observed in systems which have two competing interactions. A useful example system is a one-dimensional gas of electrons confined to a lattice. The long ranged repulsive interactions between the electrons compete with the lattice potential induced by the substrate which limits the possible distance that the electrons can be separated.[16] Depending on the coverage of electrons, which is defined as the total number of electrons divided by the number of lattice sites, an infinite number of patterns can formed which minimize the energy at zero temperature. For any coverage, a pattern will form which contains rational number combinations of electrons and lattice sites.

An example phase is shown in Figure 2. This phase has coverage $\theta=3/7$. The minimum in energy occurs when the electrons are either two or three lattice sites apart, in the repeating pattern shown on the diagram. For a general DS phase the configuration of atoms within the unit cell must follow the DS rules which minimize the total energy within each unit cell. The addition or removal of a single electron will cause the entire lattice to reorganize such that the energy is again minimized.

The DS has been a challenge to realize experimentally due to the difficulty of observing many different phases within a narrow coverage interval. However, in the Pb/Si(111) system over 15 distinct phases can be observed with STM and SPA-LEED. Instead of patterns of electrons and holes as in the electron lattice gas case, now the DS contains linear combinations of two generating phases of Pb. The "hole" phase is the $\sqrt{7} \times$

$\sqrt{3}$ phase which has 6 Pb atoms per unit cell of area 5 times the Si(111) unit cell, giving a coverage of $\theta=6/5$ ML. The “occupied” phase is the $\sqrt{3} \times \sqrt{3}$ phase which has 4 Pb atoms per unit cell of area 3 times the Si(111) unit cell, giving a coverage of $\theta=4/3$ ML. Both the $\sqrt{7} \times \sqrt{3}$ and $\sqrt{3} \times \sqrt{3}$ phases form chains of cells aligned along the [112] direction creating patterns of stripes on the surface. DS phases are formed of linear combinations of these stripes.

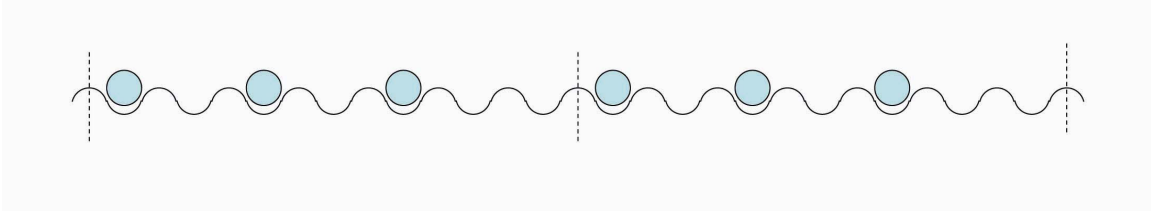


Figure 2: Illustration of DS phase with coverage $\theta=3/7$. The lattice confines the electrons to be integer number of lattice spacing apart. DS rules determine the configuration with the energy minimum shown here.

Figure 3 shows the origin of the name DS. This figure shows the chemical potential vs. coverage (μ vs. θ) calculated stability curve for both the lattice gas of electrons (black) and the new Pb/Si(111) DS (red). The curves appear fractal like, and the length of each “stair” is inversely proportional to the length of the unit cell for each phase. The differences between the lattice gas curve and the Pb/Si(111) curve arise from the possible spacing allowed by each system. While in the lattice gas the separation between atoms is any integer, for the Pb/Si(111) system the separation must be linear combinations of 3 and 5 due to the size of the basis unit cells along the [110] direction which limits the possible sizes for the full unit cells at a given coverage. Since the length of each stair $\Delta\mu$ is proportional to the size of the unit cell, phases where the size of the unit cell changes in the two systems will have different stair lengths.[17]

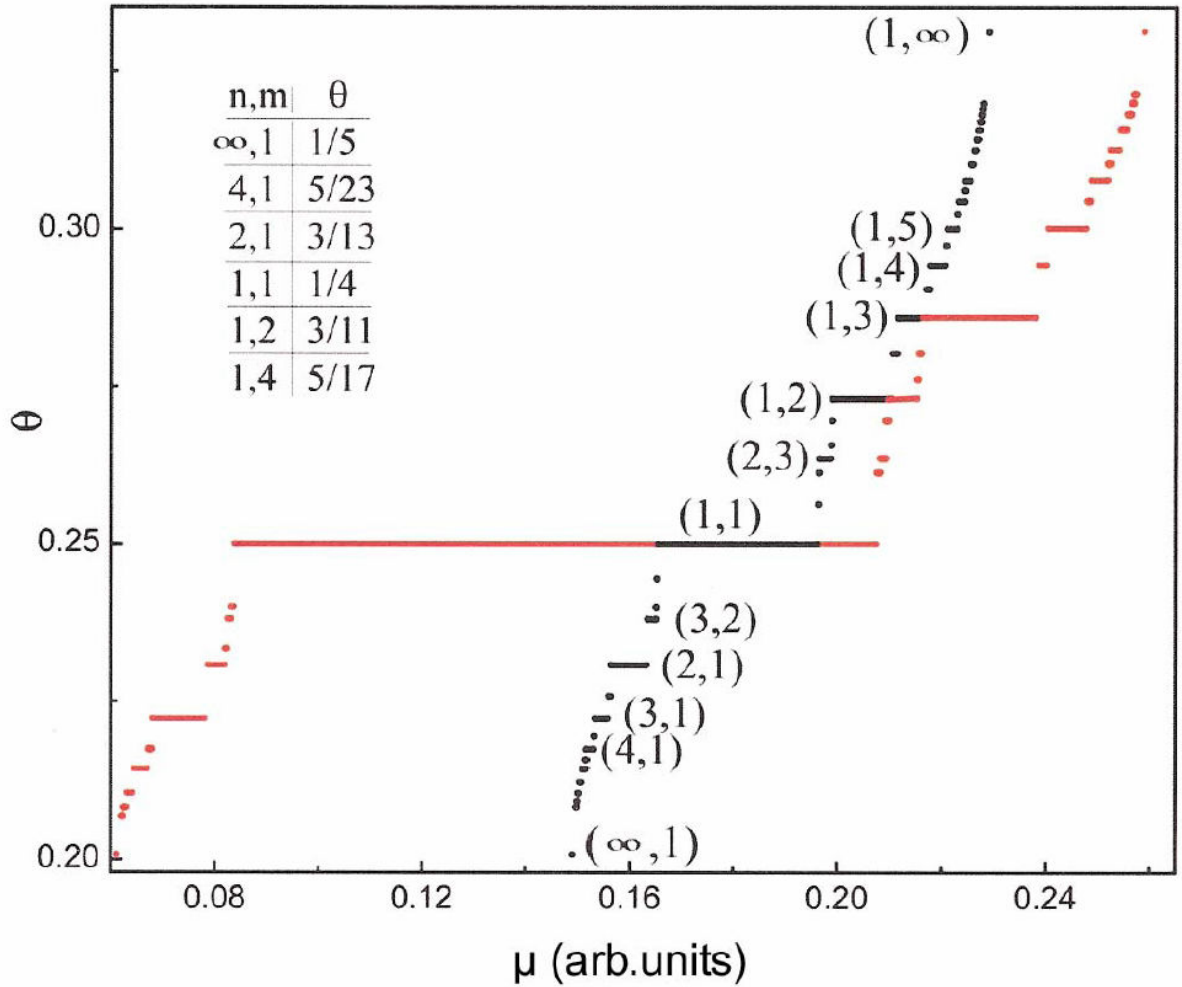


Figure 3: Comparison of the electron gas (red) and Pb/Si(111) DS (black) for the coverage region $1/5 < \theta < 1/3$. The change in the lengths of the stairs in the staircase is due to differences in the unit cell size for each coverage in each system. Figure taken from Ref.[17].

Very surprisingly, we found that with a small deposition of Pb, $\Delta\theta \sim 0.006$ ML, the phases will reorganize from one DS phase to the next, even for temperatures as low as 120K. This requires an extraordinary amount of atom reorganization, as illustrated in figure 4. In this schematic the dense $\sqrt{3} \times \sqrt{3}$ cells are represented by the thin dark black lines while the less dense $\sqrt{7} \times \sqrt{3}$ cells are represented by the thicker light blocks. The addition of just a small amount of lead causes the entire surface to reorganize in a matter of seconds, meaning nearly every atom on the surface needs to change position collectively to reach the energy minimum, including atoms which are large distances away from any incoming atom.

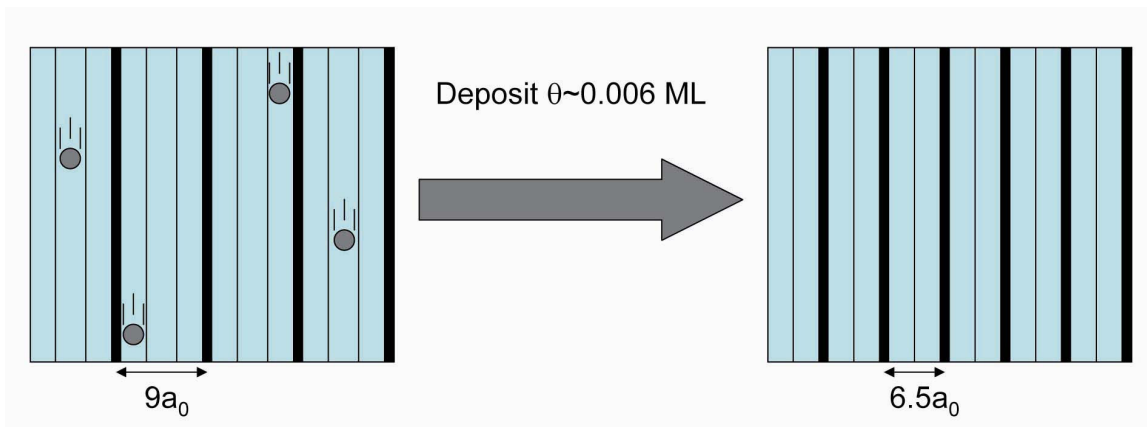


Figure 4: Illustration of global surface reorganization with minute changes in coverage. The (3,1) phase (left) reorganizes to the (2,1) phase with deposition of less than 0.1 ML coverage at 120 K in less than 5 minutes. This illustrates that a high degree of collective surface reorganization is possible even at low temperatures.

A focal point of the research in this thesis is to map out the phase diagram of the DS, something which is important for connecting with the theoretical models. However, unlike the electron gas sample, the two dimensionality and threefold symmetry of the Si(111) substrate introduce additional complexities into the Pb/Si(111) system. In addition to the DS the phase diagram includes a family of hexagonal phases, a meandering striped phase, and two possible configurations of each type of DS unit cell. This presents a challenge to develop a theoretical justification, for all of the features of the phase diagram and there are still many open questions and physics left to be explored in this system.

The second part of this thesis focuses on many properties of self assembled quantum dots of Pb grown on metal induced Si(111) reconstructions. As I alluded to earlier, typically epitaxially grown thin metal films form on substrates in three different morphologies as illustrated in figure 5. If the deposited atoms prefer to bond to the surface than to each other it will show layer by layer growth. If the atoms prefer to bond to each other rather than the substrate, island or Volmer-Weber growth mode will be observed. Many times, due to a relaxation of the lattice mismatch between the substrate and the deposited film, a hybrid morphology where one or more layers (referred to as the wetting layer) will grow in the layer

by layer mode, followed by island growth. This hybrid mode is often referred to as the Stranski-Kratonov growth mode.

Typically the islands which grow in the Volmer-Weber or the Stranski-Kratonov growth mode resemble wedding cakes, as each ascending atomic layer of the island will occupy some fraction of the layer underneath it. This results in island shapes that resemble hills on the surface. However, for Pb islands, the grown islands display an unusual morphology. Each layer in the islands covers every layer underneath. These islands have very steep sides and flat tops. Also, these islands prefer certain heights over others, i.e. 5- 7- and 9- layer islands are far more common than 6- and 8-layer islands. This unusual growth morphology is believed to be caused by the quantum size effect.

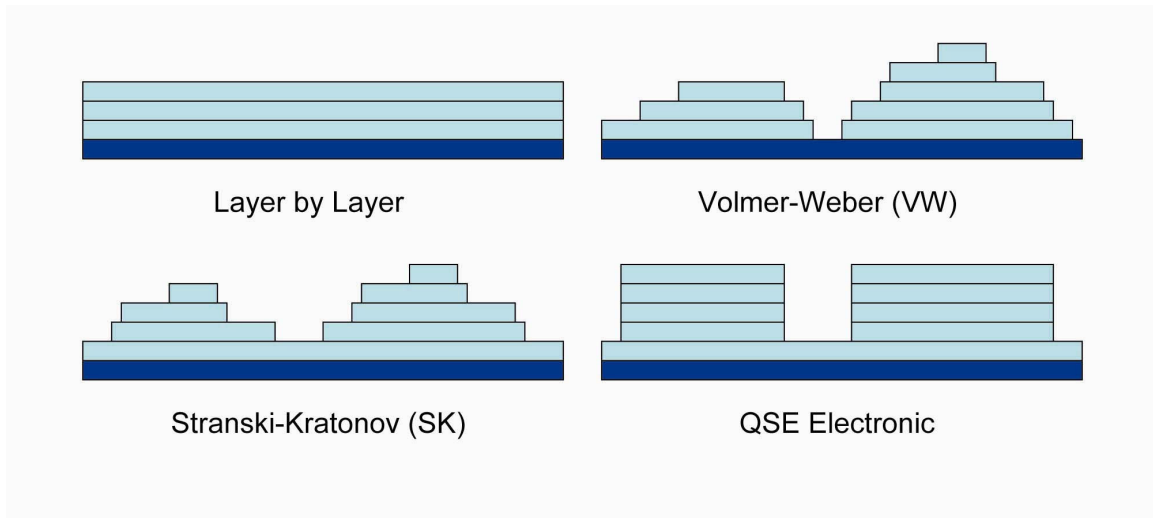


Figure 5: Typical growth morphologies in epitaxial growth. The new QSE-driven growth mode is similar to the Stranski-Kratonov growth mode, however, the grown islands have flat tops, steep sides and preferred heights.

As a metal film size is reduced to a few atomic layers, the film will begin to resemble a one-dimensional quantum well of width proportional to the thickness of the well. Free electrons within the metal will form standing waves based on the thickness of the well and the Fermi wavelength of electrons within the metal. This standing wave will give discrete

energy levels within the film. Depending on the relationship between these energy levels and the Fermi energy of the film the stability of these islands can change.

For Pb(111) the Fermi wavelength is nearly $4/3$ times the atomic level spacing of the islands. This means that the energy levels will oscillate such that the Fermi level will be alternating close to and far away from the electronic energy levels. This effect is illustrated in Figure 6. For the height H , the highest occupied electronic energy band HOB is far away from the Fermi energy, resulting in a stable energy configuration. When the island height is increased one level to $H1$, the highest occupied band moves closer to the Fermi wavelength, resulting in an unstable island configuration. With the addition of an additional layer ($H2$), the island highest occupied band is far away from the Fermi level again, resulting in another stable configuration. These roughly bilayer stability oscillations will continue as the thickness of the film increases. [18]

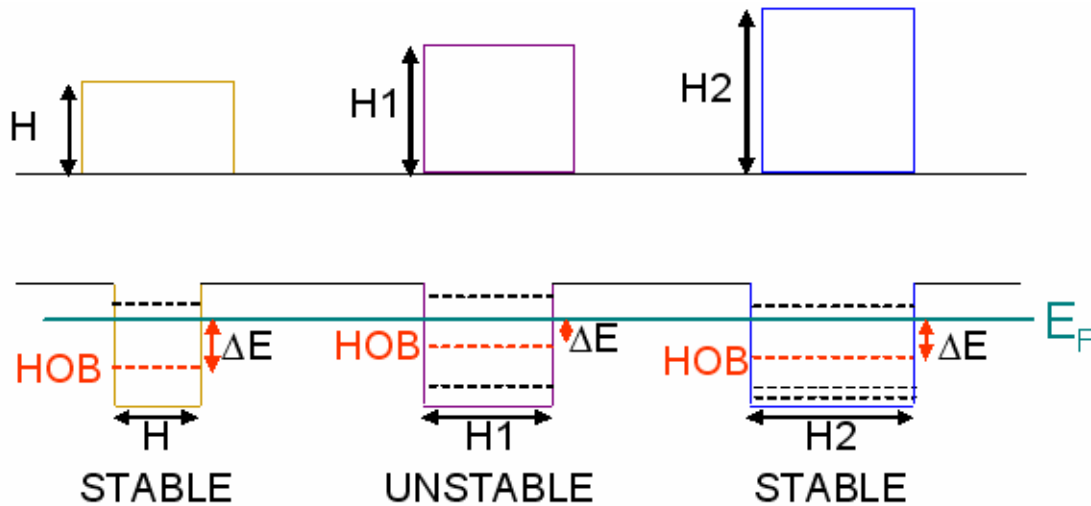


Figure 6: Illustration of the energetic cause of the preferred heights. Pb islands behave similarly to one-dimensional quantum wells with width proportional to the height of the islands. As the depth increases the difference between the highest occupied energy band in the well and the Fermi energy oscillates. When the difference is large the islands have increased energy dependence over islands where the difference is small.

In order to fully understand the QSE, it is important to understand all of the details of the island crystallography. An important feature of the islands which we can use to probe the

island crystallography is the corrugation of the island tops. The lattice constant of Pb(111) is 3.5 Å, while the lattice constant of Si(111) is 3.84 Å. This means that along the $[1\bar{1}0]$ direction 11 Pb atoms or 10 Si atoms fit within 38.5 Å. This creates a supercell where every 10th Si and 11th Pb atom line up at the same position. In two dimensions the lattice mismatch between the Pb overlayer and the Si substrate results in a 6-fold symmetric pattern called a Moiré pattern. This means along the $[1\bar{1}0]$ directions some Pb atoms will be located directly on top of an underlying Si atom, while others will settle into the spaces between the atoms. This results in a variation of atomic height along the island tops which is commonly referred to as the island corrugation. [19]

There are two types of corrugation patterns on the island surface. The first, often referred to as the Type I, pattern has bright spots on a dark background. The second, referred to as the Type II pattern has dark spots on a bright background. The two patterns arise from a combination of electronic and geometric effects. Pb(111) forms an fcc stacking sequence. There are two equivalent fcc stacking sequences, rotated by 180 degrees with respect to each other. Using other characteristics of the islands on the surface such as the shape of each type of island and the presence of lines of atoms known as decoration rows, we can identify which stacking sequence goes with which corrugation pattern. Once each stacking sequence is identified the number and area covered by each type of island in STM images is used to determine the population of each island type in STM. Surprisingly, for lower coverages the Type I stacking is preferred, while for higher coverages Type II stacking is preferred. This change in population must be caused by the Si(111) substrate, but it is still unclear what physics drives the transformation.

We can also look at how the Moiré pattern with the orientation of the islands with respect to the Si(111) substrate. A change in the orientation of Pb islands relative to the Si substrate with increasing coverage is observed for Pb islands grown on the Pb/Si(111) α -phase. The Pb lattice is also slightly compressed in the (111) plane with respect to the bulk value. For lower Pb coverage the $[1\bar{1}0]$ axis of the islands is most often aligned with the $[1\bar{1}0]$ axis of the substrate. At higher Pb coverage the islands coalesce and form a bilayer

with additional islands grown on top of the bilayer. At this coverage the islands prefer a rotation of 5.6° relative to the substrate.

Since the QSE has proven to be such a useful tool for controlling the vertical height of islands, an obvious question is to ask how we might be able to control the lateral size of islands as well. If even one lateral dimension could be controlled uniform “nanowires” might be created which might have very interesting physical properties. One technique to control the lateral size of islands in a system is to use a substrate which has anisotropic diffusion on the surface, i.e. atoms which are moving around on the surface prefer to move in one direction over the other.

The substrates that the Pb overlayers are grown on have a large effect on the island morphology, preferred heights, and stability temperatures. STM showed that islands grown on the anisotropic In(4x1) substrate form long wires with uniform heights and preferred width. Using SPA-LEED we verified the morphology of the islands and also observed an increase of the critical temperature to room temperature. As the sample is heated the wetting layer thickness changes from two layers thick to one layer thick, however the preferred height of the islands remains four layers high.

The Pb/Si(111) system has proven to be an excellent playground for studying different types of physics at the nanoscale. From the quasi 1-D DS to the quantum confinement of the islands we have seen a number of unusual properties which hopefully may be extended to new systems and theories.

References

- [1] <http://www.whitehouse.gov/stateoftheunion/2006/aci/>, Page viewed October 5, 2006.
- [2] M. Grundmann, *Physica E* **5**, 167 (2000)
- [3] P. Bhattacharya, S. Ghosh, A.D. Stiff-Roberts, *Annu. Rev. Mater. Res.* **34**, 1 (2004)
- [4] P.M. Petroff *et al.*, *Physics Today*, **54**, 5 46 (2001)
- [5] J.A. Venables, “Introduction to Surface and Thin Film Processes”, Cambridge University Press, 2000

- [6] G. Costantini, A. Rastelli, C. Manzano, R. Songmuang, O. G. Schmidt, K. Kern., *Appl. Phys. Lett.* **85**, 5673 (2004)
- [7] R. Notzel, *Semicond. Sci. Technol.* **11**, 1365 (1996)
- [8] O. G. Schmidt, S. Kiravittaya, Y. Nakamura, H. Heidemeyer, R. Songmuang, C. Müller, N. Y. Jin-Phillipp, K. Eberl, H. Wawra, S. Christiansen, H. Gabeldinger, H. Schweizer, *Surf. Sci.* **514**, 10 (2002)
- [9] K. Jacobi, *Prog. Surf. Sci.* **71**, 185 (2003)
- [10] A. Rastelli, S. Stufler, A. Schliwa, R. Songmuang, C. Manzano, G. Costantini, K. Kern, A. Zrenner, D. Bimberg, and O. G. Schmidt, *Phys. Rev. Lett.* **92**, 166104 (2004)
- [11] H. Heidenmeyer, C. Muller, O.G. Schmidt, *J. Cryst. Growth* **261**, 444 (2004)
- [12] V. Yeh, L. Berbil-Bautista, C. Z. Wang, K. M. Ho, and M. C. Tringides, *Phys. Rev. Lett.* **85**, 5158 (2000)
- [13] http://whome.phys.au.dk/~philip/q1_05/surflec/node23.html, page viewed October 19, 2006, figure adapted from Takayanagi et al., *J. Vac. Sci. Techn. A* **3**, 1502 (1985).
- [14] K. Oura, V.G. Lifshits, A.A. Saranin, A.V. Zotov, A. Katayama, “Surface Science: An Introduction” Springer-Verlag, 2003
- [15] U. Scheithauer, G. Meyer, M. Henzler, *Surf. Sci.* **178**, 441 (1986)
- [16] P. Bak and R. Bruinsma, *Phys. Rev. Lett.* **49**, 249 (1982)
- [17] M. Hupalo, J. Schmalian, and M. C. Tringides, *Phys. Rev. Lett.* **90**, 216106 (2003)
- [18] C. M. Wei and M. Y. Chou, *Phys. Rev. B* **66**, 233408 (2002)
- [19] M. Hupalo, V. Yeh, T. L. Chan, C. Z. Wang, K. M. Ho, and M. C. Tringides, *Phys. Rev. B* **71**, 193408 (2005)

CHAPTER 2: EXPERIMENTAL DETAILS

There are a number of tools needed to perform a surface science experiment in the laboratory. The primary tools in this thesis which are used measurement tools are Spot Profile Analysis – Low Energy Electron Diffraction (SPA-LEED) and Scanning Tunneling Microscopy (STM). In addition tools are also necessary to prepare the crystal surface and keep the surface unchanged throughout the course of an experiment. In this chapter the techniques used to prepare our samples for measurement will be discussed, as well as the instruments which we use to probe the crystal surface.[1,2]

In order to work on surfaces it is important that the conditions of the experiment do not change during the time of an experiment. In a normal atmosphere a typical silicon surface will be covered with a complete layer of particles from the atmosphere in around 10^{-9} second. So to keep the surface conditions the same throughout the experiment it is necessary to reduce the number of outside particles that come in contact with the sample by reducing the pressure at the sample surface. In Ultra High Vacuum (UHV) experiments it is necessary to reach a pressure of less than 10^{-9} torr (1 atm=760 torr). The base pressure for the experiments conducted in this thesis is on the order of 10^{-11} torr.

In the chamber where the SPA-LEED experiments are conducted, three vacuum pumps to achieve ultra high vacuum conditions. The first is a turbo molecular pump backed by a simple roughing pump. A turbo pump functions like a jet engine blowing out particles with a series of rotors. With only the turbo pump a pressure of 10^{-8} torr can be reached. To achieve lower pressures we use an ion pump and a titanium sublimator are used. In an ion pump a potential difference is created across two large metal plates. Gas atoms which fall between the plates become ionized and they accelerate toward the edges of the plates where they become trapped. The titanium sublimator sprays titanium atoms into the chamber. Many reactive particles in air such as hydrogen and oxygen will bind to the titanium atoms and be easily removed by the other vacuum pumps.

When a vacuum chamber is exposed to air it will accumulate a layer of air and water vapor on the inside of the chamber. In the vacuum this layer will slowly evaporate into the chamber raising the pressure inside the chamber. In order to remove this layer you can heat up the walls of the chamber to bake out this gas. To bake out the chamber heating coils are wrapped around the elements of the chambers. We then cover the heating tapes with foil to keep the heat in and to evenly heat the chamber. It is important to control the heat of the chamber because some of the instruments will become damaged with excessive heating. For example the SPA-LEED optics will become damaged if the temperature exceeds 200° C

Once UHV is obtained inside the chamber we need to prepare the crystal for the experiment. Even in UHV conditions a Si crystal will become covered with residual gas after being left overnight. To get the sample clean again we use a procedure we call “flashing”. First we heat the crystal to 1250° C (just below the Si melting temperature) in order to remove the excess gas from the sample. Then the sample temperature is reduced to 700° C slowly (2 minutes) which is the temperature through which the sample forms the 7x7 reconstruction and then quickly dropped to room temperature. Once the quality of the 7x7 reconstruction is verified with the SPA-LEED the sample is ready for experimentation. When a new crystal is placed in the chamber it is covered with an oxide film which is meant to keep the crystal clean during shipping. In order to remove this film from the crystal it is necessary to repeat the flashing procedure multiple times, with the pressure below 10⁻⁹ torr to prevent roughening of the crystal, however, once this film is removed the procedure will typically only need to be done once in order to produce a reproducible clean surface.

Once the sample is prepared then new layers can be deposited on the surface. This is done by a process known as molecular beam epitaxy (MBE). In the experiments in this thesis the molecular beams are controlled using a setup known as a Knudsen cell. In a Knudsen cell some amount of the material to be deposited is placed in a crucible with a small opening controlled by a shutter. The crystal is cooled with a water bath and other shielding to limit radiative heating of the surrounding chamber, which would lead to outgassing and rise of pressure inside the chamber. This setup is useful for materials with low melting

temperatures and high vapor pressures such as lead and indium. Since the vapor pressure is dependant on the source temperature, the deposition rate can be controlled with great precision simply by adjusting the temperature of the material since there is equilibrium between the gas and liquid phases. The deposition time is controlled by simply opening and closing the shutter.

In order to determine the total amount of material deposited on the surface, two methods are used. First we use two structures of known coverage, for example the $\sqrt{3}\times\sqrt{3}$ - β phase and the $\sqrt{7}\times\sqrt{3}$ phase of Pb. An ideal $\sqrt{3}\times\sqrt{3}$ - β phase is formed by annealing a sample of coverage slightly above the ideal coverage of the $\sqrt{3}\times\sqrt{3}$ - β phase until the diffraction peak intensity of the $\sqrt{3}\times\sqrt{3}$ - β phase spots has reached a maximum. From this ideal coverage Pb is added in small amounts and the intensity of the $\sqrt{7}\times\sqrt{3}$ phase spots which will begin to form when about 0.5 ML of Pb has been added is monitored. When the $\sqrt{7}\times\sqrt{3}$ phase peak intensity is maximized (or alternatively when the peak position begins to move indicating the formation of the devil's staircase) the surface coverage is determined to have reached the ideal $\sqrt{7}\times\sqrt{3}$ phase coverage of 1.2 ML. The flux rate is then calculated by determining the coverage difference and the coverage time.

After calibration, we can use a quartz crystal microbalance (QCM) to determine the amount of material deposited on the surface. A quartz crystal microbalance operates by placing a small quartz crystal in the path of the metal flux, but not directly between the source and the sample. The crystal will oscillate with a resonant frequency which is dependant on the crystal mass. As some of the deposited material accumulates on the crystal the resonant frequency of the crystal will change. By comparing this frequency change with the known amount of material deposited during the first calibration procedure, the deposited coverage can be expressed in terms of the change in crystal frequency. The sensitivity of the QCM is in the nanogram range giving submonolayer accuracy to the coverage measurements. The advantage of using a QCM to determine the amount of deposition is that the flux rate does not have to be recalibrated every time the heating current of the crucible is changed; the rate is monitored directly with the QCM.

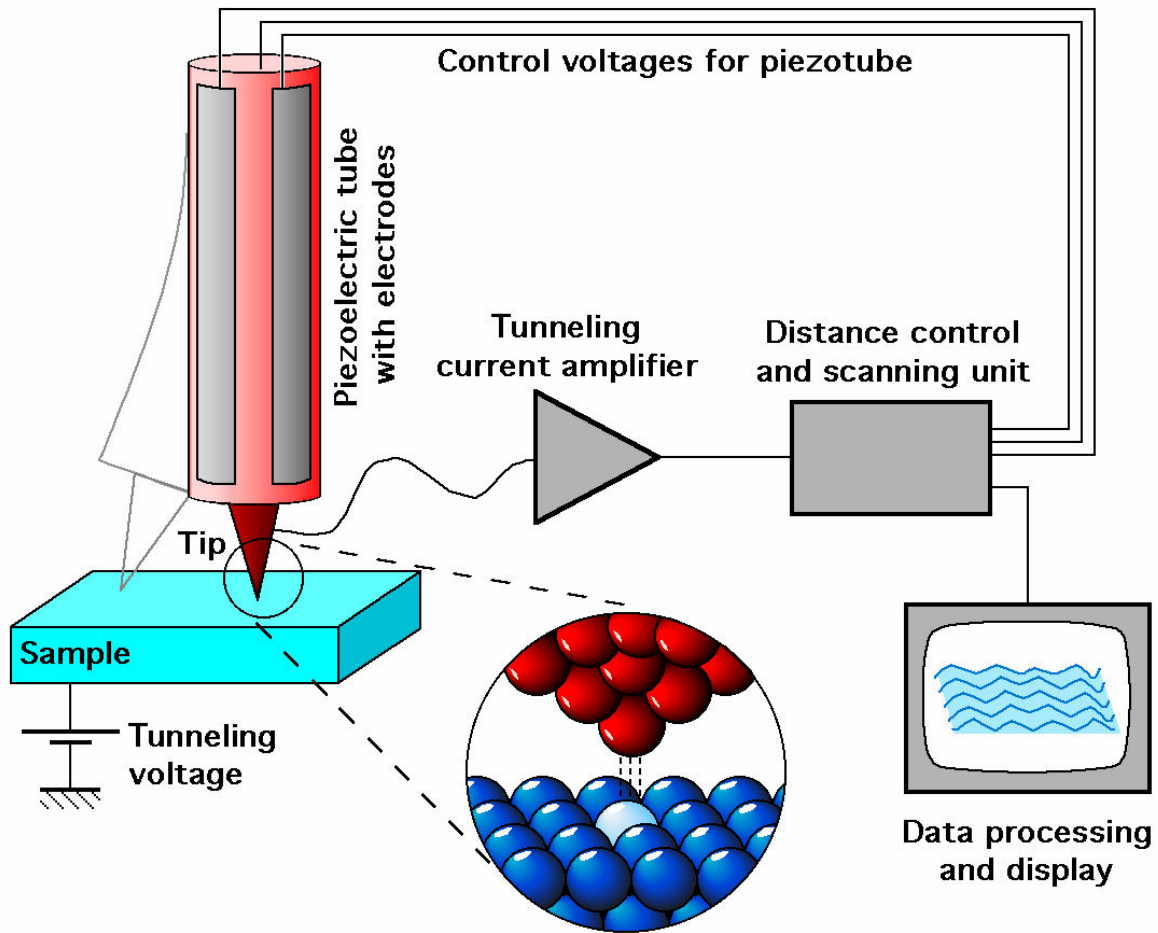


Figure 1: Schematic diagram of STM operation. Figure: Michael Schmid, TU Wien [3]

In our group we use two primary tools to determine the surface structure. Although the primary focus of this thesis has been in the use of SPA-LEED to characterize the surface, it has also been necessary to learn the basics of the STM experiment. The STM is one of the most powerful microscopes in the world, capable of real space images with resolution on the order of atomic distances. A diagram of a typical STM experimental setup is shown in figure 1. The STM works on the principle of quantum tunneling. The STM has an atomically sharp tip of a conductive material which is brought close to the surface of the sample. When a potential difference is induced between the tip and the sample an electron current will be created between the tip and the sample as electrons “tunnel” through the vacuum barrier to

reach the region of lower potential. The electron current is exponentially dependant on the distance between the tip and the sample.

In order to map out the real space structure the STM uses piezoelectric crystals to scan over the crystal surface. The limiting factors in the acquisition rate of the STM are related to the electronics which control the movement of the STM tip. The lateral resolution is limited by the sample temperatures on the surface. In addition to real space mapping of the surface, the potential difference between the tip and the sample can be varied in order to perform spectroscopy of the surface.

The second complementary technique we use to study the crystal surfaces is LEED. In an LEED experiment a beam low energy electrons (typically 10-200 eV) is directed toward the sample, since the wavelength of these electrons is on the order of the atomic separation of the crystal diffraction will be observed. In a conventional LEED system the diffracted electrons are scattered towards a screen, and the diffraction pattern can be recorded with a camera. Conventional LEED systems are often used in growth chamber as a rough guide to the quality of the grown crystal surface.

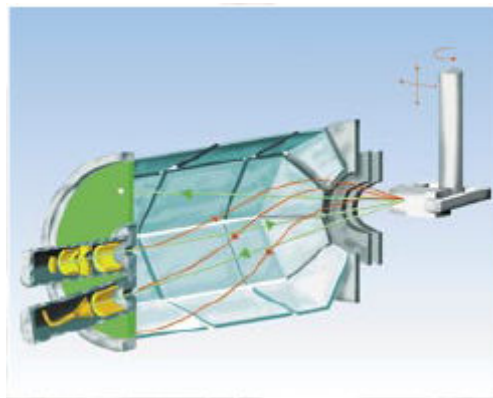


Figure 2: Octopole Electric field adjust the trajectory of the incoming and outgoing electrons so a single portion of reciprocal space is observed. From Omicron [4]

In order to do more quantitative analysis of a diffraction pattern in is important to increase the resolution in reciprocal space of a LEED system. One scheme used to increase the resolution is SPA-LEED. In a SPA-LEED system, the incoming and outgoing electron beams are passed through an octopole electric field. Figure 2 shows a schematic diagram of

the incoming and outgoing beams being deflected by the octopole. By choosing the appropriate field (usually done by computer) electrons which are diffracted to a specific portion of reciprocal space can be directed toward a high sensitivity electron detector. The sensitivity of the instrument in reciprocal space is determined by the transfer width of the incoming electron beam. For a conventional LEED system the transfer width is typically on the order of 100 Å, giving reciprocal space resolution of about 1-2% Si BZ. In the SPA-LEED the high sensitivity detector allows for a more sensitive beam and increases the transfer width to 2000 Å, allowing sensitivity of 0.5% BZ. The detector also provides quantitative intensity measurements which are much better than a conventional LEED system. The combined reciprocal space and spot intensity resolution is what allows the spot profile analysis which is the primary investigative tool of this thesis.

References:

- [1] K. Oura, V.G. Lifshits, A.A. Saranin, A.V. Zotov, A. Katayama, "Surface Science: An Introduction" Springer-Verlag, 2003
- [2] J.A. Venables, "Introduction to Surface and Thin Film Processes", Cambridge University Press, 2000
- [3] http://www.iap.tuwien.ac.at/www/surface/STM_Gallery/stm_schematic.html observed November 13, 2006
- [4] http://www.omicron.de/products/leed_instruments/spot_profile_analysis/spa_leed/media/spa_leed_1.pdf observed November 13, 2006.

PART I: DEVILS STAIRCASE OF LINEAR PHASES ON PB/SI(111)

CHAPTER 3: SELF-ORGANIZATION AT FINITE TEMPERATURES OF THE DEVIL'S STAIRCASE IN Pb/Si(111)

M. Yakes¹, V. Yeh², M. Hupalo³, and M. C. Tringides⁴

(A paper published in *Physical Review B* **69**, 224103 (2004))

Abstract

The “devil’s staircase” (DS) is one of the outstanding phase diagrams in physics because it shows a high degree of self-organization driven by a repulsive long-range adatom interaction. An infinite number of phases are predicted to exist which are built hierarchically with simple combinatorial rules. It was found with diffraction and scanning tunneling microscopy that a DS exists in Pb/Si(111) in the range $1.2 < \theta < 1.33$ monolayers, surprisingly at ~ 120 K, and with phases which extend spatially over macroscopic distances (~ 0.5 mm). The extraordinary amount of atom rearrangement necessary for these phases to form indicates an unexpected degree of self-organization at low temperatures.

DOI: 10.1103/PhysRevB.69.224103 PACS numbers: 61.14.Hg, 64.70.Rh, 68.35.Rh, 68.43.De

I. Introduction

Surface overlayers provide rich experimental realizations of statistical mechanical predictions related to phase transitions and ordering phenomena in two-dimensional models. [1-4] Temperature vs. coverage (T - θ) phase diagrams are normally constructed with the use of different experimental techniques (diffraction, scanning tunneling microscopy (STM), etc.) to map out regions where ordered phases of different symmetry form and to identify the nature of the transition lines separating these regions. A typical phase diagram consists of a finite number of distinct regions for each of the ordered phases present. Although these

¹ Graduate student, co-primary researcher on LEED experiments

² Graduate student, co-primary researcher on LEED experiments

³ Staff scientist, conducted STM experiments

⁴ Professor and author for correspondence

phases can be highly complex with complicated multicomponent order parameters, they are commonly accounted for in terms of a simple Hamiltonian which includes a set of short-range but possibly competing adatom interactions. The nature of the phase transitions is identified from the temperature or coverage dependence of the order parameter describing the extent of an ordered phase.

Contrary to these expectations based on short-range interactions, a highly unusual phase diagram has been predicted for a system with long range repulsive interactions even in one dimension (1D), i.e., the so called “devil’s staircase” (DS) phase diagram.[4-8] For example, adatoms on a 1D lattice with coverage θ and interacting with long range repulsion, at $T=0$ form an infinite number of commensurate phases.[9-11] The coverage of each of these phases is in one-to-one correspondence with the denumerable set of rational numbers $\theta=p/q$. The phase with coverage p/q has period q , with the p adatoms occupying sites in unique patterns dictated by the energy minimization of the system. The term “devil’s staircase” commonly refers to the θ vs. $\Delta\mu$ stability curve relating the coverage of a phase to its chemical potential. The stability interval $\Delta\mu$ depends only on the period of the phase q independent of the numerator p . Since rational numbers of arbitrary large denominator can be arbitrarily close to any θ and $\Delta\mu$ decreases with q , the “staircase” is built in a piecewise fashion from segments of variable length and has a fractal character well documented in the literature.[12] It has also been shown that an equivalent way to construct the hierarchical patterns of the DS phases is by combining recursively the unit cells of two generating phases of coverage θ_1, θ_2 (which define the coverage limits $\theta_1 < \theta < \theta_2$ for the DS). With increasing recursive stages, a larger number of unit cells of the generating phases is used to construct the phase of the higher stage, so its period increases and its stability $\Delta\mu$ decreases.

It has been an outstanding experimental challenge to discover in nature physical realizations of the DS, since physical phenomena are not expected to be described by fractal-like nondifferentiable functions.[13-17] To prove the presence of a DS in a physical system, it is required first to show that a large number of phases are present within a narrow $\Delta\theta$. Second, to show that these phases are generated in the hierarchical way by the same recursive

rules used to construct DS phases in the theoretical models.

This challenge is even more demanding when a statistical probe like diffraction (which probes macroscopic distances) is used. The identification of the specific phases from the expected ones based on DS phases is difficult because diffraction spots at new locations emerge as the coverage θ is changed even by minute amounts. For the numerous phases to be identified, it is necessary to prepare within the illuminated area [~ 0.5 mm for spot profile analysis (SPA) low-energy electron diffraction (LEED)] only one or two DS phases, so their characteristic wavevectors can be resolved. The indexing of the spots of even two coexisting phases close in coverage is nontrivial since some of their spots will be difficult to separate. A given DS phase can be conveniently described by the pair (n,m) of integers which denotes the number of unit cells of the generating phases. If the unit vectors of the two generating phases are b_1, b_2 times the substrate lattice constant, then the period of a (n,m) phase is $q=nb_1+mb_2$ and its diffraction spots at $(p/nb_1+mb_2)\%$ fraction of the Brillouin zone (BZ) while a phase with slightly higher coverage $(n-1, m)$ has spots at $(p'/(n-1)b_1+mb_2)\%$ BZ. Since p and p' are independent, some spots can be so close that higher resolving power is needed to discern them.

STM directly and unambiguously images the hierarchical DS phases constructed from the two generating phases, but it is more difficult to assess coverage uniformity over macroscopic distances ~ 0.5 mm. However, as demonstrated before,[18] a DS has been discovered in Pb/Si(111) with STM within the range $1.2 < \theta < 1.333$ monolayers (ML). 12 atomically resolved phases were identified according to the DS hierarchy. The two generating phases are the $\sqrt{7} \times \sqrt{3}$ ($\theta=1.2$ ML) and $\sqrt{3} \times \sqrt{3}$ ($\theta=1.33$ ML) phases.

However, since the DS phase diagram is strictly speaking valid only at $T=0$, an interesting question is what to expect at finite temperature.[19,20] Not only are the energy differences between the DS phases minute and for phases with larger q less than $k_B T$, but entropic effects should be taken into account to determine the dependence of the free energy of a phase on temperature. It is not clear how phases of larger q (and lower stability) transform after annealing to higher temperature. Or when the DS phases form after

deposition at constant temperature, does the number of the observed phases decrease if higher temperature is used? In either experiment finding out how DS phases transform to each other can be used to deduce their relative stability.

In addition to the question of energetic stability, the transition from one DS phase to another poses questions about the kinetics. High atom mobility is necessary for the surface to rearrange from the initial to the final DS pattern, but it is not clear what is the optimal kinetic pathway for the system to “discover” as many DS phases as possible? Intuitively, one expects faster diffusion at higher temperatures to promote the DS formation, since it is easier for the Pb atoms to move to locations dictated by the DS pattern. However, as shown below, quite unexpectedly a DS was discovered at low temperature (120 K) with a large number (~15) of macroscopically developed phases resolved. This indicates a still poorly understood nonthermal pathway to the highly complex self-organization required by DS. Since the DS phases are close in coverage, inhomogeneities (i.e., of the deposition rate or temperature or surface defects) can potentially limit the spatial extent of the phase. The use of diffraction with ~0.5 mm illuminated area offers the possibility of testing the spatial extent and coverage uniformity. If the coverage has large spatial fluctuations, different DS phases will nucleate and their diffraction patterns will be superimposed, so the spots will smear out. To address all these questions two complementary techniques, high-resolution electron diffraction (SPA LEED) and STM, are employed so the phase structure, kinetics, and spatial distribution can be examined from the atomic to the macroscopic scale.

II. Atom Arrangement In The DS Phases

A schematic model of the two generating phases, $\sqrt{3}\times\sqrt{3}$ and $\sqrt{7}\times\sqrt{3}$ is shown in Fig. 1. Smaller circles denote top layer Si atoms, and larger circles denote Pb atoms. The unit cell of the $\sqrt{3}\times\sqrt{3}$ phase has four Pb atoms, three of them are at off-centered $T1$ sites and one atom at the high-symmetry $H3$ site. The unit cell of the $\sqrt{7}\times\sqrt{3}$ phase has six atoms; five of them are at off-centered $T1$ sites and one at the high-symmetry $H3$ site. The coordinates of atoms are obtained from x-ray diffraction experiments [21] and were verified with first

principles calculations.[22] Although the long-range stress-driven interaction involves all the Pb atoms within the unit cell, it is a reasonable approximation to assume that an effective

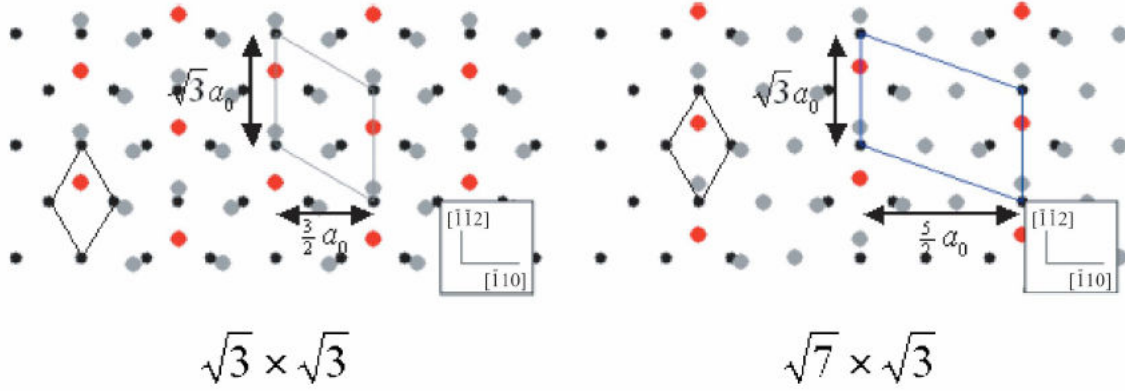


Figure 1: Schematic illustration of the $\sqrt{3} \times \sqrt{3}$ and $\sqrt{7} \times \sqrt{3}$ unit cell arrangements. Smaller circles denote Si and larger circles Pb atoms. The rows of the 1D structures are aligned along the $[\bar{1}\bar{1}2]$ direction and the DS ordering is along the $[\bar{1}10]$ direction.

interaction exists only between the high-symmetry atoms. The contribution of the Pb atoms at the off-symmetry sites simply renormalizes the strength of the interaction, but without changing its dependence on r , i.e., the separation between the two interacting atoms. Because of this reason in the kinematic calculations of the diffraction pattern discussed below, only the high-symmetry atoms are assumed in the unit cells.

The diffraction pattern expected for the ideal $\sqrt{3} \times \sqrt{3}$ has superstructure spots located at the $(1/3, 1/3)$ and $(2/3, 2/3)$ positions. The pattern of the $\sqrt{7} \times \sqrt{3}$ phase shown in Fig. 2 has two sets of six superstructure spots arranged on two equilateral triangles centered at the $(1/3, 1/3)$ and $(2/3, 2/3)$ positions. Three of the six spots are at the triangle corners and three are at the center of the opposite sides. The triangle height is $1/5$ the separation $4\pi/a_0$ of the (00) and (11) spots (with a_0 the Si lattice constant). The origin of the triangular spot arrangement is related to the threefold symmetry as shown schematically in Fig. 2 because $\sqrt{3} \times \sqrt{3}$ domains can grow in three equivalent directions. The center of the triangle is $(1/3, 1/3)$ the intersection of the three equivalent $[\bar{1}10]$ directions.

An (n,m) DS phase in Pb/Si(111) has unit cell vectors $b_2 = \sqrt{3}a_0\hat{y}$,

$b_1 = \sqrt{3}a_0/2\hat{y} + [(m+n)a_0/2]\hat{x}$ [if $m+n$ is odd] and $b_1 = [(m+n)a_0/2]\hat{x}$ [if $m+n$ is even] with period $q = 5n+3m$ in units of $a_0/2$. The diffraction pattern resulting from such a phase also has threefold symmetry. It can be expressed as the product of two terms, i.e., the

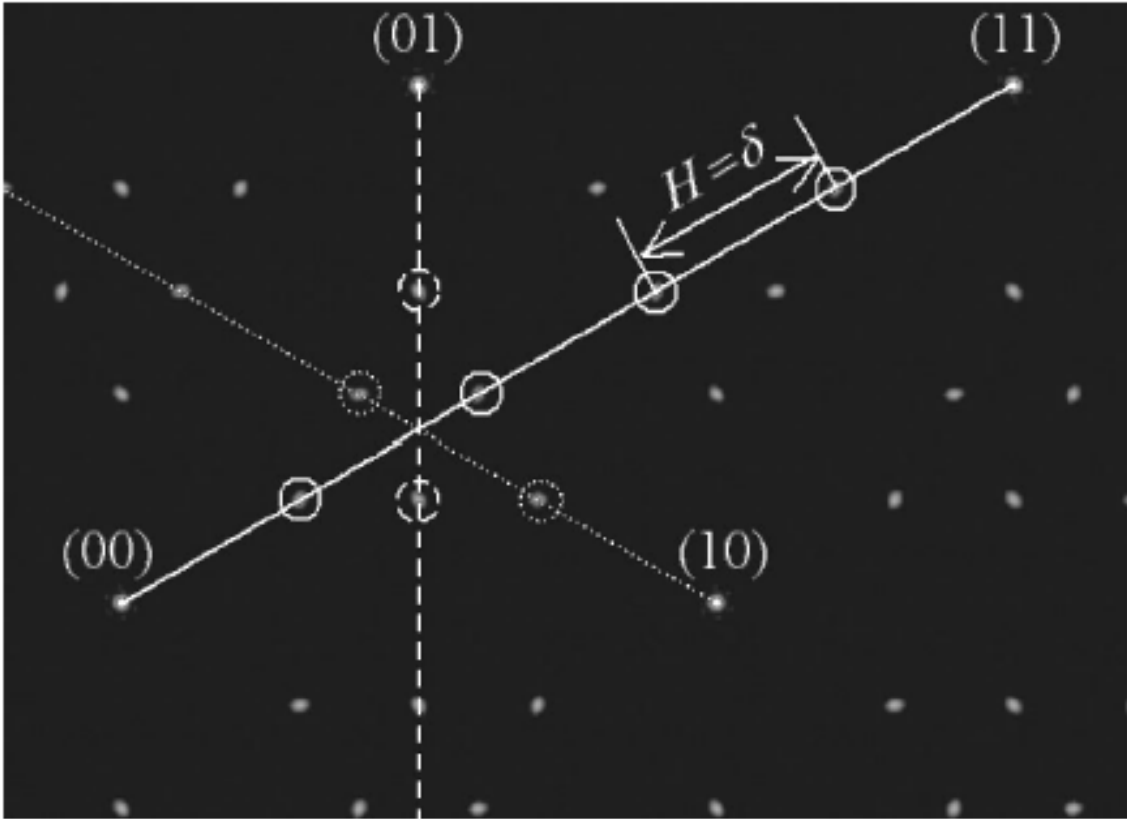


Figure 2: Schematic representation of the $\sqrt{7}\times\sqrt{3}$ diffraction pattern. Characteristic spots are observed at multiples of $1/5$ the diagonal connecting the (00) and (11) spots. Because of the three equivalent $[110]$ directions which intersect at the $(1/3, 1/3)$ position the six spots are arranged in triangular pattern. The triangle height H equals the δ -function separation for this phase.

scattering factor within a single (n,m) unit cell $F_{\text{unit cell}}$ times the reciprocal lattice of δ functions originating from long-range order

$$I_{\text{total}}(k_x, k_y) = \left| F_{\text{unit cell}} \sum_{l,s}^{s=n+m} \exp(ik_x \cdot lb_1 + k_y \cdot sb_2) \right|^2 .$$

The δ -functions are separated in the $[1\bar{1}0]$ direction by $\delta = 4\pi/a_0 / (5n+3m)$. To calculate F_{unit}

cell only the high-symmetry Pb atoms at positions rs are included

$$F_{\text{unitcell}} = \sum_{l,s}^{s=n+m} \exp(ik_x \cdot r_s).$$

The displacement vector between two neighboring high-symmetry atoms at $H3-H3$ sites is $\Delta_{s+1-s} = (3a_0/2, a_0/2)$ for neighboring $\sqrt{3} \times \sqrt{3}$ and $\Delta_{s+1-s} = (5a_0/2, \sqrt{3}a_0/2)$ for neighboring $\sqrt{7} \times \sqrt{3}$ unit cells. If there is a shift from an $H3$ to $T4$ position then the second component of Δ_{s+1-s} is $1/3$ of the previous shift $\sqrt{3}a_0/6$. Such a small shift can be detected from the ‘‘flipping’’ of the triangular pattern and it is related to the formation of other phases [‘‘HIC’’, ‘‘SIC’’] at higher temperatures not predicted for the DS model and will be discussed in a forthcoming publication.[23]

A typical kinematic calculation of the pattern is shown in Fig. 3 for the $(2,1)$ phase with only $H3-H3$ high-symmetry sites occupied. At the top the real space $(2,1)$ unit cell is shown schematically, i.e., two $\sqrt{7} \times \sqrt{3}$ rows separated by one $\sqrt{3} \times \sqrt{3}$ row. The calculated diffraction pattern is shown to the bottom left and the observed pattern to the bottom right. Spots are expected at $4\pi p/a_0(5n+3m) = p\delta$ with p an integer. However not all spots have the same intensity. The δ -function spots closer to the spot of the ideal $\sqrt{7} \times \sqrt{3}$ and the ideal $\sqrt{3} \times \sqrt{3}$ are expected to be the strongest. This suggests that the easiest way to identify an (n,m) phase is to use the triangle height H (i.e., the separation between the most intense spots along $[1\bar{1}0]$). More detailed identification of the phases present can be deduced from 1D scans by determining the integers p, n, m so all spots are matched to $4\pi p/a_0(5n+3m)$.

Next we show how H is related to the phase period for the $(n,1)$ and $(1,m)$ phases, which are the ones observed in the stepwise deposition experiments. For large n the strongest surviving δ -function spots (for the triangle centered at $(1/3, 1/3)$) are the ones closest to the superstructure spots which are at $1/5$ and $2/5$, of the diagonal (i.e., $4\pi/a_0 \cdot 173\%$ BZ where 100% corresponds to the BZ along the $[\bar{1}\bar{1}2]$ direction). This is because $F_{\text{unit cell}}$, which includes mostly $\sqrt{7} \times \sqrt{3}$ unit cells, has broadened superstructure spots at these positions. As θ increases and n decreases, the spacing between the δ -function spots $1/(5n+3)$ increases and they intercept the broadened superstructure spots due to $F_{\text{unit cell}}$ further away from the ideal

1/5 and 2/5 positions. These two intersections form the triangle vertex and the spot at the middle of the opposite side. Their separation is the triangle height H . Since these spots are separated by an integer multiple of the δ -function spacing and are the closest spots to the 1/5 and 2/5 locations of the 173% BZ diagonal, H is the largest possible integer multiple of the δ -

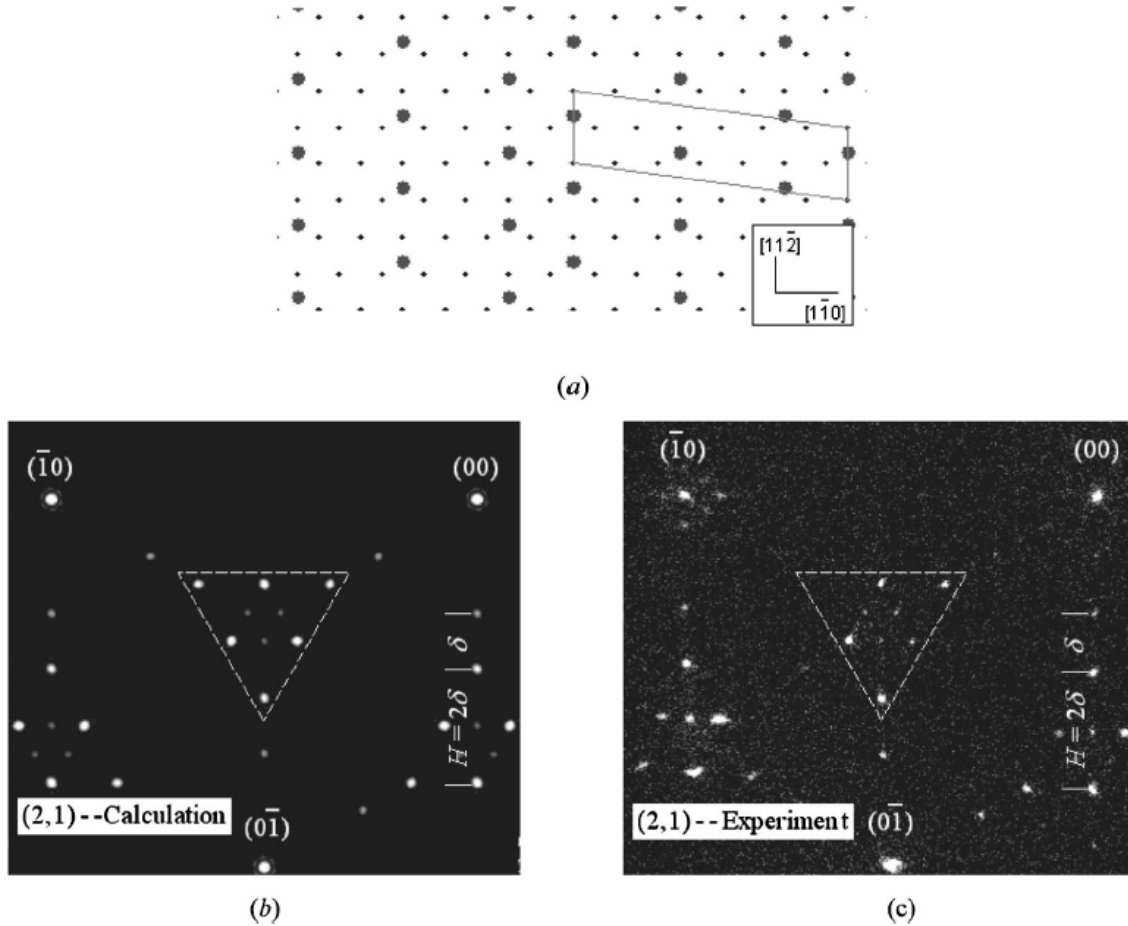


Figure 3: (a) Schematic representation of the (2,1) phase with the high-symmetry Pb atoms at H3-H3 positions. (b) Kinematically calculated diffraction pattern for the (2,1) phase with only the high-symmetry Pb atoms contributing. (c) Experimental pattern for the (2,1) phase showing agreement with the calculated one (except for the missing spot at the top vertex of the triangle).

function separation which is less than 1/5. This multiple is just n since

$$H/[1/(5n+3)] = \text{int} \left\{ \frac{1/5}{1/(5n+3)} \right\} = \text{int} \{n + 3/5\} = n$$

where $\text{int}\{\}$ denotes the integer part of a number.

For the $(1,m)$ phases intense superstructure spots due to $F_{\text{unit cell}}$ are expected closer to the $1/3, 2/3$ (in units of the diagonal $4\pi/a_0$ since the $(1,m)$ unit cell has a majority of $\sqrt{3}\times\sqrt{3}$ than $\sqrt{7}\times\sqrt{3}$ unit cells) and should become sharper as m increases. As m decreases the δ -function separation $1/(3m+5)$ is less than $1/3$ the separation of the superstructure spots, so the most intense spots closest to the $1/3$ spot are simply separated by $1/(3m+5)$ in % BZ which can be used to determine the value of m and identify unambiguously the phase present.

III. Formation of The DS At Low Temperatures

The diffraction experiments were carried out in an UHV system equipped with a SPA LEED diffractometer, an Auger spectrometer, and a mass spectrometer. As described elsewhere, flux calibration was deduced from the Auger breaks at room temperature and low temperatures ~ 120 K after monolayer completion.[24] In addition, the DS itself provides a fine flux calibration from the relation between the period q of a phase and its coverage $\Delta(q)$. The STM experiments were carried in a different UHV system, but under similar preparation conditions (of θ and T).

Different kinetic pathways to prepare the ideal DS were explored. The starting point was a perfect $\sqrt{7}\times\sqrt{3}$ at $T < 120$ K. A Pb amount $\Delta\theta < 0.1$ ML was added on the $\sqrt{7}\times\sqrt{3}$ followed by thermal annealing; or a larger Pb amount was deposited $\Delta\theta = 0.2$ ML and desorbed by heating progressively to higher temperature > 500 K; or the deposition was on a hot surface $T = 500$ K and at a higher flux rate, so finer coverage control can be obtained when dynamic equilibrium is established between the incident and desorbing atoms. All these recipes rely on the thermal energy of the atoms to generate via diffusion the different (n,m) phases. Although new phases were produced in such thermal preparations with new diffraction spots observed, these were in practically all cases spots corresponding to the most stable DS phases (i.e., the ones with the smaller period $\sqrt{7}\times\sqrt{3}$, $(2,1), (1,2)$ etc.).

It was surprising that a DS, shown in Fig. 4, with distinct phases clearly identified from their 1D profiles along the $[1\bar{1}0]$ direction, was prepared at low temperature < 120 K

without thermal annealing. The $[1\bar{1}0]$ direction contains the information about DS phases because it corresponds to the direction of ordering of the unit cells $\sqrt{7}\times\sqrt{3}$ and $\sqrt{3}\times\sqrt{3}$ of the generating phases. Each DS phase is prepared after stepwise deposition of only $\Delta\theta < 0.006$ ML starting initially with the $\sqrt{7}\times\sqrt{3}$ phase on the surface. All 15 phases were observed within < 0.1 ML additional coverage.

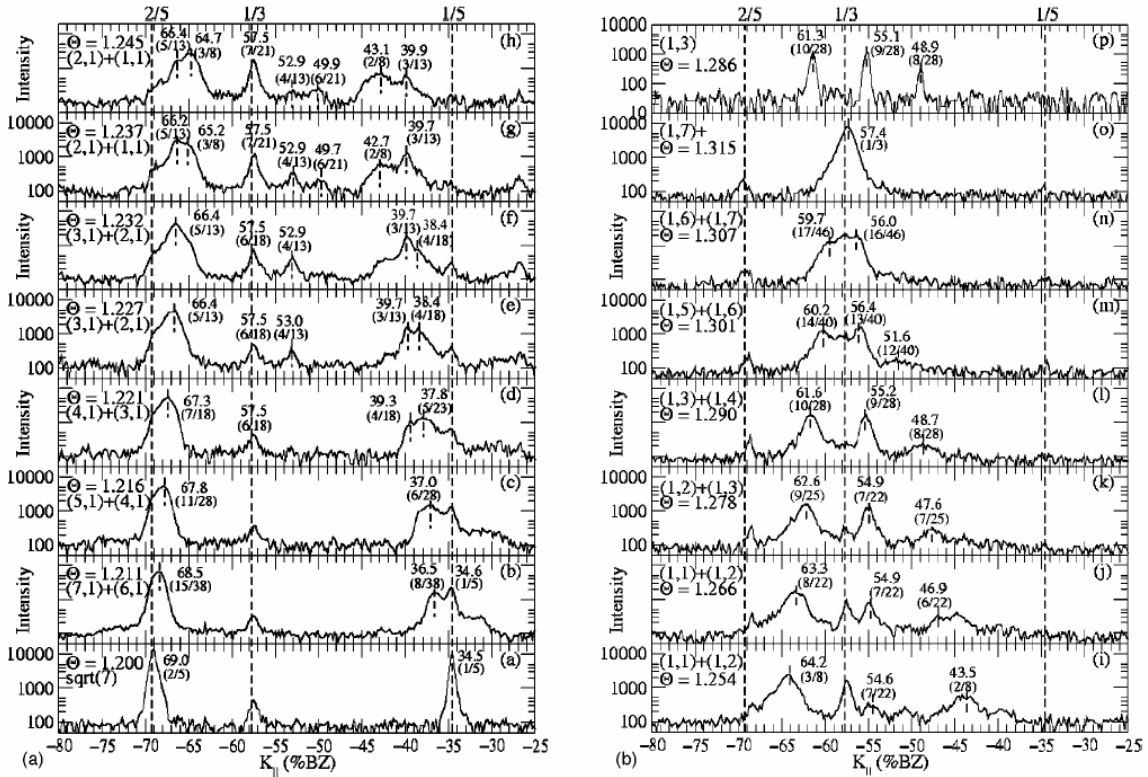


Figure 4: 1D scans of the low temperature DS phases formed after stepwise deposition on top of the $\sqrt{7}\times\sqrt{3}$ at 120 K approximately an amount $\Delta\theta \sim 0.006$ ML after each deposition. The phase identified and the average coverage are shown to the top left corner. The dotted lines are at spot positions expected for the ideal $\sqrt{7}\times\sqrt{3}$ [multiples of $1/5$ the length of the diagonal (00) and (11)] and the ideal $\sqrt{7}\times\sqrt{3}$ phase (at multiples of $1/3$ the diagonal length). The spot position is converted into a fractional ratio which is used to identify the DS phases. For example, $15/38$ indicates the presence of the (7,1) phase, $11/28$ indicates the presence of the (5,1) phase, etc. Phases with $\theta > 1.25$ have $1/2$ the expected triangle height H which indicates that H3 and T4 sites are occupied. The profile (p) is obtained after overnight annealing of the (1,7) phase $\theta = 1.315$ ML, indicating that a single (1,3) phase $\theta = 1.286$ ML occupies the area ~ 0.5 mm illuminated by the electron beam.

A typical 2D pattern is shown in Fig. 3 (bottom right) for the (2,1) phase to be

compared to the calculated one (bottom left). The spots are arranged in triangular pattern around the $(1/3, 1/3)$ and the equivalent $(2/3, 2/3)$ positions as expected from the kinematic calculation described in Sec. II. We mostly discuss the triangle around the $(1/3, 1/3)$ spot because of better linearity in the SPA LEED optics. The outlined white triangle highlights the triangular pattern of the ideal $\sqrt{7} \times \sqrt{3}$ phase and is used to focus on new spot positions as new DS phases form. One of the six spots in the triangle is missing at the particular energy 80 eV. It is not clear why the spot is absent; possibly it can be due to the dependence of the scattering factor on incident energy or more complex dynamic effects but since it does not affect the identification of the DS phases, this question has not been investigated further.

The 2D patterns for the other DS phases were omitted because of space limitations and because the exact spot positions and wave vector shifts can be measured with better accuracy from the 1D scans along the $[1\bar{1}0]$ direction shown in Fig. 4. Before discussing how the spots were indexed and the DS phases identified, it is easily seen that changes in the pattern occur and new spots at different wave vectors emerge after each 0.006 ML (except the last profile which results after overnight annealing experiment to be discussed below). Numerous phases within narrow $\Delta\theta$ is one of the necessary conditions to realize experimentally a DS. The dotted lines show the wave vectors where the spots of the generating phases are expected as fractions of the diagonal, i.e., its length is 173% $BZ=4\pi/a_0$) at $1/5$ (34.6%), $2/5$ (69.3%) for the $\sqrt{7} \times \sqrt{3}$, and at $1/3$ (57.3%) for the $\sqrt{5} \times \sqrt{3}$ phase. The shown range in reciprocal space is limited from 25% to 80% of the BZ.

To identify the DS phases we first use the height of the triangle H (i.e., the separation between the most intense spots in the 1D scan). In addition we index all the spots which have intensity above twice the background. Some spots overlap either because two majority phases adjacent in coverage cover the illuminated area or because adjacent δ functions of a single phase are within the diffuse spots generated by $F_{\text{unit cell}}$. Both effects result in broader, ‘‘streakier spots’’ but clearly the maxima due to the separate components can be resolved and unique wave vectors can be assigned to them. Above a major spot we denote its position as a fraction of the $[11\bar{0}]$ BZ. For example profile f in Fig. 4(a) has wave vectors at 66.4%, 57.5%, 52.9%, 39.7%, and 38.4%. We search for the fraction closer to the ratio of these

wavevectors to the width of the BZ (173%) to assign 5/13, 6/18, 4/13, 3/13, 4/18 to the above wave vectors. This corresponds respectively to the (2,1), (3,1), (2,1), (2,1), and (3,1), phases with (2,1) and (3,1) the main ones. The coverage of an (n,m) phase is $\theta=1+(m+n)/(5n+3m)$. We estimate the coverage on the surface for profile f $\theta=1.232$ ML from the fractional occupation of the two phases (deduced from their peak intensity) and the additional deposited amount $\Delta\theta<0.006$ ML. The profile g in Fig. 4(a) obtained after the next deposition has spots at 66.2%, 65.2%, 57.5%, 52.9%, 49.7%, 42.7%, 39.7% which are identified as 5/13, 3/8, 7/21, 4/13, 6/21, 2/8, 3/13, respectively. The two phases corresponding to the main spots are the (2,1) and (1,1) with average coverage 1.237 ML. In a similar way all the major DS phases and the average coverage have been identified for all 16 profiles of Fig. 4 and are shown to the left corner of each profile.

It is remarkable that in practically all cases only two phases are sufficient to cover more than 95% of the illuminated area of ~ 0.5 mm. However in a few cases, some spots which correspond to other phases besides the two major ones are present like spots 57.5% and 49.7% at profile h in Fig. 4(a). These spots are accounted for by a second generation phase (3,2) with period 21 (3,2) should be written more accurately as (1,1,2,1), i.e., one $\sqrt{7}\times\sqrt{3}$, one $\sqrt{3}\times\sqrt{3}$, two $\sqrt{7}\times\sqrt{3}$, one $\sqrt{3}\times\sqrt{3}$ with $\theta=26/21$ slightly less than $\theta=10/8$, the coverage of the (1,1) phase.

For phases with coverage $\theta>1.25$, the observed spots are indexed with height, half the one expected for an (n,m) phase, and the triangularly arranged spots “flip.” This indicates that the binding site in the unit cells of the generating phases can be either $H3$ or $T4$ sites, which causes a doubling of the period of an (n,m) phase to $2(5n+3m)$. This in turn implies that the spacing of the δ -functions in the $[1\bar{1}0]$ direction is half the spacing for the same (n,m) phase with only $H3$ - $H3$ sites occupied. In addition, as mentioned before the shift $a_0/6$ between $H3$ and $T4$ sites in the $[\bar{1}\bar{1}2]$ direction is $1/3$ the shift between the $H3$ and $H3$ sites. This additional symmetry breaking implies that even fundamental spots (kl) will show satellite spots whenever $\text{mod}_3(k-l)\neq 0$. For example, the (00) and (11) spots do not show satellite spots while the (01) and (10) do. These observations, to be discussed in more detail in the future,[23] suggest that the onset of the $H3$ - $T4$ occupation is the (1,1) phase.

Phases with higher period q and lower stability, which are not easily observed after thermal annealing, are observed after low-temperature deposition. It is not yet clear why thermal annealing does not lead to these less probable phases, since atom diffusion is faster at higher temperature. However, since the changes of the patterns shown in Fig. 4 are observed immediately after the deposition of $\Delta\theta$, some type of mass transport must be operating very efficiently even at low temperatures, leading to this unusual self-organization. It is intriguing that the readjustment to the next DS phase after $\Delta\theta$ deposition is very fast (\sim few seconds) over the whole macroscopic surface. This is evident from the continuous decrease of the triangle height H with θ seen in the 2D patterns with naked eye and correspondingly in the 1D scans of Fig. 4. The degree of self-organization and highly correlated atom movement which is needed to change at 120 K an initial $(n-1,1)$ to a final $(n,1)$ phase is extensive [since after depositing $\Delta\theta \sim 0.006$ ML the average distance between the arriving atoms is $(\Delta\theta)^{1/2} \sim 26a_0$ so atoms need to diffuse at least over this distance to reach their final well-defined positions within the $(n,1)$ unit cell]. The long-range strain interaction between the Pb atoms, which is induced by the underlying substrate, provides the necessary energy for the mass transport over large distances.

The phase obtained after overnight slow annealing to room temperature phase (o) in Fig. 4(b) prepared at 120 K with $\theta < 1.315$ ML is $(1,3)$ of lower coverage ($\theta = 1.286$ ML) as shown in profile p of Fig. 4(b). The pattern is extremely sharp with the observed spots accounted for exclusively from the $(1,3)$ phase and with instrumentally limited full widths at half maximum. Some Pb must have been removed from the system (most likely to steps or to form very few two-layer Pb(111) islands)[24] since the coverage of the $(1,3)$ phase is lower and the triangle height H is 7% which is larger than the height of phase o . It is extraordinary that a single $(1,3)$ phase covers the surface over macroscopic distances which requires even higher coverage uniformity than when two DS phases are present. The low-temperature transformation from a lower- to a higher-coverage phase according to the DS phase diagram is also seen with STM. Figure 5(a) shows a $13.5 \times 18.5 \text{ nm}^2$ image with the surface prepared in the $\sqrt{7} \times \sqrt{3}$ phase. After depositing an amount of $\theta = 0.07$ ML Fig. 5(b) shows a dramatic change of the surface morphology with the $(2,5)$, i.e., $(1,2,1,3)$, similar to the ones shown in

profile k in Fig. 4(b), thus confirming the diffraction results that a high-quality DS can be prepared at low temperature.

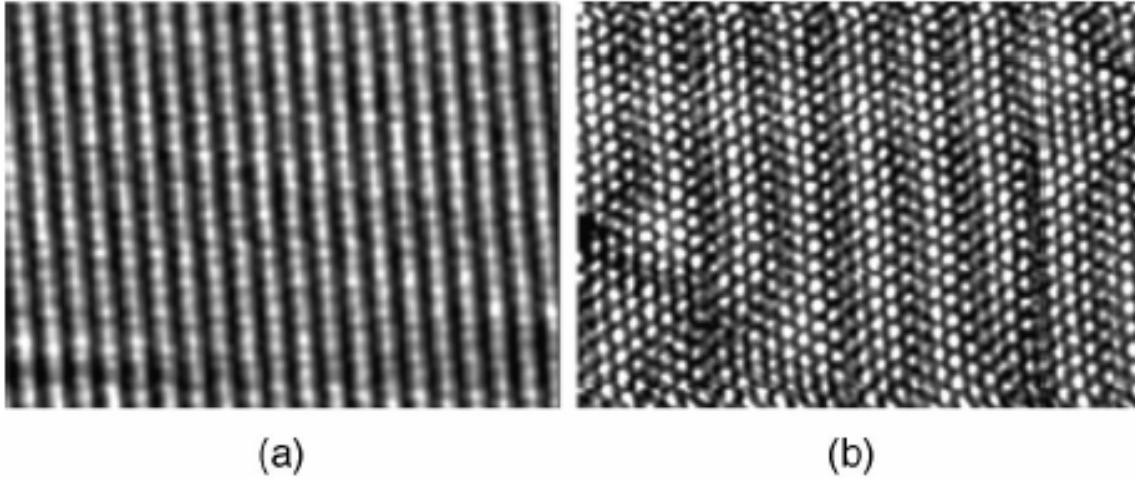


Figure 5: STM image $18.5 \times 13.5 \text{ nm}^2$ indicating the formation of a 1-D phase $(1,2,1,3)$ $q\text{-}32/25$ ML after deposition of 0.07 ML on top of the $\sqrt{7} \times \sqrt{3}$ at low temperature $T = 40$ K.

IV. Finite Temperature Effects in the DS

We would like to address briefly the second question raised in the introduction, i.e., what is the role of the finite temperature in the formation of the DS phases since strictly speaking a DS is possible only at $T=0$? To answer the question we performed two types of experiments, first to deposit in a stepwise fashion (as in the experiment of Fig. 4) but at higher constant temperature $T > 120$ K and second, to anneal at constant θ to higher temperatures an initial DS phase formed at low temperature.

Figure 6 shows the results of the first type of experiment with Pb deposited at $T=169$ K and with larger coverage increments $\Delta\theta \sim 0.01$ ML (than in the 120 K experiment). We observe again the same progression to $(n,1)$ phases with increasingly smaller n and higher coverage [the first stable phases resolved are $(6,1)$ and $(5,1)$ with $\theta=1.21$ ML]. However, within the range $1.23 < \theta < 1.27$ ML instead of observing only 1D DS phases, a new phase of hexagonal symmetry, the ‘‘HICA’’ phase, is found to coexist with the $(2,1)$ phase. A model of the ‘‘HICA’’ phase has been proposed in Ref. 25. It was identified as a commensurate phase of hexagonally arranged $\sqrt{3} \times \sqrt{3}$ triangular domains phase separated by light ‘‘almost

$\sqrt{7}\times\sqrt{3}$ domain walls (this phase is slightly different from the ideal $\sqrt{7}\times\sqrt{3}$ phase because adjacent $[1\ \bar{1}2]$ rows have Pb atoms on $H3$ and $T4$ sites occupied instead of only $H3$ sites).

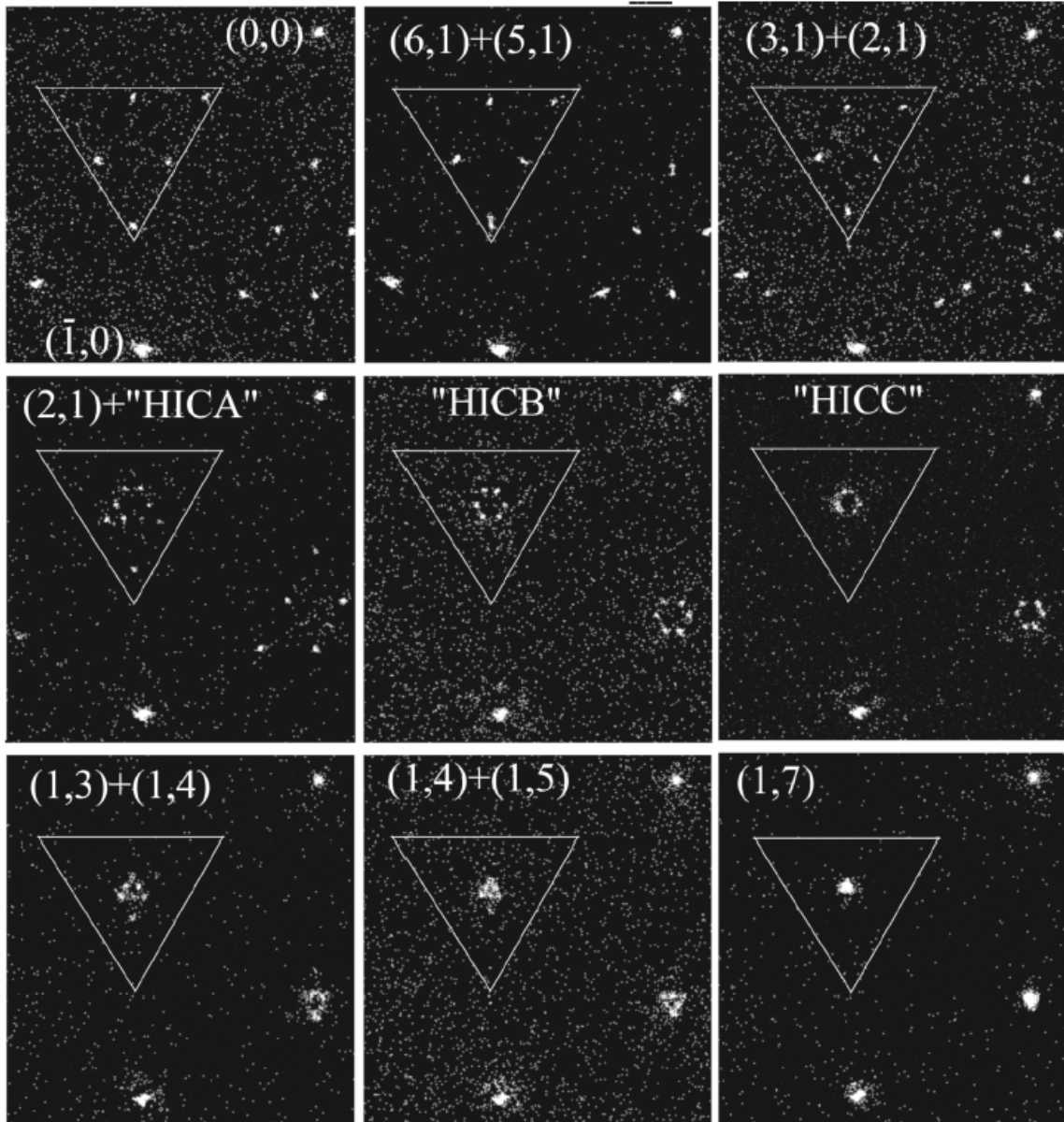


Figure 6: Stepwise deposition experiments at constant temperature $T=169$ K with $\Delta\theta\sim 0.01$ ML showing the formation of 1D phases as expected from the DS hierarchy. In the coverage range $1.23 < q < 1.27$ ML phases of hexagonal symmetry “HIC” form.

Such “HICA” phase is easily distinguished with diffraction, because it gives rise to hexagonally arranged spots around $(\frac{1}{3}, \frac{1}{3})$ rather than the triangular patterns of Fig. 3. A

pair of spots is aligned along the $[\bar{1}\bar{1}2]$ direction resulting in the characteristic “horizontal splitting” described in earlier reflection high-energy electron diffraction and LEED studies.[26-28] The separation of the spot from the $(\bar{1}/3, \bar{1}/3)$ position can be used to deduce the domain size 4.7 nm for the HICA phase, consistent with the model proposed in Ref. 25 with STM. With further deposition of $\theta=0.01$ ML new types of “HICA” phases form (denoted as “HICB” and “HICC”) with slightly higher coverage, i.e., larger $\sqrt{3}\times\sqrt{3}$ triangular domains, since the size of the observed hexagon decreases with increasing coverage. Details about the structure of these new “HIC” phases will be described in a future publication. For higher coverage $\theta=1.27$ ML 1D phases $(1,m)$ form, similar to the low-temperature $T=120$ K deposition experiments.

The “HIC” phases also form after heating to higher temperature a surface which is initially covered with 1D phase. The transition temperature T_c from a 1D to the “HIC” phase depends on the coverage of the 1D phase [T_c for the $(1,1)$ phase with $\theta=1.25$ ML has the lowest $T_c = 130$ K with all the other 1D phases undergoing the transition at higher T_c]. Typical results are shown in Fig. 7 with the $(2,1)$ phase prepared initially on the surface at 136 K as evident from the size of the triangle height $H=26.6\%$ BZ. At 202 K the $(2,1)$ coexists with the “HICA” phase. With annealing the pattern of the “HICA” phase reaches maximum intensity at 216 K but with further heating this phase gradually disorders, as seen from the lower intensity, until at 362 K only a (1×1) pattern is present. Cooling the surface back to 136 K restores the $(2,1)$ but at slightly reduced intensity, indicating that possibly some Pb has diffused irreversibly to the steps. These thermally or coverage induced transformations of the (n,m) phases to the “HIC” phase and to what extent they are reversible or not, will be discussed in the future.

With coverage θ approaching $4/3$ ML the thermally annealed phases give rise to the “SIC” phase, a phase consisting of $\sqrt{3}\times\sqrt{3}$ domains separated by meandering “almost $\sqrt{7}\times\sqrt{3}$ ” domain walls. The walls do not have the regular hexagonal arrangement as in the “HIC” phase (Fig. 8). They have shorter length per unit area than the hexagonally arranged

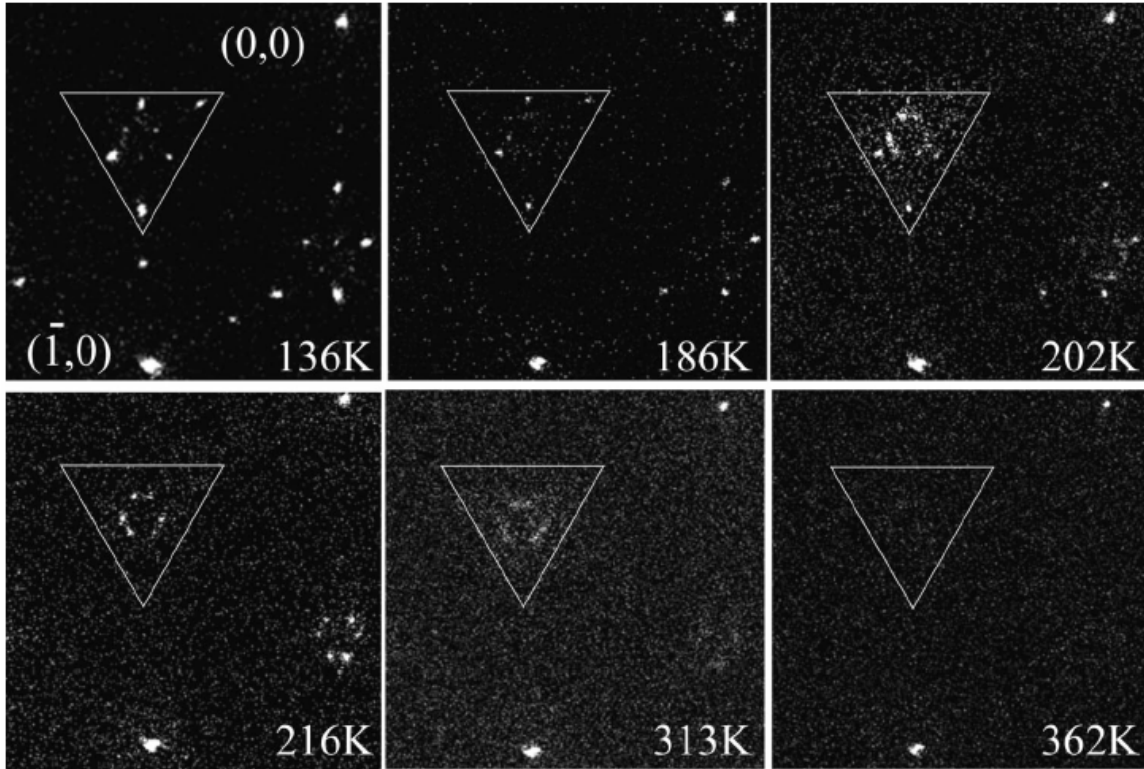


Figure 7: Thermal annealing of a surface prepared initially in the (2,1) phase $\theta=1.231$ ML at 136 K showing the progressive evolution to the “HICA” phase (186 K), to the disordered “liquidlike” phase and finally to the (1x1) disordered phase. Cooling the surface back to 136 K recovers the (2,1) phase.

domain walls, so higher coverage can be accommodated. No evidence for this “SIC” phase is found after deposition at low temperatures. The corresponding 1D scans for Fig. 4(b) show that the characteristic triangle height H continuously decreases and falls below the instrumental resolution which indicates the formation of large $\sqrt{3}\times\sqrt{3}$ domains with possibly extremely low $\sqrt{7}\times\sqrt{3}$ domain wall density which cannot be resolved in the diffraction patterns.

A different issue is related to the type of binding site the high-symmetry Pb atoms occupy in the unit cells of the generating phases. It has been observed in STM images and supported with first-principles calculations that the triangular domains of the HIC alternate between the Pb atoms occupying $H3$ vs $T4$ because these sites have approximately the same energy.[22] On the other hand, the structure of the ideal $\sqrt{7}\times\sqrt{3}$ phase ($\theta=6/5$ ML) has the high-symmetry Pb atoms only on $H3$ sites. It is interesting to ask whether the 1D (n,m)

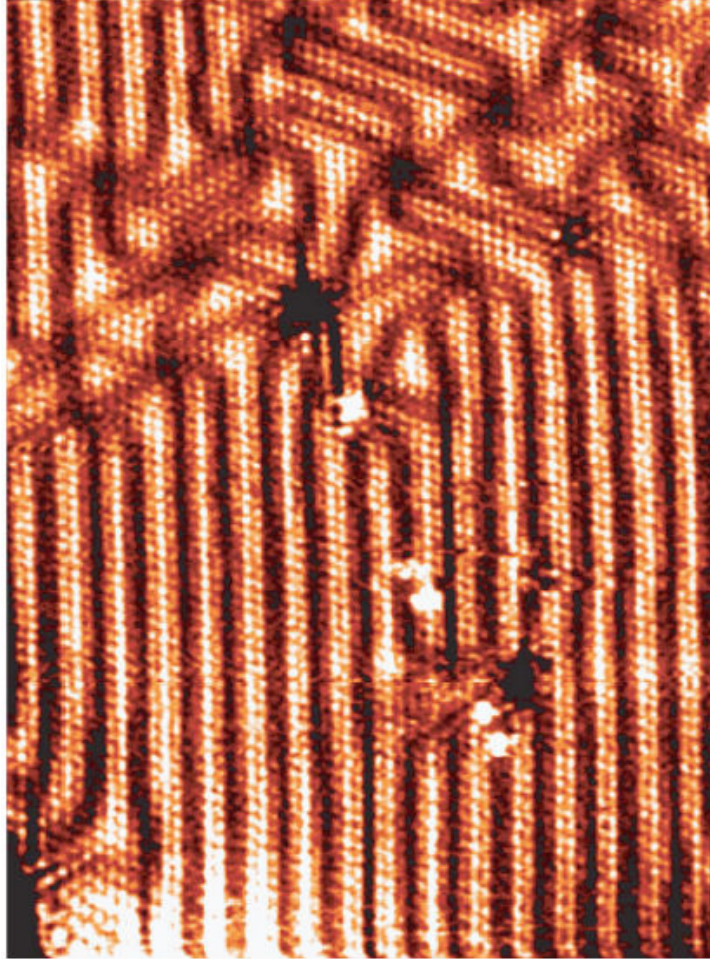


Figure 8: STM image over a scale $38 \times 50 \text{ nm}^2$ showing the coexistence of a 1D (1,2) phase with “HICC” phase as shown in the diffraction patterns of Figure 6.

phases have only $H3$ sites occupied or at some coverage there is a transition with either $H3$ or $T4$ sites occupied. As mentioned before, we observe such a transition close to $\theta=1.25 \text{ ML}$ the coverage of the (1,1) phase (the coverage of the “HICA” phase although such a phase did not form at the low temperature deposition $T=120 \text{ K}$ of Fig. 4).

V. Summary

In summary we have shown that DS phases in Pb/Si(111) in the range $6/5 < \theta < 4/3 \text{ ML}$ can be prepared after growth at low temperature without the need of thermal annealing. Only 1D phases are observed after stepwise deposition of small coverage amounts $\Delta\theta < 0.006 \text{ ML}$ at 120 K and without the “HIC” phase which appears after thermal annealing or during

deposition at higher temperature. Phases of larger periods (and smaller stability range) can be prepared at low temperatures rather than after thermal annealing. It is possible to cover macroscopic distances (0.5 mm the size of the incident electron beam) with predominantly two or even a single 1D phase by stepwise deposition of $\Delta\theta$. This unexpected formation of the DS at low temperature demonstrates that self-organization is possible, due to still unclear but very effective kinetic mechanisms.

Acknowledgements

Ames Laboratory is operated by the U.S. Department of Energy by Iowa State University under Contract No. W-7405-Eng-82. This work was supported by the Director for Energy Research Office of Basic Energy Sciences.

References

- [1] L.D. Roelofs, in *Handbook of Surface Structure*, edited by W. Unertl (Elsevier, Amsterdam, 1997), Chap. 13.
- [2] E. Bauer, in *Topics in Current Physics*, edited by W. Schommen and P. von Blanckenhagen (Springer-Verlag, Berlin, 1987).
- [3] *Ordering in Two Dimensions*, edited by S.K. Sinha (North-Holland, New York, 1980).
- [4] H. Taub, G. Torzo, H.J. Lauter, and S. Fain, *Phase Transitions in Surface Films 2* (Plenum, New York 1991).
- [5] P. Bak, Rep. Prog. Phys. **45**, 587 (1982).
- [6] V.L. Pokrovsky, A.L. Talapov, and P. Bak, in *Solitons*, edited by S.E. Trullinger, V.E. Zakharov, and V.L. Pokrovsky (North-Holland, Amsterdam, 1986), pp. 71–128.
- [7] T.A. Kontorova and Ya.I. Frenkel, Zh. Eksp. Teor. Fiz. **8**,89 (1938).
- [8] S. Aubry, in *Solitons and Condensed Matter Physics*, edited by A.R. Bishop and T. Schneider (Springer-Verlag, Berlin, 1979), pp. 264–278.
- [9] J. Hubbard, Phys. Rev. B **17**, 494 (1978).
- [10] M.E. Fisher and W. Selke, Phys. Rev. Lett. **44**, 1502 (1980).
- [11] P. Bak and R. Bruinsma, Phys. Rev. Lett. **49**, 249 (1982).

- [12] M. Mandelbrot, *The Fractal Geometry of Nature* (Freeman, San Francisco, 1982).
- [13] B.D. Krack, V. Ozolins, M. Asta, and I. Daruka, Phys. Rev. Lett. **88**, 186101 (2002).
- [14] E.D. Tober, R.C.F. Farrow, R.F. Marks, G. Witte, K. Kalki, and D.D. Chambliss, Phys. Rev. Lett. **81**, 1897 (1998).
- [15] P. Pieranski, P. Sotta, D. Rohe, and M. Imperor, Phys. Rev. Lett. **84**, 2409 (2000).
- [16] D.F. McMorrow, D. Gibbs, and J. Bohr, in *Handbook on the Physics and Chemistry of Rare Earths*, edited by K.A. Gschneidner and L. Eyring (Elsevier, Amsterdam, 1999), p. 169.
- [17] R.A. Cowley *et al.*, Phys. Rev. Lett. **66**, 1521 (1991); J.M. Tranquada *et al. ibid.* **73**, 1003 (1994).
- [18] M. Hupalo, J. Schmalian, and M.C. Tringides, Phys. Rev. Lett. **90**, 216106 (2003).
- [19] M. Nielsen, J. Als-Nielsen, J. Bohr, and J.P. McTague, Phys. Rev. Lett. **47**, 582 (1981).
- [20] S.C. Fain, Jr., M.D. Chinn, and R.D. Diehl, Phys. Rev. B **21**, 4170 (1980).
- [21] Ch. Kumpf, O. Bunk, J.H. Zeysing, M.M. Nielsen, R.I. Johnson, and R. Feidenhansl, Surf. Sci. **448**, L213 (2000).
- [22] T.L. Chan, C. Z Wang, M. Hupalo, M.C. Tringides, Z.Y. Lu, and K.M. Ho, Phys. Rev. B **68**, 045410 (2003).
- [23] S. Stepanovsky, V. Yeh, M. Yakes, M. Hupalo, and M.C. Tringides (unpublished).
- [24] M. Hupalo, V. Yeh, L. Berbil-Bautista, S. Kremmer, E. Abram, and M.C. Tringides, Phys. Rev. B **64**, 155307 (2001).
- [25] M. Hupalo, T.L. Chan, C.Z. Wang, K.M. Ho, and M.C. Tringides, Phys. Rev. B **66**, 161410(R)(2002).
- [26] L. Seehofer, G. Falkenberg, D. Daboul, and R.L. Johnson, Phys. Rev. B **51**, 13503 (1995).
- [27] A. Petkova, J. Wollschlager, H.-L. Gunter, and M. Henzler, Surf. Sci. **471**,11 (2001).
- [28] K. Horikoshi, X. Tong, T. Nagao, and S. Hasegawa, Phys. Rev. B **60**, 13 287 (1999)

CHAPTER 4: PHASE DIAGRAM OF Pb/Si(111) FOR $1.2 \text{ ML} < \theta < 1.33 \text{ ML}$

S. Stepanovskyy,¹ M. Yakes², V. Yeh³, M. Hupalo⁴ and M.C. Tringides⁵

(Based on an article published in *Surface Science*, **600**, 1417 (2006))

Abstract

We have created a new phase diagram for the system Pb/Si(111) for coverage $1.20 < \theta < 1.33$ using STM and SPA-LEED. This phase diagram shows a number of interesting new features, including the temperature dependence of a system which behaves according to the “devil’s staircase” rules. In addition, we have identified three different varieties of the hexagonal phase, as well as the disordered phase and the striped incommensurate phase.

Introduction

The Pb/Si(111) system is one of the most explored metal-semiconductor interfaces due to its rich phase diagram with many interesting properties. At low coverage there is a mosaic phase with $\theta = 1/6 \text{ ML}$ [1] and the $\sqrt{3} \times \sqrt{3}$ - β phase with $\theta = 1/3 \text{ ML}$. [2,3] At higher coverage ($\theta = 2 \text{ ML}$), three-dimensional islands form, which have flat tops and steep edges. [4,5] There has also been a great deal of experimental effort put into the intermediate coverage, however there is still some debate as to the composition of the phase diagram near $\theta = 4/3 \text{ ML}$, where the $\sqrt{3} \times \sqrt{3}$ - α phase forms. [6-8]

One interesting feature of the Pb/Si (111) system which has been recently discovered are the linear phases which were found that at low temperature and coverage $1.2 \text{ ML} < \theta < 1.33 \text{ ML}$. [9-10] Each of these linear phases consist of unit cells containing different combinations of two phases, the $\sqrt{7} \times \sqrt{3}$ phase (ideal coverage $\theta = 6/5 \text{ ML}$) and the dense $\sqrt{3} \times \sqrt{3}$ phase (ideal coverage $\theta = 4/3 \text{ ML}$). It was found that these phases behave according to the devil’s staircase model. From these two generating phases, an infinite number of unit cells (n,m) can be created, where n is the number of $\sqrt{7} \times \sqrt{3}$ cells and m is the number of $\sqrt{3} \times \sqrt{3}$ cells.

¹ Visiting Scientist from Lviv National University, Ukraine, conducted LEED experiments

² Graduate Student, involved in LEED experiments and analysis of LEED and STM data

³ Graduate Student, participated in LEED experiments

⁴ Staff Scientist, conducted STM experiments

⁵ Professor, author for correspondence

The devil's staircase (DS) is one of the outstanding predictions in theoretical physics, with a complex and fractal-like structure. A DS is an infinite set of phases, which are formed from a hierarchy of two generating phases in a narrow coverage interval. The DS arises from competing interactions within a system. In the Pb/Si(111) system the two competing interactions are the repulsive interactions from the lead atoms, and the periodic potential which comes from the silicon lattice.

Since the DS is strictly speaking true only at $T=0$, we are interested in the behavior of the staircase at finite temperatures.[11,12] Although there are examples of low temperature DS in other systems, there are very few examples in which the temperature dependence has been explored.[13,14] A primary goal of this work is to map out the thermal stability of a DS system. We are also interested in the effects on the linear phases on other phases which exist in the same coverage interval, namely the Hexagonal Incommensurate (HIC) and Striped Incommensurate (SIC) phases.

The diffraction experiments were carried out in a UHV system equipped with a SPA-LEED diffractometer, an Auger spectrometer and a mass spectrometer. The staircase itself provides a very fine flux calibration from the relation between the period q of a phase and its coverage $\theta(q)$. The STM experiments were carried in a different UHV system but under similar control conditions (of coverage and temperature) as in the diffraction experiments. The starting point was the $\sqrt{7}\times\sqrt{3}$ phase prepared at $T=120\text{K}$ and different annealing recipes were followed to investigate different regions of the phase diagram.

Phase Diagram And Observed Phases

Figure 1 shows a schematic phase diagram for the Pb/Si(111) for coverage range $1.2 < \theta < 1.33$. This phase diagram shows a number of new phases not seen in previous works.[6,8] In the most recent phase diagram published by Horikoshi *et al*, at low temperatures the $\sqrt{7}\times\sqrt{3}$ phase was identified for coverage $\theta < 1.22$, the $\sqrt{43}\times\sqrt{3}$ ((2,1) in our notation) phase was identified for $1.22 < \theta < 1.3$, and the SIC phase was identified for $\theta > 1.3$. At high temperatures, the HIC phase was identified as well as the SIC phase at higher coverage and higher temperatures. The phase diagram proposed in figure 1 represents phases prepared in a slightly different fashion to the previous phase diagrams in this coverage

region. The previously cited works deposited the entire coverage of lead in one step. For all phases in this work an intermediate $\sqrt{7} \times \sqrt{3}$ phase was prepared by depositing 1.2 ML of Pb on the

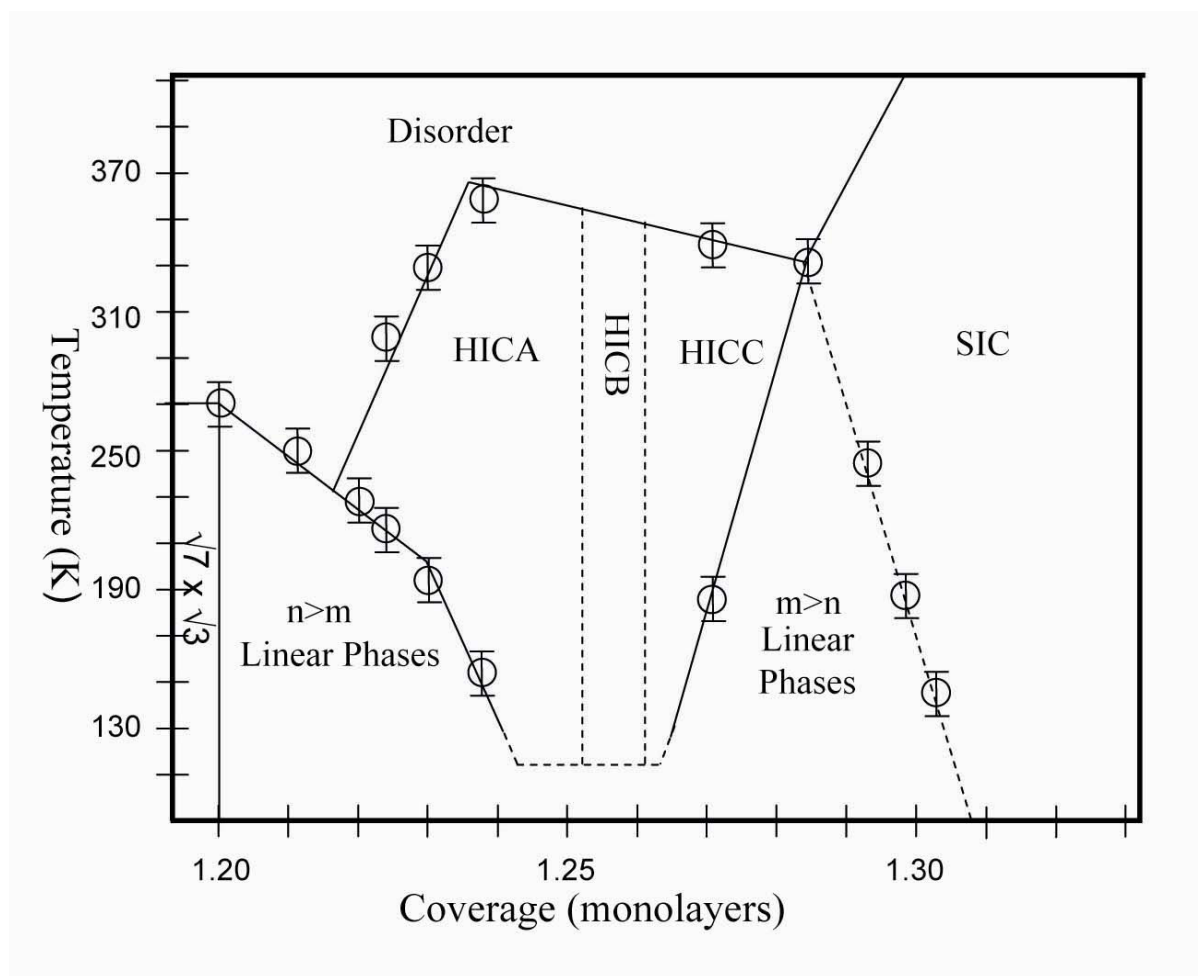


Figure 1: T- θ phase diagram for Pb/Si(111) in the coverage range $1.2 < \theta < 1.33$. In this phase diagram there is DS of linear phases, three different hexagonal phases as the temperature is increased, and the meandering “SIC” phase at highest coverages. As the temperature is increased these phases evolve into a disordered phase with a 1×1 diffraction pattern.

surface and annealing to 500 K then cooling to low temperature before depositing additional lead, annealing to 500 K and cooling again to reach our final phase.

The phase diagram in figure 1 shows many features not observed in previous phase diagrams. At low temperature and coverage $1.2 < \theta < 1.3$, we see the devil's staircase linear phases. The circles on the diagram indicate transition temperatures seen in experiment, determined from diffraction intensity vs. annealing temperature at constant coverage. These transition temperatures were confirmed with STM images at regular temperature intervals and constant coverage. The DS linear phases form a U-shaped curve of transition temperatures to different types of HIC phases between coverages $1.22 \text{ ML} < \theta < 1.29 \text{ ML}$. The HIC phase was found to be a family of phases whose periodicity and unit cell size change with increasing coverage. In addition, consistent with previous experiments, at coverage higher than $\theta = 1.29 \text{ ML}$, the linear phases transition to the SIC phase. At high temperatures phases at all coverages transition to the disordered phase which gives a (1×1) SPA-LEED diffraction pattern.

Figure 2 shows many examples of linear phases prepared by annealing lead with coverage $1.2 < \theta < 1.33$ to $T = 500 \text{ K}$ and cooling. Shown are the $\sqrt{7} \times \sqrt{3}$ phase ($\theta = 1.2$), the $(6,1)$ phase ($\theta = 1.212$), the $(3,1)$ phase ($\theta = 1.222$), the $(2,1)$ phase ($\theta = 1.231$), and the $(1,3)$ phase ($\theta = 1.286$). As the coverage of each phase increases, the size of the triangles near $(\frac{1}{3}, \frac{1}{3})$ decrease. The triangle around each pattern represents the triangle connecting the 6 spots of the $\sqrt{7} \times \sqrt{3}$ phase and is used as a guide to the eye to see the decreasing size of the triangle for each phase as coverage increases. Unlike the surface created at low temperature, by annealing to high temperatures the surface is covered with a single phase and not a mixture of two or more DS phases. This is identified by the absence of the "streaky spots" shown in phases created with low temperature deposition,[10] which were due to the superposition of two or more DS phases in the 2-D pattern. It appears that the orientation of the pattern for the $(1,3)$ phase, shown in figure 2(e) is different than for other phases of lower coverage. Figure 2(f) and 2(g) show close-up scans of the diffraction pattern near the $(\frac{1}{3}, \frac{1}{3})$ spot for the $(3,1)$ and $(1,3)$ linear phase. In each case there is a triangle, however, the $(1,3)$ triangle appears inverted with respect to the others. In addition, the triangle height appears to be half of the expected distance from our simple relation for the $(1,3)$ phase. To

get more details on the locations and intensities of the spots within the diffraction patterns we can use one-dimensional scans.

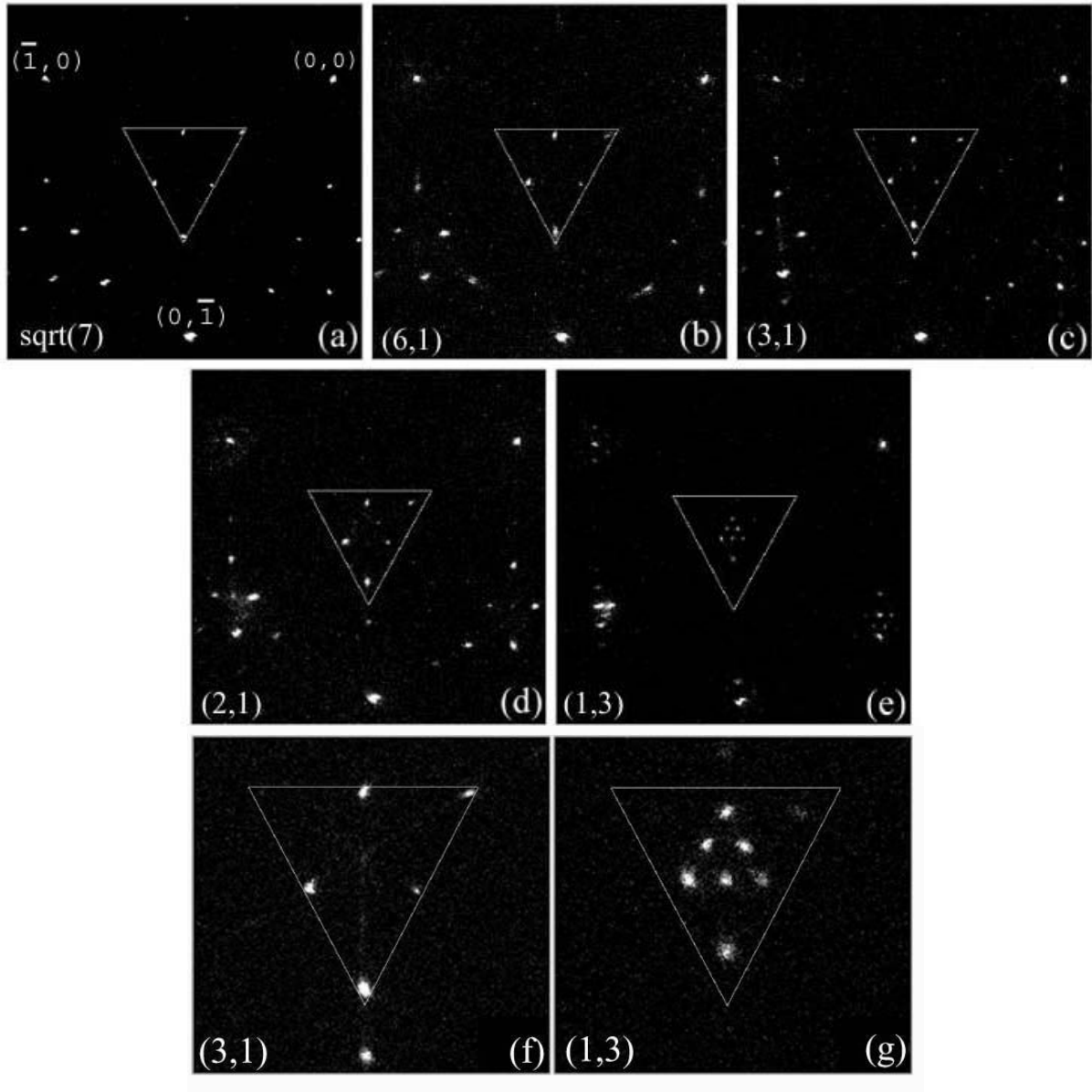


Figure 2: (a-e) 120% BZ scans of different (n,m) linear phases in the coverage region $1.2 < \theta < 1.33$ ML. (f-g) 40% scans of the $(3,1)$ and $(1,3)$ phases centered on $(1/3, 1/3)$ showing the flipping of the triangles and decrease of triangle height as the coverage increases above $q=1.25$ ML.

Before discussing the details of the diffraction pattern, it is useful to describe the expected diffraction patterns for each of the phases in our phase diagram. The diffraction

patterns for the linear and hexagonal phases were calculated kinematically. The diffracted intensity is given as:

$$I_{total}(k_x, k_y) = |F_{unitcell} \sum_{l,s}^{N_x, N_y} \exp(ik_x \cdot lb_1 + k_y \cdot sb_2)|^2 .$$

The diffraction pattern is the product of two terms, the term $F_{unitcell}$ which is dependant on the locations of the atoms within the unit cell multiplied by a reciprocal lattice of δ -functions from the long-range order, which is determined by the summation. The diffraction pattern for the linear phases is fully determined by the δ -function spots along $[1\bar{1}0]$ which are located at $(4\pi)k/a_0(5n+3m)$ where k is an integer determined by the identifying numbers (n,m) of each linear phase. Since there are three equivalent $[1\bar{1}0]$ directions which intersect at the commensurate positions at $(1/3, 1/3)$ and $(2/3, 2/3)$, the three patterns are superimposed. However due to the contributions of $F_{unitcell}$, not all spots have the same intensity. This leads to the triangle shaped pattern seen for the linear phases.

Intuitively, one expects the δ -function spots closest to the position of the ideal generating phases (i.e. the $\sqrt{7} \times \sqrt{3}$ phase has spots at multiples of $1/5$ and the $\sqrt{3} \times \sqrt{3}$ phase has spots at multiples of $1/3$) to be the strongest. It is convenient to define a triangle size H , which is determined by measuring the separation between the strongest spots along the $[1\bar{1}0]$ axis. For the $\sqrt{7} \times \sqrt{3}$ phase ($\theta=1.2$ ML), the triangle size is 34.6% BZ ($1/5 \cdot \sqrt{3} \cdot 100\%$ BZ). For the $\sqrt{3} \times \sqrt{3}$ phase ($\theta=1.33$ ML), the triangle size is 0. Using the kinematic calculations it can be shown that for every linear phase with $1.2 < \theta < 1.25$, the triangle height is determined by $H=34.6-259.5(\theta-1.2)$. [15] For $1.25 < \theta < 1.33$, the triangle height is half this value, due to the presence of two high symmetry sites in the unit cells which will be discussed more below. These definite relations between the triangle size and the values of n and m allow us to uniquely determine the phases present on a surface from the triangle shaped diffraction

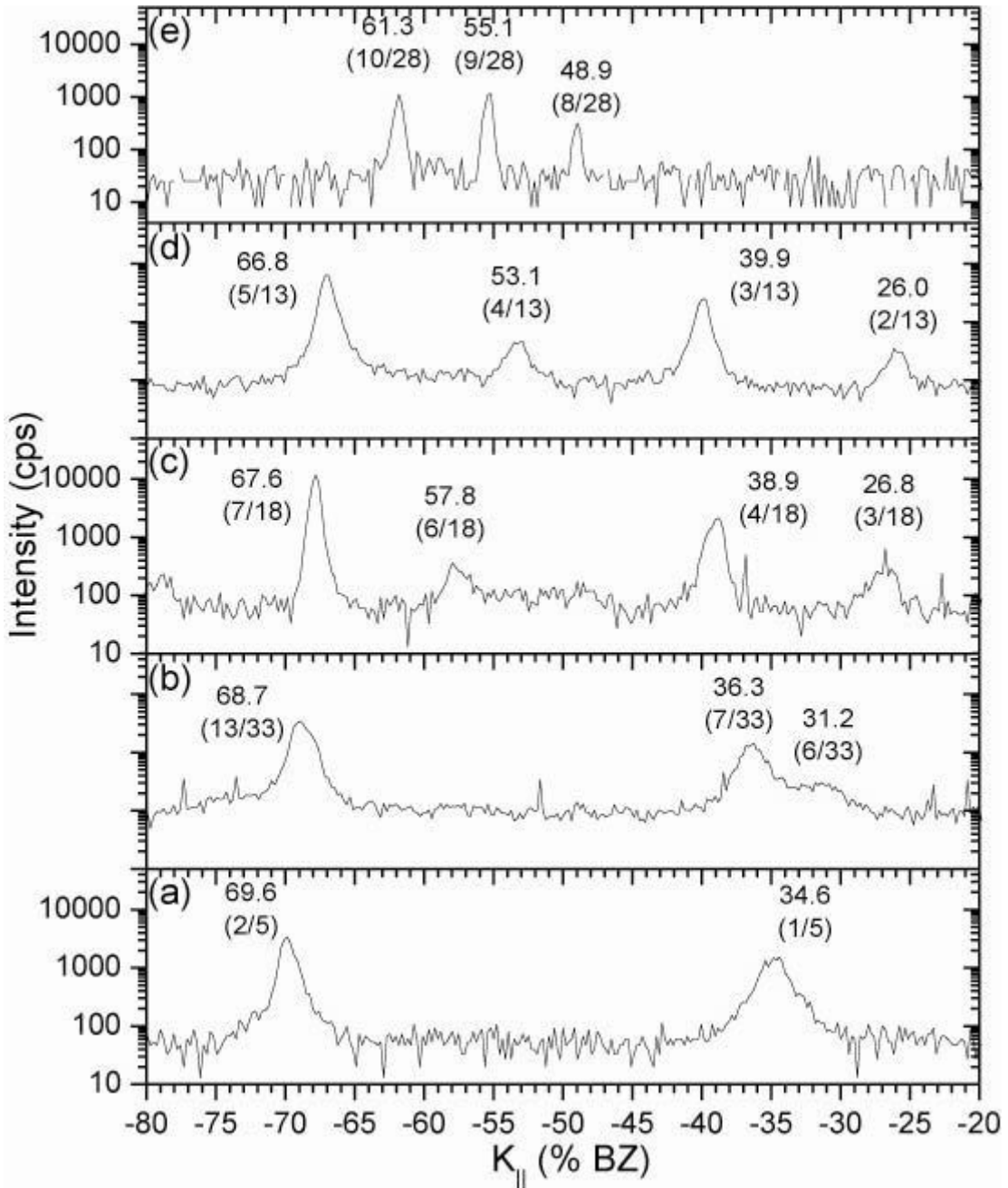


Figure 3: 1-D scans along the [110] direction in reciprocal space showing the DS phases seen in 2-D scans in figure 2(a)-(e). The decreasing characteristic triangle size H and the fractional identification of the spot positions can be used to identify the phases present.

pattern. Further support for the identification of each phase can be made by indexing weaker spots which should also be located at multiples of $(4\pi)k/a_0(5n+3m)$.

Figure 3 shows one dimensional scans along the $[1\bar{1}0]$ direction near the $(\bar{1}/3, \bar{1}/3)$ spot for the 2-dimensional patterns shown in figure 2. As mentioned above, the phase is determined by the triangle height H , which is defined as the distance in %BZ between the strongest spots near $(\bar{1}/3, \bar{1}/3)$. Further evidence for the existence of each phase can be given by indexing the weaker spots in the scan. For example, in Figure 3(c), the (3,1) phase, we expect δ -functions to occur at $1/18$ of the distance between (00) and $(\bar{1}\bar{1})$. This is due to the length of the unit cell being $5*3+3*1=18$ times the separation of Si atoms along that direction. We see that the strongest spots are at positions 67.8 and 38.8, giving a triangle height of 29.0% BZ. These spots correspond to $7/18$ and $4/18$ of 173% BZ respectively. This is in agreement with 28.9% BZ, the expected triangle height of the (3,1) phase. In addition we see weaker spots at 57.7, 48.5, and 27.0, which correspond to $6/18$, $5/18$, and $3/18$. The FWHM of 0.8% BZ indicates a domain size of greater than 400 Angstroms, showing that these phases exist over macroscopic distances.

As mentioned previously, having two nearly energetically equivalent high symmetry sites causes a major qualitative difference in the experimental diffraction pattern from the (3,1) phase to the (1,3) phase. These effects are to be discussed in detail in a future publication, so we will only outline the argument here. [16] STM images suggest that for phases with coverage less than 1.25 the high symmetry atoms are all located on one high symmetry site. For linear phases with coverage greater than 1.25 high symmetry atoms are located on both high symmetry sites. We know from STM images that the high symmetry sites only switch at the $\sqrt{7} \times \sqrt{3}$ cells within the unit cell.[9] This leads to phases with $\theta > 1.25$ ML having a unit cell which is twice the size of a cell which would happen if the atoms were only located on a single high symmetry site. This means that the separation of delta functions should be half of what is expected from the size of the (1,3) cell. The shift in sites also introduces extra terms in the F_{unitcell} portion of the kinematic calculation, due to the ~ 1 Angstrom shift in position from the H3 to T4 site. This rearranges the unit cell contribution in such a way that the delta functions nearest the $(1/3, 1/3)$ commensurate position become more prominent, instead of the delta functions, which form the triangular pattern seen for the $\theta < 1.25$ phases. The decrease in δ -function separation is observed in figure 3(e) where the

separation between the observed spots is $173\%/2(5*1+3*3)$ or 6.2%, half of what would be expected if all of the high symmetry atoms within the unit cell were located on a single high symmetry site.

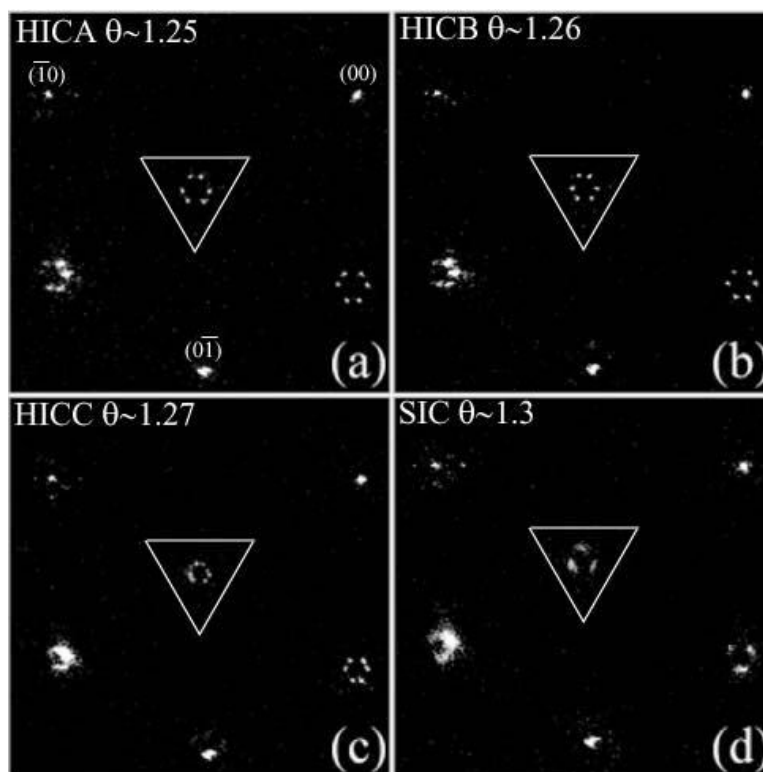


Figure 4: Experimentally observed diffraction patterns for HICA, B, and C phases and SIC phase. The decreasing hexagon size indicates increasing numbers of $\sqrt{3} \times \sqrt{3}$ cells within each hexagonal unit cell.

As the linear DS phases with coverage $1.22 < \theta < 1.29$ are annealed to higher temperatures, a family of HIC phases emerge. Figure 4 shows $120\% \times 120\%$ 2-D scans of three hexagonal phases as well as the SIC phase which is observed at higher coverage. For the hexagonal phases, a hexagon created from two rotated equilateral triangles is visible near the $(1/3, 1/3)$ and $(2/3, 2/3)$ positions. The equilateral triangles arise from the characteristic rhombic unit cell of the HIC phases. As the Pb coverage on the surface increases, the spots within each triangle get closer together. This indicates a larger unit cell with increasing coverage. Therefore we identify each pattern with increasing coverage as a different configuration in a family of hexagonal phases which we call HIC A, B, and C. Although the

models show that the HIC phases are commensurate, we refer to these phases “HIC” to avoid confusion with the previous convention.

In contrast to the diffraction patterns which come from the hexagonal phases, the pattern which comes from the SIC phase has a different structure. Instead of 6 distinct spots, the SIC pattern has three spots elongated along the reciprocal space $[112]$ directions. This elongation is due to the meandering domain walls of the SIC phase which have the effect of “smearing” the diffraction pattern.

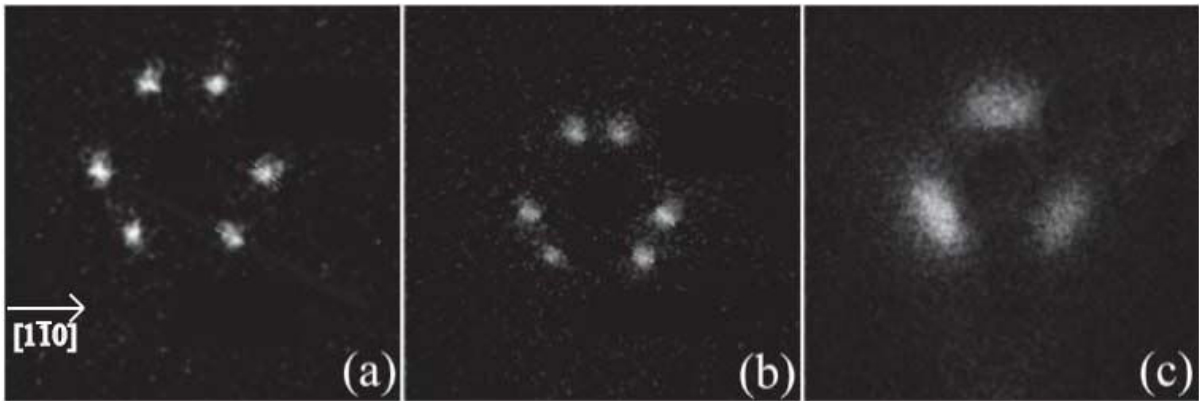


Figure 5: 20% diffraction patterns for the HICA (a), HICC (b), and SIC phases. The distance between spots within the same triangle and the rotation angle away from the $[112]$ direction are used to determine the size and orientation of each hexagonal unit cell.

By using the (10) Si spots as a reference and finding the coordinates of the most intense spots in the 2-D scan, we can measure the distance between the spots. Figure 5 shows 20% x 20% scans near the $(1/3, 1/3)$ position. We can use these scans to measure the separation of the spots from each triangle. The separation between each of the spots in each triangle is 8.0% for hexagonal A, 7.3% for hexagonal B and 6.3% for hexagonal C. The error is $\pm 0.5\%$ BZ for each measurement. The error was determined from the accuracy of determining the deflection voltage in SPA-LEED experiments. This is consistent with the model described above. The close-up scans clearly demonstrate the difference between the two configurations of hexagonal phases and between the HIC and SIC phases.

In order to explain the diffraction pattern due to the family of hexagonal phases we extend the model proposed by Hupalo et al.[17] In this model, the HIC phases consist of

triangular domains of $\sqrt{3} \times \sqrt{3}$ domains separated by “almost $\sqrt{7} \times \sqrt{3}$ ” domain walls. Unlike regular $\sqrt{7} \times \sqrt{3}$ cells where the high symmetry atoms are all located on the same site (i.e all H3 or all T4), the “almost $\sqrt{7} \times \sqrt{3}$ ” cells have atoms which switch sites across the unit cell. This unit cell is the same as the unit cell which causes the binding site switch in the linear phases. Figure 6 shows a schematic diagram of the HIC B phase which is based on the model of the HIC A phase proposed in ref. 17. In this phase there is a triangular domain of $\sqrt{3} \times \sqrt{3}$ unit cells with 28 high symmetry atoms located on H3 sites and another triangular domain of $\sqrt{3} \times \sqrt{3}$ unit cells with 21 atoms located on T4 sites. In contrast the model for the HIC A phases has 21 atoms and 15 atoms in the H3 and T4 domain respectively. The asymmetry in triangle size and the “almost $\sqrt{7} \times \sqrt{3}$ ” causes a rhombic unit cell with lattice vectors rotated 4.1° away from the $[\bar{1}\bar{1}2]$ direction for the HIC B phase.

We can calculate the expected diffraction pattern for the hexagonal phases using the kinematic approximation as in the linear phases, but we use the rhombic unit cells of various sizes to account for the different HIC unit cells. Because the HIC phase is primarily constructed from $\sqrt{3} \times \sqrt{3}$ domains, the most intense spots should be nearest the $(1/3, 1/3)$ positions. The unit cell contribution and rhombic unit cell forming an equilateral triangle near the $(1/3, 1/3)$ and $(2/3, 2/3)$ positions. A schematic diagram of the expected pattern is shown in figure 6. The size of the triangle and its orientation are dependent only on size and orientation of the unit cell. Due to the mirror symmetry in the system, there are two possible orientations of each HIC configuration, the second configuration is simply the first configuration reflected about the $[\bar{1}\bar{1}2]$ axis. The diffraction pattern is composed of two equilateral triangles centered near the $(1/3, 1/3)$ and $(2/3, 2/3)$ positions, each of which are reflections of the other, as shown in the schematic diagram at the bottom of figure 6. This description matches the description of the experimental diffraction pattern.

From the schematic diagram and the experimental results we can determine the size and rotation for each unit cell. The separation between each of the spots in each triangle is 8.0% for hexagonal A, 7.3% for hexagonal B and 6.3% for hexagonal C, which correspond to real space distances of 48.0 Å, 52.6 Å, and 61.0 Å respectively. The rotation angles of the lattice vectors measured with diffraction are 5.4, 4.3 and 3.0 degrees, +/- 1.5 degrees. The

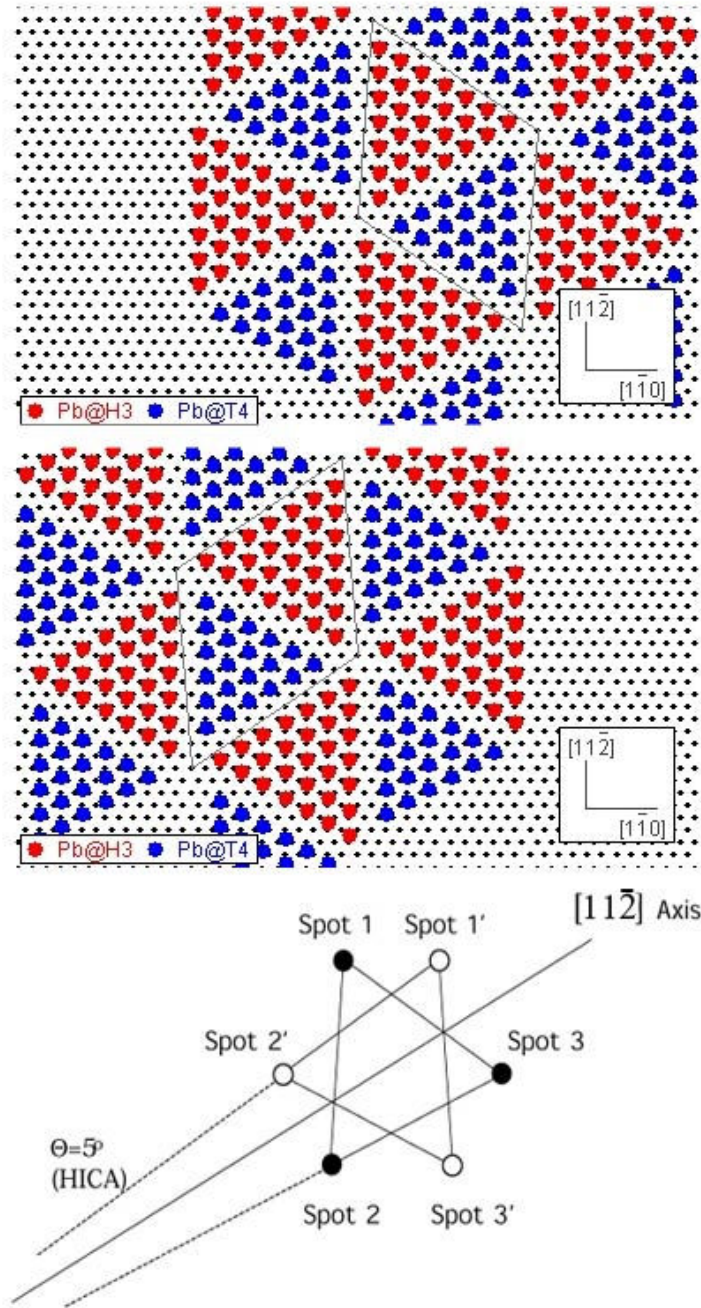


Figure 6. Schematic models of the HIC phase showing mirror symmetry about the $[11\bar{2}]$ direction. Each orientation gives rise to three diffraction spots which form an equilateral triangle. The two patterns combined lead to the diffraction patterns observed in diffraction.

rotation angles match the rotation angle of the primary unit cell vectors with respect to the $[11\bar{2}]$ real space lattice. From the models we predict a unit cell size and rotation angle of

46.7 Å and 4.7° for HIC A, 53.3 Å and 4.1° for HIC B, and 58.9 Å and 3.7° for HIC C, in good agreement with the experimentally determined values.

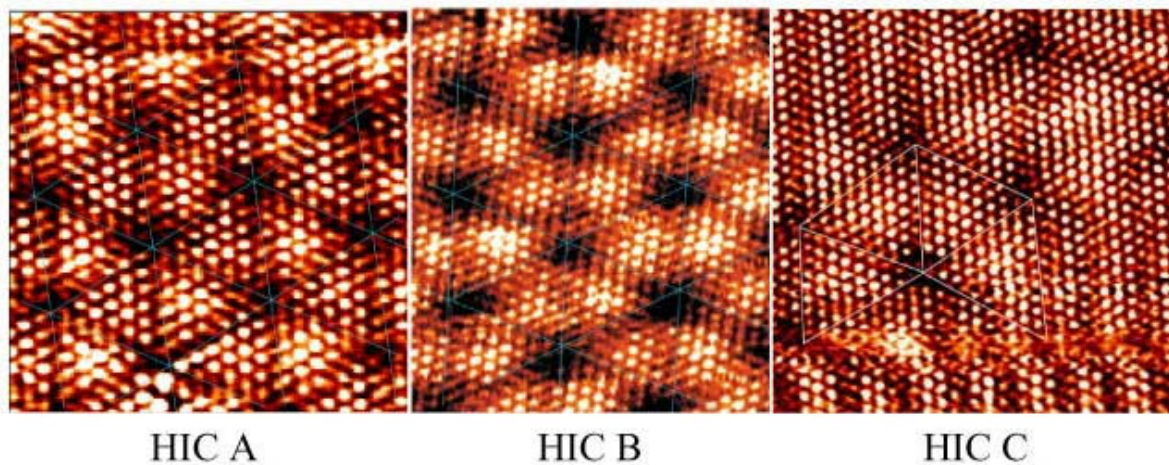


Figure 7: STM images of the HICA, B, and C phases. The scan sizes are 8.8 x 6.6nm², 14.4 x 7.2 nm² and 12 x 12 nm² as you move from right to left. As the coverage of each phase increases more white circles are present within each unit cell. This indicates more high symmetry atoms within each unit cell, confirming the models shown previously.

The three types of hexagonal phases have also been observed with STM, as shown in figure 7. This figure shows the expected effect from diffraction, i.e., the size of the unit cell increases as we change from hexagonal A to B to C. The identification of each phase is done by measuring the length of each unit cell. This measurement gives length 47.2, 54.5 and 62.5 Angstroms respectively, in agreement with the diffraction images. In addition we can verify our model by counting the number of “blobs” along each boundary of each unit cell domain. Each blob should signify a high symmetry atom within each $\sqrt{3} \times \sqrt{3}$ unit cell. This counting gives 6 and 5 for the HIC A cell, 7 and 6 for HIC B and 8 and 8 for HIC C, in good agreement with our models. The good agreement between STM and SPA-LEED is excellent evidence for the existence of a family of HIC phases in our phase diagram.

Phase Transitions

To determine the critical temperature of each phase in the phase diagram of figure 1, we took a given DS phase prepared by high temperature annealing, and cooled back to ~120 K. The sample was then heated to various temperatures in succession to observe the phase

transition. The system was annealed to the desired temperature with a heating time of approximately 10 minutes. The system was allowed to equilibrate for an additional 15 minutes, then one and two dimensional scans were taken in order to characterize the surface.

Figure 8 shows one dimensional scans taken near $(\frac{1}{3}, \frac{1}{3})$ as we anneal the (2,1) phase from 136 K to 378 K along the $[11_0]$ reciprocal space direction. Specifically this is the (2, 1) to hexagonal phase transition. The (2,1) phase has length $(2 \cdot 5a/2) + (1 \cdot 3a/2) = 13a/2$ in the $[110]$ direction, where a is the lattice constant of Si(111). This means that a delta function will be located every $(\sqrt{3}/2)/(13/2) = 13.3\%$ BZ along the $[11_0]$ reciprocal direction. We can show from a kinematic calculation that the most intense delta functions near the $(\frac{1}{3}, \frac{1}{3})$ commensurate position should be the $3/13$ and $5/13$ spots, giving a triangle height of 26.6% BZ. This system was prepared by annealing 1.23 ML of Pb on Si to 500 K, then cooling to low temperature. At $T=136$ K, the system is in the (2,1) phase with no evidence of the HIC phase present in 1-D or 2-D scans. The (2,1) phase can be identified by the triangle height of 26.9 % BZ in good agreement with the expected triangle height of 26.6% for the (2,1) phase, as well as the weaker spots located at 53.1% ($4/13$) and 26.0% ($2/13$).

As the temperature is increased, a new spot appears in the 1-D scan at 63.0% BZ. We can see from the 2-D patterns that this belongs to the hexagonal phase, and we believe that this spot is the projection of the two spots nearest the $[11_0]$ axis onto that axis. From the model given by Hupalo et al.[17], we can calculate the projection using the twist angle of 4.7 degrees and the 8.2%BZ separation between delta functions, which comes from the 46.7 Angstrom size of the unit cell. From these two numbers, we can find the expected projection, located at 62.0%BZ. As in two dimensions, in the $T=186$ K and $T=202$ K scans, we see coexistence between the two phases, however, due to the short equilibration times in our experiment, it is unclear whether or not this is a thermodynamically stable or metastable coexistence.

At $T=216$ K, the linear phase has disappeared and only the hexagonal phase is present on the surface. The 63.0% spot intensity increases to its maximum at ~ 300 K, then decreases with continued heating. At $T=362$ K, the 63% spot disappeared and the pattern

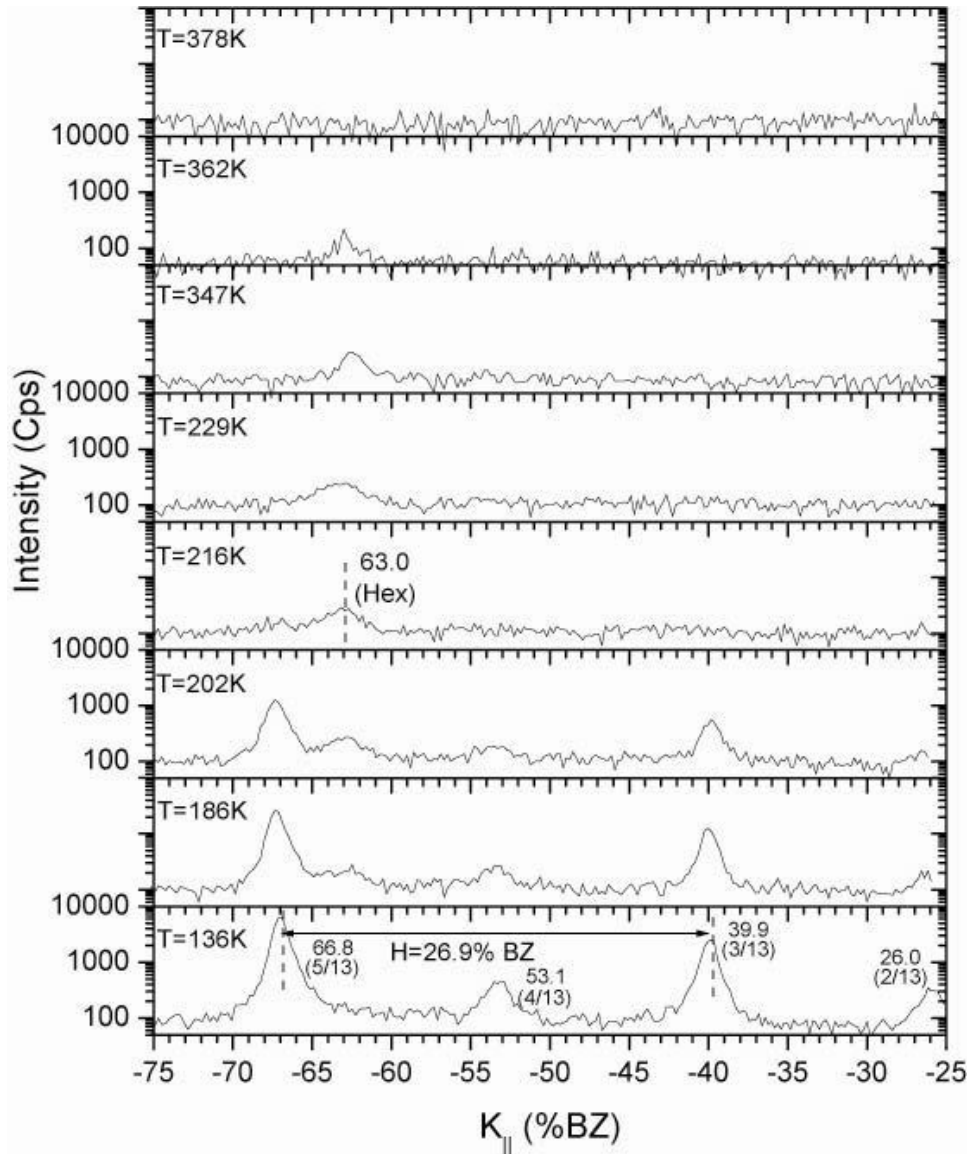


Figure 8: 1-D scans along the $[112]$ direction as the surface temperature is increased. Initially the surface consists of only the $(2,1)$ phase, but with increasing temperature the HIC A phase and disordered phase eventually appear.

shows no spots, indicating the 1×1 or disordered phase. After cooling again to low temperature, the system returns to the $(2,1)$ phase, but the spots have a lower intensity.

Figure 9 shows STM images illustrating this transition. At 150 K, the surface is completely covered with the $(2,1)$ phase. At 155 K we see the initial nucleation of the HIC phase. By 190 K there is coexistence between the hexagonal A and linear phases. The dark spots which are circled in the figure are defects which can be used to verify that the same

portion of the surface is being probed with increasing temperature. As in the diffraction images above, it is unclear whether or not the coexistence we see in these STM images indicate a thermodynamically stable coexistence between the two phases or a metastable state.

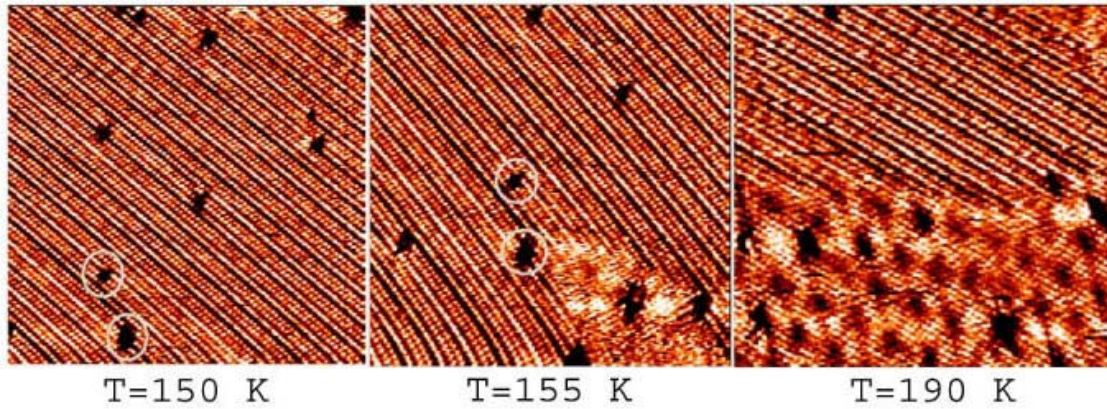


Figure 9: 43 x 43 nm STM images showing the transition of the (2,1) phase to the HIC A phase with increasing temperature.

The linear to hexagonal phase transition seen in figure 8 is shown in more detail in Figure 10. The spot intensities of the 67% spot (the most intense spot belonging to the (2,1) linear phase), and the 63% spot (the most intense spot belonging to the hexagonal phase) are shown in Figure 10. The critical temperature is defined as the temperature where the diffraction spot intensity is 20% of the maximum intensity. The value of 20% was chosen such that the critical temperature of 270 K for the $\sqrt{7} \times \sqrt{3}$ matches previous experiments done by other groups. We can see the trend that is shown in the one-dimensional scans that the intensity of the linear phase spots decreases as the temperature increases, while the hexagonal phase spot intensity increases. We can also see that at temperatures near the transition temperature, the two phases will coexist. This figure also shows the hexagonal to disordered phase transition near $T=350$ K.

Figure 11 shows relative diffraction spot intensities for the strongest spots of many linear phase transitions. The transition temperatures from this diagram were used to construct the phase diagram in Figure 1. Each transition temperature in the phase diagram is

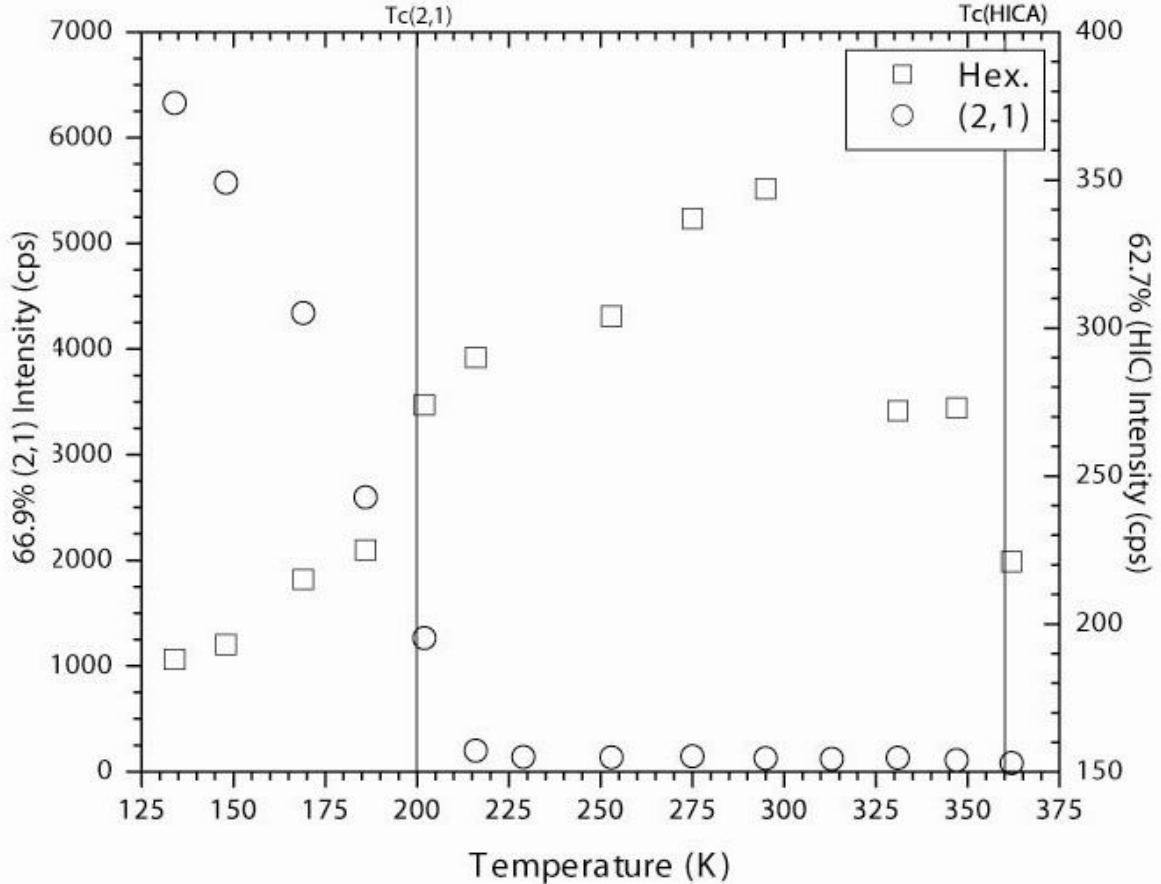


Figure 10: Intensity of the strongest spots for the (2,1) linear phase and the Hexagonal phase. Transition temperatures are defined as 20% of the original spot intensity in order to behave like earlier models.

then from the point where the most intense spot has 20% the maximum intensity. The coverage for each phase is given by $\theta = (6n+4m)/(5n+3m)$. We see that as the phase increases in coverage from the $\sqrt{7} \times \sqrt{3}$ phase to the (3,2) phase, the transition temperature decreases. These phases all have $n > m$ or $\theta < 1.25$. As the coverage increases from $\theta = 1.25$, consisting of the phases where $n < m$, the transition temperature increases with coverage. The (1,3) phase has the highest transition temperature of any of the DS phases.

From a simple mapping to the 1-D lattice gas system it might be expected that the phase diagram would be symmetric with respect to coverage. This is clearly not the case, the transition temperature seems to decrease with increasing coverage for linear phases with $n < m$, whereas the (1,3) phase has the highest observed transition temperature for phases with

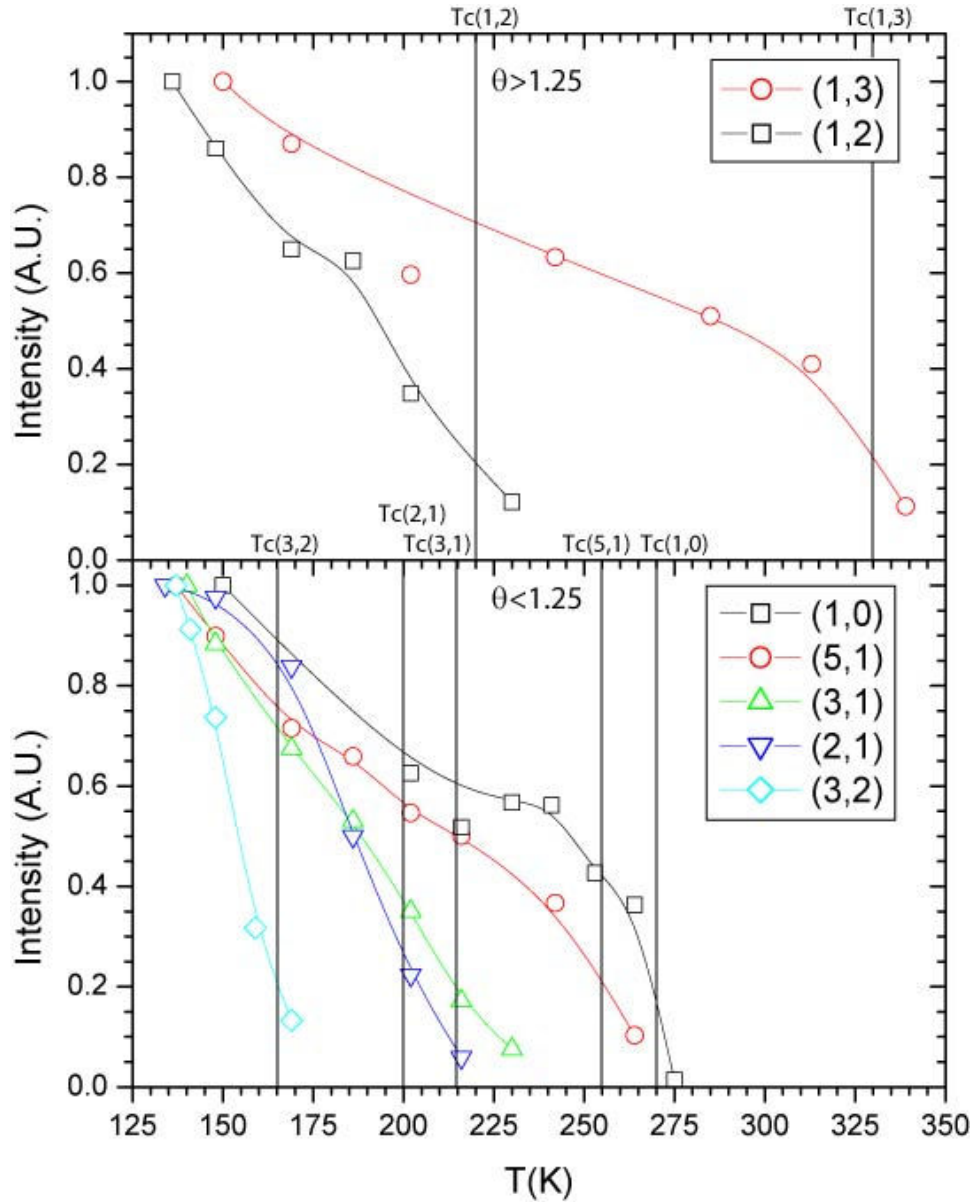


Figure 11: Spot intensity maxima for 7 recorded DS phases. The colored lines are intended as a guide for the eye.

$m > n$. It also might be expected that T_c would decrease with increasing coverage due to increasing long range Pb-Pb repulsion due to strain within the lead layer. The reentrant stability of the (1,3) phase disproves this argument. However, there are added complexities of the Pb/Si(111) system not seen in the simple theoretical model; the hexagonal phases, the SIC phase, the H3-T4 lattice site shift. It is clear that these features have a profound effect

on the phase diagram. More theoretical work regarding these features of the real system is necessary to fully understand the physics of the real system.

Low Temperature Deposition

In a complimentary work,[10] it was determined that the optimal kinetic pathway to produce DS phases which extend over macroscopic distances is to deposit lead atoms onto the $\sqrt{7} \times \sqrt{3}$ surface at $T=120$ K. Such a procedure allows you to see more than 15 linear phases, with coverage $1.20 < \theta < 1.33$. It is interesting to examine if and how the phases present on the surface will change with annealing if you create DS phases at low temperature as compared to creating phases by annealing to high temperature.

Figure 12 shows 1-D scans along $[1\ \bar{1}0]$ for coverages $\theta = 1.22$ ML made by each method. At $T=140$ K, the equilibrium phase has much sharper diffraction spots, however, each maximum is located at the same (3,1) peak positions of 67.9 and 39.0, as in the (3,1) scans above. The primary phase present on each surface, the (3,1) phase, is identified from the triangle height of 28.7%. Initially the surface prepared at low temperature has broader diffraction spots which indicate multiple phases are present on the surface. However, as the surface is heated to near the (3,1)->hexagonal transition temperature of $T=220$ K, the extra phases present on the non-equilibrium scan are reduced. This means that less stable phases at the surface coverage have lower transition temperatures than the primary (3,1) phase. It is important to note that phases the primary phases created by each method have the same transition temperature. For example, in Figure 12, the (3,1) phase shifts to the hexagonal phase at the same temperature regardless of preparation method. Also, each phase is left with a spot at 63.0%, which indicates that both preparation methods turn into the HICA phase. We found that all linear phases created by low temperature deposition behave similarly to the phases created on surfaces annealed to high temperature. However, there is one key difference. If you deposit lead at $T=120$ K, instead of seeing the SIC phase at coverage $\theta=1.28$ as in experiments where the sample has been annealed, linear phases with coverage up to $\theta \sim 1.33$ can be formed at low temperature.

This effect is illustrated in Figure 13. At low temperature the surface is prepared with a DS phase near the coverage of the ideal $\sqrt{3} \times \sqrt{3}$ phase. This surface was formed by

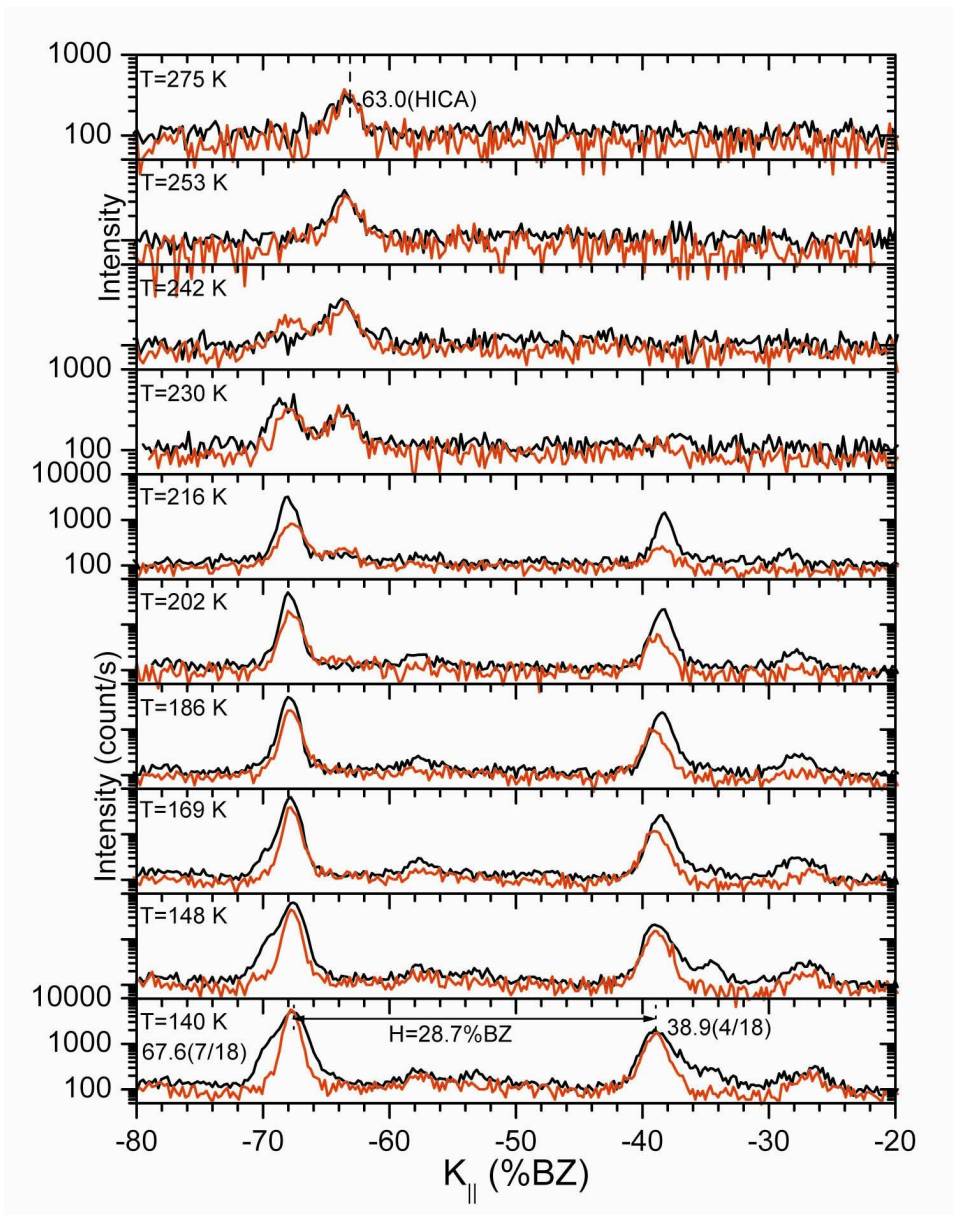


Figure 12: Comparison of annealing of the (3,1) phase prepared by thermal annealing (red line) and low temperature deposition (black line). While the low temperature deposition gives broader spots due to the coexistence of different phases, the transition temperature is the same for both preparation methods.

depositing 0.13 ML of lead on the $\sqrt{7} \times \sqrt{3}$ phase at $T=120$ K. We see one broadened primary spot near 57.7% BZ (1/3). The spot broadening is likely due to the presence of high m linear phases which would have small but non-zero triangle heights. As the sample is annealed, the triangle size will increase, indicating DS phases of lower coverage. At $T=275$ K, the mostly $\sqrt{3} \times \sqrt{3}$ surface has been replaced with a surface covered mostly with the (1,3)

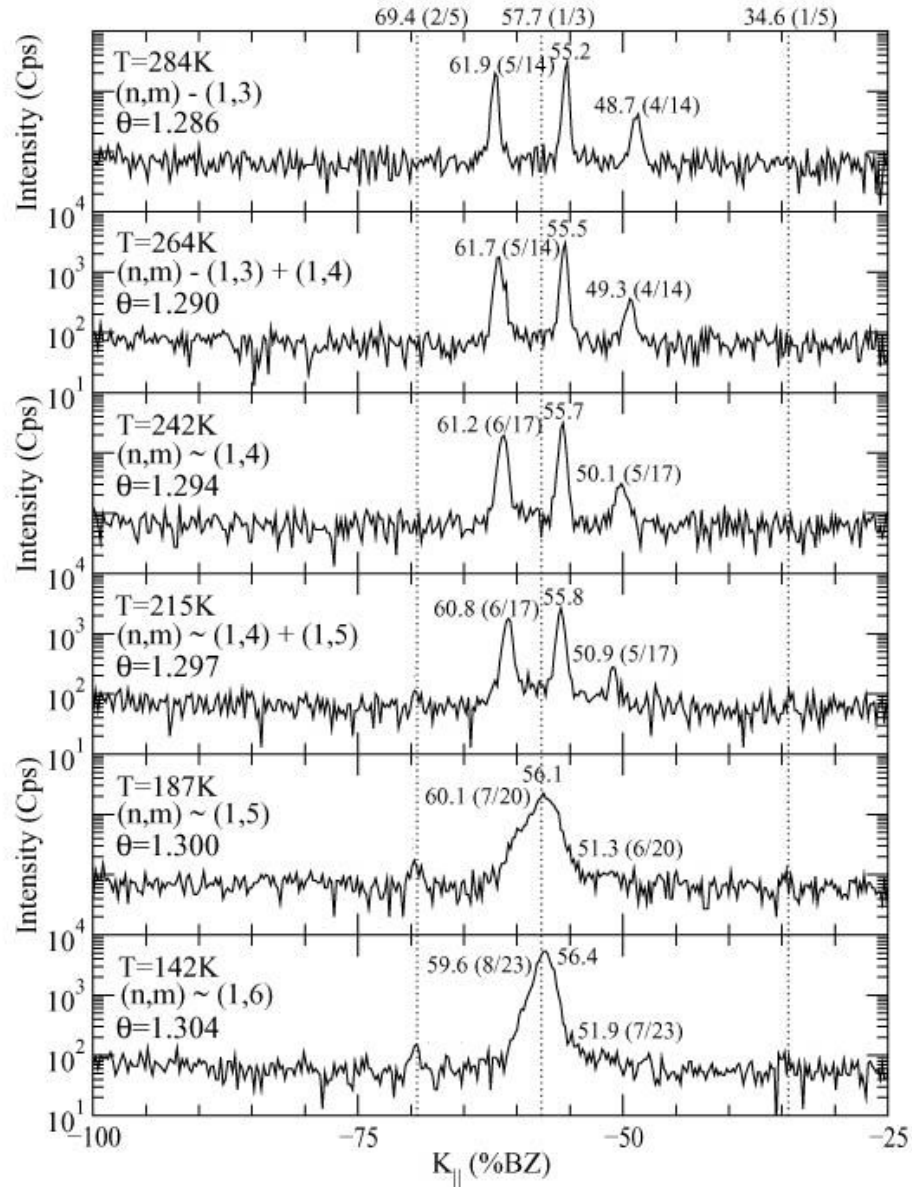


Figure 13: Mild thermal annealing to room temperature of an initial (1,6) phase formed with low temperature (120 K) deposition. As the temperature increases the coverage of the DS phase decreases until the (1,3) phase appears. This phase is stable upon cooling to 130 K. This indicates that a small amount of lead has been lost irreversibly to the steps.

linear phase, a coverage change of $\Delta\theta=0.04$. We believe the driving force of this phase transition is the dependence of the stability of DS phases on the period of the phase. For $\theta>1.25$, phases of higher coverage have higher period, and are therefore less stable and we would expect them to have a lower transition temperature.

Summary

As noted elsewhere, this devil's staircase can be reproduced by a one-dimensional Ising model with long range convex interactions, in this case Coulombic interactions.[9,20-22] We have not found any theoretical work done on this particular problem, however, the work done on temperature dependence of other devil's staircase systems does not seem to map correctly to this problem.[11-13,23,24] One result which is not intuitive is that the critical temperature of this does not depend on the $T=0$ stability curve. For instance, the (5,1) phase has a much smaller stability in μ than the (2,1) phase, however, its critical temperature is higher by 50 K. Although we can model this system by the one-dimensional Ising model, the real system is more complex due to the existence of the two high symmetry sites as well as the SIC and Hexagonal phases. It is possible that it is these factors that prevent the system from behaving similarly to other models.

We have created a new phase diagram for the system Pb/Si(111) for coverage $1.20 < \theta < 1.33$ ml. This phase diagram shows a number of outstanding new features, including the temperature dependence of a system which behaves according to the "Devil's Staircase" rules. In addition, we have identified three different varieties of the hexagonal phase.

References

- [1] E. Ganz, I.S. Hwang, F. Xiong, S.K. Theiss, and J. Golovchenko, Surf. Sci **257**, 259 (1991)
- [2] E. Ganz, F. Xiong, I. S. Hwang, and J. Golovchenko, Phys. Rev. B, **43**, 7316 (1991)
- [3] J.A. Carlisle, T. Miller, and T.-C. Chaing, Phys Rev. B, **45**, 3400 (1992)
- [4] H.H. Weitering, D.R. Heslinga, and T. Hibma, Phys. Rev. B, **45**, 5991 (1992)
- [5] K. Budde, E. Abram, V. Yeh, and M.C. Tringides, Phys Rev. B, **61**, R10602 (2000)
- [6] L. Seehofer, G. Falkenberg, D. Daboul, and R. L. Johnson, Phys Rev. B **51**, 13503 (1995)
- [7] X. Tong, K. Horikoshi, and S. Hasegawa, Phys. Rev. B, **60**, 5653 (1999)
- [8] K. Horikoshi, X. Tong, T. Nagao and S. Hasegawa, Phys. Rev. B **60**, 13287 (1999)
- [9] M. Hupalo, J. Schmalian, and M.C. Tringides, Phys Rev. Lett. **90**, 216106 (2003)
- [10] M.Yakes, V. Yeh, M. Hupalo, and M.C. Tringides Phys. Rev. B **69**, 224103 (2004)

- [11] S. Aubry in *Solitons and Condensed Matter Physics*, edited by A.R. Bishop and T. Schneider (Springer-Verlag, Berlin, 1979) pp. 264-278
- [12] V.L. Povrovsky et al in *Solitons*, edited by S.E. Trullinger, V.E. Zakharov, and V.L. Povrovsky (North-Holland, Amsterdam, 1986) pp. 71-128.
- [13] M. E. Fisher and W. Selke, *Phys Rev. Lett.* **44**, 1502 (1979)
- [14] K. Ohwada *et al.* *Phys Rev. Lett.* **87**, 086402 (2001)
- [15] V. Yeh, Ph.D Thesis
- [16] M. Yakes et al. (to be published)
- [17] M. Hupalo, T.L. Chan, C.Z. Wang. K.M. Ho and M.C. Tringides, *Phys Rev B*, **66**, 161410(R) (2002)
- [18] M.F. Reedijk, J. Arsic, D. Kaminski, P. Poodt, J.W. M van Kessel, W.J. Szweryn, H. Knops, and E. Vleig, *Phys. Rev. Lett.* **90**, 056104 (2003)
- [19] M. Hupalo, V. Yeh, L. Berbil-Bautista, S. Kremmer, E. Abram, and M.C. Tringides, *Phys. Rev. B*, **64**, 155307 (2001)
- [20] A.A. Slutskin, V.V. Slavin and H.A. Kovtun, *Phys Rev B*. **61**, 14184 (2000)
- [21] J. Hubbard, *Phys. Rev. B* **17**, 494 (1977)
- [22] P. Bak and R. Bruinsma, *Phys. Rev. Lett.* **49**, 249 (1982)
- [23] P. Bak and J. von Boehm, *Phys. Rev. B* **21**, 5297 (1979)
- [24] J. Villain and P. Bak, *J. Phys* **42**, 657 (1981)

**PART II: PROPERTIES OF QSE ISLANDS GROWN ON SI(111) SURFACES WITH
METAL ADSORBATES**

**CHAPTER 5: OVERAGE DEPENDENT ANISOTROPY IN FCC STACKING
SEQUENCE OF PB ISLANDS GROWN ON SI(111)-PB($\sqrt{3}\times\sqrt{3}$)- α PHASE**

M. Yakes¹, J. Chen², M. Hupalo³, and M.C. Tringides⁴

(Based on a paper to be submitted to *Physical Review B*)

Abstract

Pb islands were grown on the Si(111)- α phase at 180 K and coverages $1 \text{ ML} < \theta < 3 \text{ ML}$. Pb islands grown on the Si(111)- α phase display two corrugation patterns which are caused by the twin fcc stacking sequences. The fcc sequence for each type relative to the Si substrate has been identified from the step edge energies and from the observation of decoration rows which form at boundaries between islands of different types. In addition, the relative population of each island type is shown to change with increasing coverage and changing island morphologies.

Introduction

There has been a great deal of interest in the growth of reproducible self-assembled nanostructures with uniform size and geometry. These nanostructures have many potential uses in technological applications. One common method for producing these nanostructures is epitaxial growth of thin films on a crystalline substrate. The effect of the substrate on the growth material often introduces a variety of interesting new phenomena not seen in bulk growth.

A particular system which has attracted recent attention is the Pb/Si(111) system. The Pb/Si(111) system has shown a novel growth mode which consists of uniform height islands with flat tops and steep edges. [1-4] The height of the islands can be controlled using differing growth pathways in temperature, coverage, and substrate. The cause of the unusual growth mode of the Pb islands is believed to be related to the confinement of electrons in the direction of the surface normal. [5,6] This is usually referred to as the Quantum Size Effect (QSE).

¹ Graduate student, primary researcher

² Graduate student, participated in data analysis

³ Staff Scientist, conducted STM experiments

⁴ Professor, author for correspondence

Pb islands grown on the Pb/Si(111)- $\alpha\sqrt{3}\times\sqrt{3}$ phase provide additional information regarding the atomic structure of the islands. The corrugation atop the Pb/Si(111) α -phase islands has been observed using Scanning Tunneling Microscopy (STM) and high resolution low energy electron diffraction [7,8]. The observed corrugation in STM comes from a combination of an electronic effect related to the confinement of electrons within the Pb island and the geometric pattern related to the relaxation of the layers within the island. [7-9] It is generally accepted that the observed pattern is the Moiré pattern derived from the lattice mismatch of the Pb(1 x 1) lattice and the Si(1 x 1) lattice.

There are two types of corrugation patterns seen on the tops of islands grown on the Pb/Si(111)- $\alpha\sqrt{3}\times\sqrt{3}$ phase. These types have been identified as Type I and Type II. The island types are identified by the contrast of the observed corrugation patterns in STM. The two types of islands come from the two “twin” fcc stacking sequences. However, the stacking sequence of each island type relative to the Si substrate has not been previously identified. The Moiré pattern and observed corrugation of these islands has also been used as a template to grow self organized Ag clusters on top of the Pb islands. [10] The growth of the Ag clusters depends on the island type which the clusters grow on.

Twinning is a common effect in FCC lattices. For a closed packed system there are three equivalent stacking sites, typically named A, B, and C. If one layer is identified as A, the next layer of atoms can go on either the A site or the B site. For FCC crystals there are two possible equivalent stacking sequences i.e., when the first layer is identified as A there is ABCABCA... and ACBACBA.... These sequences are equivalent except for an 180° rotation with respect to each other. Twinning occurs when both sequences are realized within a system.

In many systems, the symmetry of the two twin structures is broken and can lead to differences in the relative population of each stacking sequence. In many overlayers the substrate causes one stacking sequence to be favored over the other. For example, in the Ni/Pt(111) system, there is anisotropy in the populations of each stacking sequence. [11] In Au/Ni(111), the relative ratios of the population can be controlled based on the deposition temperature, and the temperature dependence of the relative population has a complicated

oscillatory behavior. [12] Pb deposited on Ni(111) is very strongly anisotropic, with population ratios as high as 1000:1. [13,14]

Differing populations of stacking sequences in a system do not always depend on temperature. Changes in twinning population with coverage have been observed in Rh/Ru(0001). [15] As coverage is increased from 2ML to 3 ML a reversal in the preferred stacking sequence is observed. Population anisotropies have also been observed for epitaxially grown islands. In the homoepitaxial Ir/Ir(111) small islands preferentially nucleate in the unfavored hcp stacking sequence. As coverage increases the relative amount of islands in the preferred fcc stacking sequence increases. [16,17]

There has been an experimental observation of stacking populations in Pb/Si(111) Measurements have been taken for relative populations of each sequence of Pb/Si(111)-7x7. [18] For 8ML Pb grown at 110 K, the layer by layer growth was found to have nearly equal populations of each stacking sequence using LEED.

Experimental

Experiments took place in a UHV chamber with base pressure 2×10^{-11} Torr. This chamber is equipped with an Omicron variable temperature STM and a conventional LEED system. In each experiment the starting point was the Si(111) 7 x 7 phase. This sample was prepared by flashing the crystal to 1250° C, then cooling the crystal to the temperature of the 7 x 7 reconstruction. The Pb/Si(111)- α phase was created by depositing 1.3 ML onto the clean Si 7x7 at low temperature and annealing for 15 minutes to 500 K. The sample was then cooled to 120 K followed by heating to 160 K for additional Pb. Various coverages ranging from 0.6 ML to 3 ML were added to the Pb/Si(111)- α phase at a flux rate of 0.2 ML/min.

Results

Sample STM images are shown in Figure 1. Figure 1(a) shows a 200 x 140 nm image of a surface with 1 ML deposited on the α phase at T=185 K. Bilayer Pb islands appear as the light portions of the image. In addition to the two types of Pb islands on the image, there are Si islands, which are the solid orange islands in the image, and lead nanoclusters [19],

which are the dark orange spotted regions between the islands. The nearly black section which covers the rest of the image is the wetting layer. The Si $[\bar{1}\bar{1}2]$ direction is identified

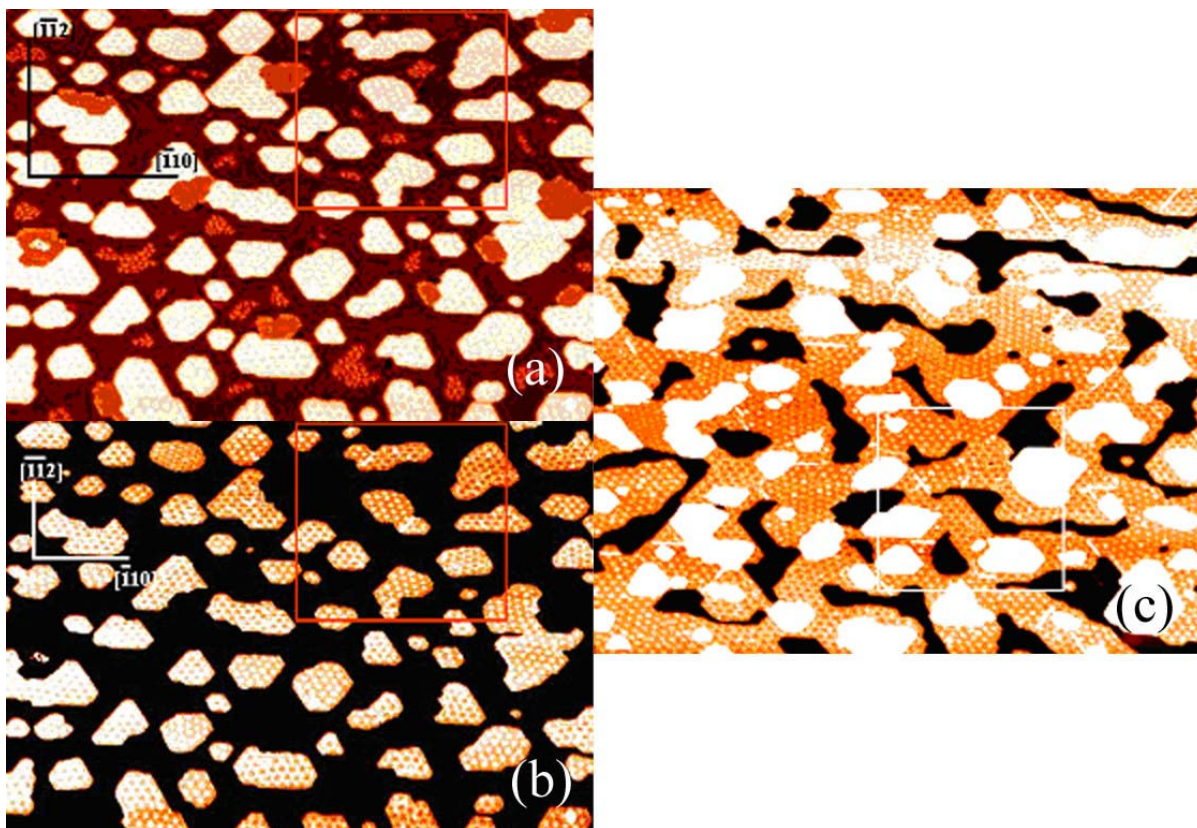


Figure 1: (a) 2000 Å x 1400 Å image taken after $\theta=1$ ML deposition on the α -phase at $T=185$ K. (b) Same image as (a) with contrast enhanced to distinguish between Type I and Type II islands. (c) 2000 Å x 1700 Å image taken after $\theta=2$ ML deposition on the α -phase at $T=185$ K.

using the faulted and unfaulted triangles from the Si 7×7 pattern on the clean sample. Figure 1(b) shows the same image with the contrast enhanced to distinguish easily between Type I and Type II islands. Type I islands can be identified as islands which appear to have dark “holes” on a light background. Type II islands appear to have light “holes” on a dark background. Figure 1(c) shows a 200 x 152 nm image of a surface with an additional 1 ML deposited on the surface in Figure 1(a), also at $T=185$ K. The additional deposition means a total of 2 ML was deposited on the α phase. At this coverage the islands have expanded and form a nearly complete lead bilayer on the surface. In addition, new islands which grow into

the third and fourth layer begin to nucleate on this bilayer. These taller islands appear as the white regions on the image.

In addition to the different corrugation pattern present on the surface of the Type I and Type II islands, there are a number of different features which distinguish the two types of islands. For fcc(111) crystals the edges of the island alternate between (100) microfaceted planes, commonly referred to as A-steps, and (111) microfaceted planes, commonly called B-steps. Small islands of each type, some of which are shown in Figure 1, tend to form shapes which appear more triangular than hexagonal. The orientation of each triangle is strongly dependent on the type of each island. Type I islands tend to have the vertex of the triangle pointed along the $[\bar{1}\bar{1}2]$, and Type II islands tend to have the vertices of the triangles pointed along the opposite or $[\bar{1}\bar{1}2]$ direction. This means that for each island, one type of step edge is typically longer than the other type. For bulk Pb the B-steps should be longer than the A-steps due to the anisotropy in step free energy. [20,21]

Figure 2 focuses on a feature which is seen when the two layer islands grow together. There exists a bright line which is seen that always separates two islands of differing types. We label these as decoration rows because of their similarity to bright lines separating two islands of different stacking seen in Ir/Ir(111). An STM image showing a decoration row is shown in Figure 2(a). This 67.2 nm x 67.2 nm image is taken from the highlighted area in Figure 1(a). A 1-D line profile is shown along the direction indicated by the blue arrow in Figure 2(b). The 1-D line profile clearly shows an increase of height across the decoration row. These decoration rows appear as bright lines which are 3-10 Å wide and extend 1.6-2.2 Å into the fourth Pb layer relative to the silicon. These rows have three different orientations along the three equivalent $[1\bar{1}0]$ directions. For all observed cases, the two types of islands are always on the same side of the decoration rows for each orientation. Along any of the three equivalent $[1\bar{1}0]$ directions, Type I or “dark” islands will be on the left side of the decoration row and Type II or “bright” islands will be on the right side. This means that when two island types come together there is only one type of boundary which will produce these rows.

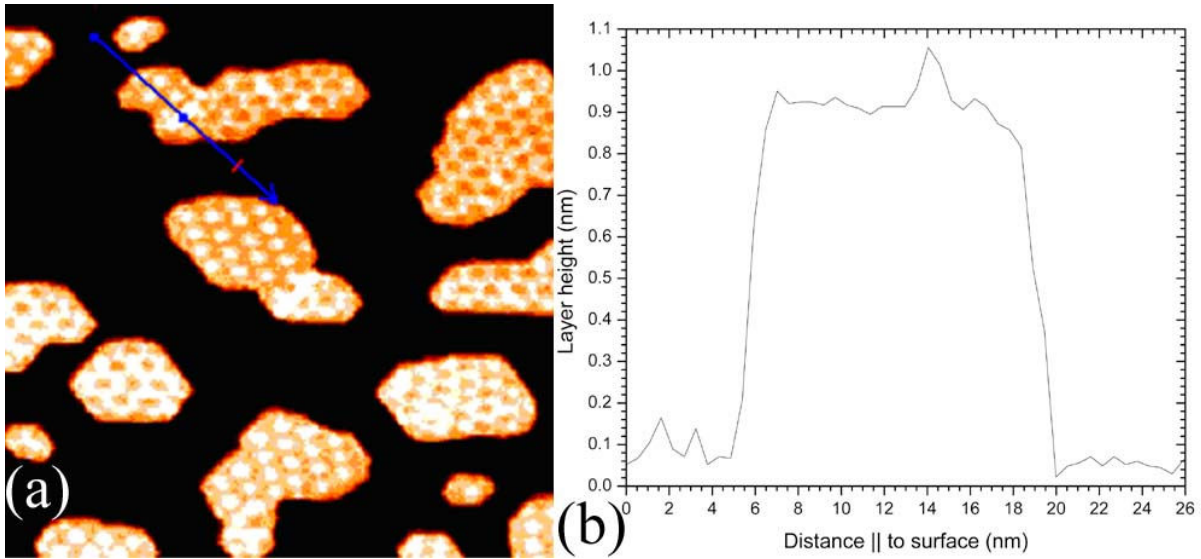


Figure 2: Decoration row between two islands of different types. (a) 67 nm x 67 nm image taken from the highlighted portion of Figure 1(a). (b) The blue line on the two-dimensional scan corresponds to the direction of the one-dimensional scan. The bright decoration row can be clearly seen to extend above the island top.

Using the STM images island number and area was counted for each island type. For coverage $\theta=1$ ML + α phase, as in Figure 1, there are 41 type I islands and 25 type II islands. The ratio of Type I island area to Type II island area is 1.9:1. Island areas were computed using pixel counting features of the software program. Islands were identified as type I or type II and the pixel coverage of each island was counted. As the coverage increases, the islands begin to coalesce and form a nearly complete lead bilayer. This means that we can no longer count individual islands by type; however island area can still be calculated. At this coverage, additional third and fourth layer islands then grow on top of the bilayer. Although the individual islands merge, the island types can still be identified by their contrast. The contrast reverses for each type of island with each additional layer. As the coverage increases and the islands merge, the percentage and coverage of the type II islands increases. At $\theta=2.0$ ML + α phase, the ratio of areas of Type I to Type II islands is 1:1.8, and at $\theta=2.2$ ML + α phase, the ratio of areas is 1:2.2.

Discussion

In the results section we identified the A-steps and B-steps for each type of island based on a comparison between with equilibrium Pb(111) crystals. In doing so we also defined the stacking sequence for each crystal type relative to the silicon substrate. From x-ray diffraction data it is believed that the α phase is destroyed with the formation of Pb islands, leaving bulk Pb crystals. [22,23] Bulk Si forms in the diamond structure, which is an fcc structure with a non-primitive basis. Due to the lattice mismatch between Pb and Si, first layer Pb atoms do not absorb in a unique Si site.

There are four potential types of boundaries when two islands come together. I will label them as follows. When two A-step edges face each other this will be called an A gap. When two B-step edges come in contact this is referred to as a B gap. When an A gap and a B gap come together this will be called an AB-gap. If we assume that the Pb crystals form only FCC stacking sequences the AB-gap is not important. The reason for this is that the only possibility for an AB-gap in these models is to have two islands of the same stacking type merge, and two of the same stacking sequence islands should coalesce without a domain boundary. This can be seen by comparing any two opposite sides in the model and noticing that they have the opposite identification.

Decoration rows with unique configurations were previously observed by Busse and Michely in the Ir/Ir(111) system. [17] They show that the decoration rows in that system were only formed between A-gaps. These decoration rows occur because atoms become trapped in the four-fold coordination sites which are created from the two island sides in the A-gap. From a bond counting argument these positions were argued to be more stable than positions on the island top or in the B-gap, where there are only three-fold coordination sites. Using this model, a self-healing mechanism was also proposed, which showed how the less stable B-gaps would be transformed into more stable A-gaps, and how the less stable “hcp” stacking sequence islands were converted into more stable “fcc” stacking sequence islands.

The shapes of the islands and the known step energies indicate that the bright decoration rows are B-gap boundaries between two islands. However, this contradicts previous results for single step islands in Ir/Ir(111). To show that the decoration rows should

be formed in the B-gap but not the A-gap, we construct atomic models which show that the addition of a second layer to the islands cause a shift in the geometry the A-gap and the B-gap. The second layer introduces stable four-fold coordination sites in the B-gap which can explain why decoration rows may be formed in the B-gap. This new model can explain all of the experimental observations, which include the ratios of the step edges and the single type of observed island boundaries.

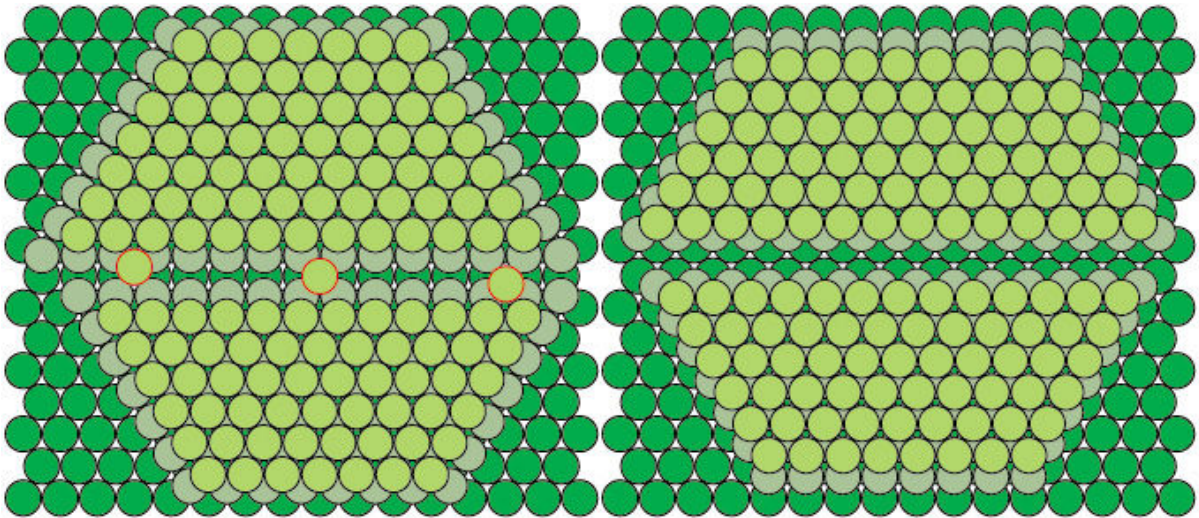


Figure 3: (Left) A-gap. Three atoms are located at different 4-fold coordination sites within the gap. These are possible locations for decoration rows. (Right) B-gap. There are no four fold sites within this gap, meaning that there are no energetically favorable sites for single atoms to be trapped.

Figure 3 shows hard ball atomic models of the A-gap and the B-gap, this time showing the two-layer islands which are present in our system as opposed to the single layer islands which are seen by Busse and Michely. [17] The introduction of two-layer islands introduces new geometries which are not seen in the Ir/Ir(111) model. For both the A-gap and the B-gap, the distance between islands in the second layer is less than one lattice constant, which means that there is no way to fit an atom between the islands in the second layer. In the third layer, for both gaps the distance is more than one lattice constant, so atoms may settle in the third layer. For the A-gap, there are three sites which are equidistant from four nearest neighbor atoms. These sites are outlined in red in figure 3. The right and left atoms are in the third layer stacking site for the island on each side of the gap. The

middle atom is located at the midpoint of two atoms from each side of the gap. This is the same as the decoration row four-fold site in the Ir/Ir(111) model. However for all three positions the extra atom would be located slightly lower than the third layer of atoms the island its “support” atoms are more than one lattice constant apart, and therefore it is unlikely that atoms in the A-gap cause the decoration row which extends into the fourth Pb layer.

The bright lines in Ir were explained as atoms which get trapped in fourfold coordination sites on the top layer of Ir. In the B-gaps these four-fold sites are not present so no decoration row can grow in these gaps. However, if we add an extra row of atoms in the three-fold sites on one side of the island (this is equivalent to adding an extra row of third layer atoms to one island) we can create four-fold sites similar to the sites seen in Ir on the third Pb layer. These sites can be used to nucleate a decoration row into the fourth Pb layer, which would explain the observed bright decoration row lines. A model for this decoration row is seen in Figure 4. Figure 4 shows the same top view as the B-gap model in figure 3, but has this extra row of third layer atoms on the bottom island as well as a new row of atoms in the created four-fold sites. In the cross section of the B-gaps, which shows the atoms contained in the rectangle on the top view, we see that the decoration row atoms would be lower than atoms on a fourth Pb layer. The B-gap decoration row model is consistent with both the length of the step edges and the unique orientations of the decoration rows.

With the information from the step edges and decoration rows we identify the island stacking sequences relative to the silicon substrate as shown in Figure 5. The silicon substrate can be thought of as an fcc lattice with a non-primitive basis. The Type I islands have an fcc lattice with the opposite stacking sequence as the Si substrate. Using the ABC notation if the Si substrate stacks in the ABCAB... pattern, the Type I islands stack in the ACBAC... Type II islands stack in the same direction as the Si substrate. If Si is ABCABC, then the Type II islands also stack in this sequence. The inset for each type of island in Figure 5 identifies the A-step and B-step orientations for each island type. The A-steps and B-steps are located on opposite sides of the islands for each island type. B-steps are drawn longer to correspond with the bulk step energies. Since B-steps are longer than A-steps Type

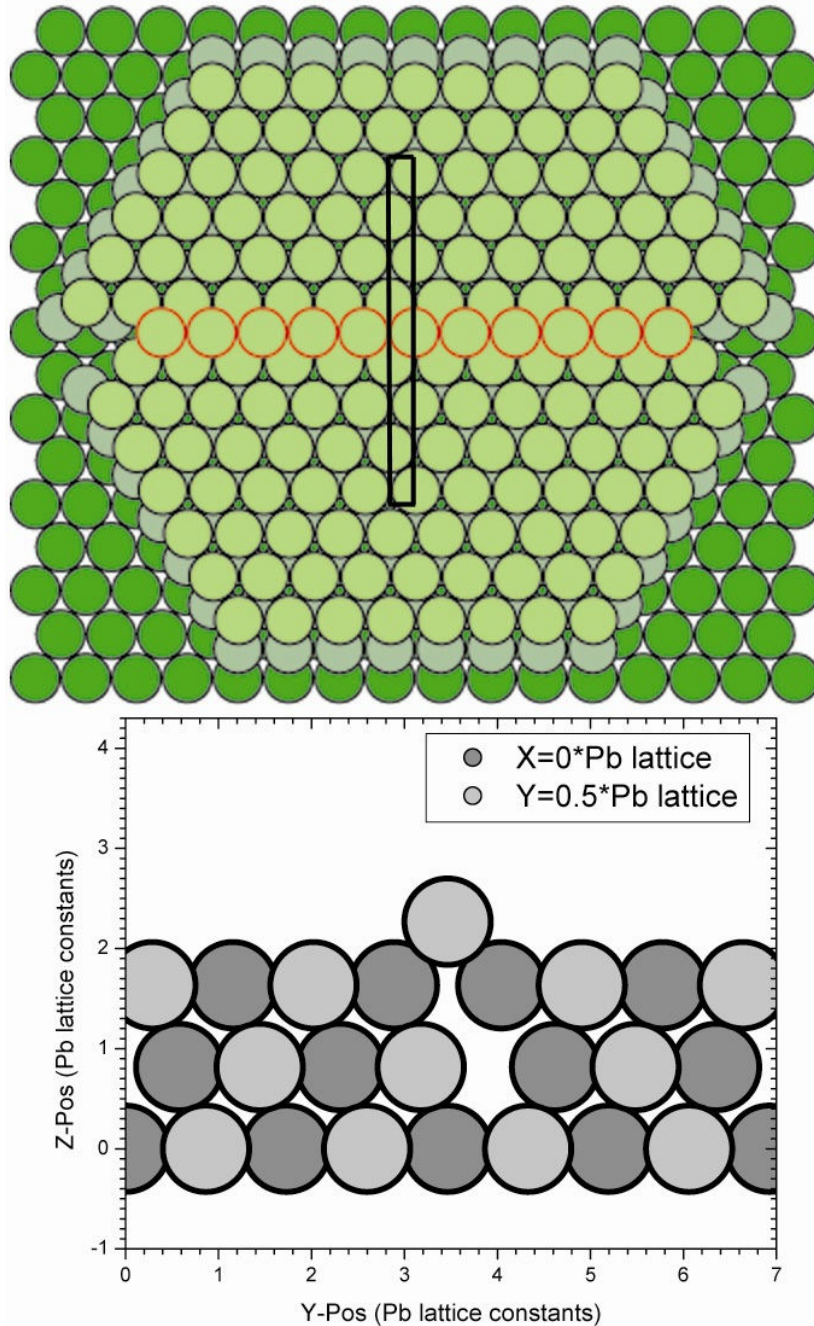


Figure 4: Proposed model for B-gap decoration row. (Top) view from above islands. (Bottom) cross section along $[112]$ direction showing a possible atomic configuration of the decoration row.

I triangular islands will point along the $[\bar{1}\bar{1}2]$ direction and Type II islands will point along the $[\bar{1}\bar{1}\bar{2}]$ direction, consistent with the experimental results.

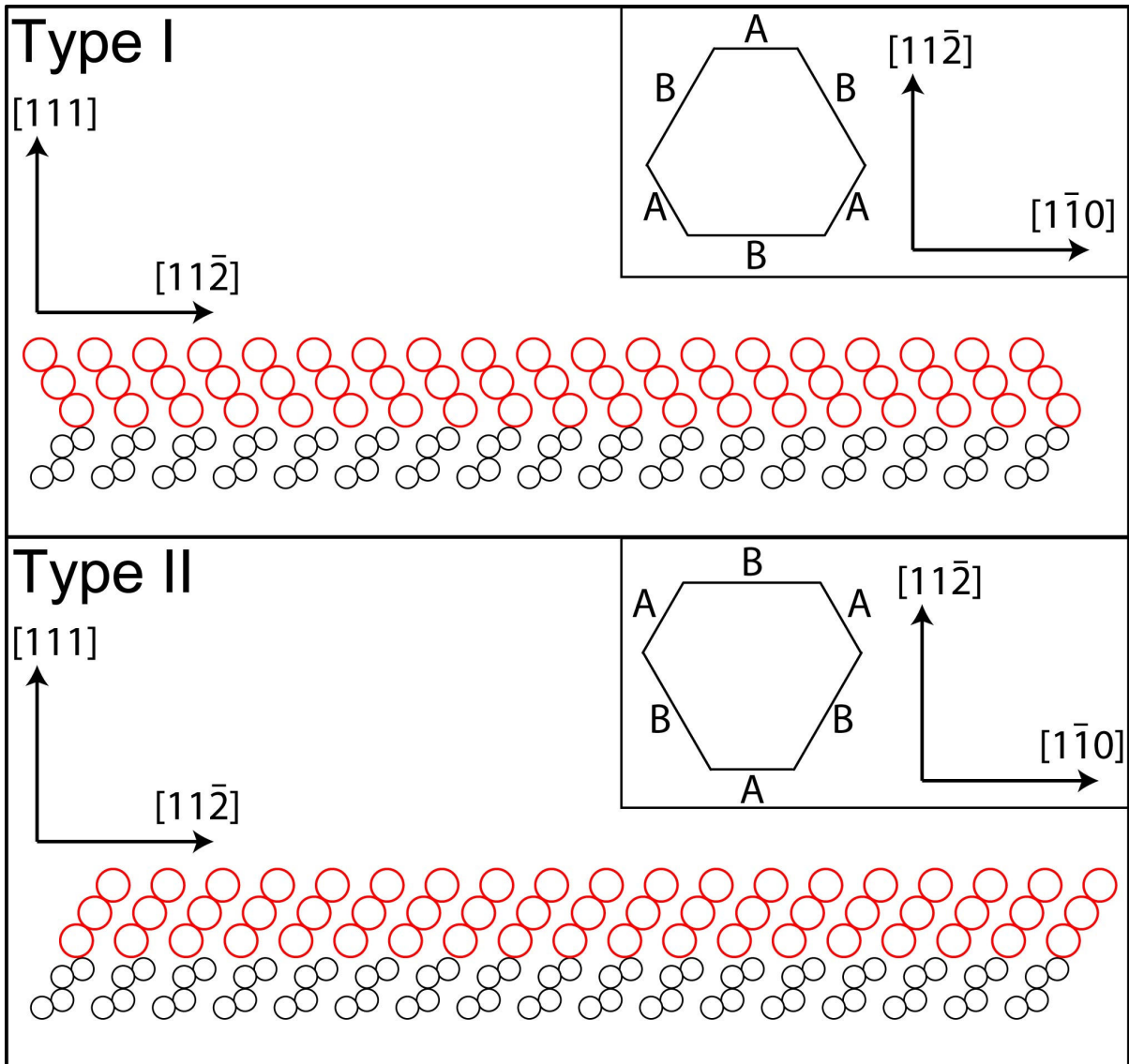


Figure 5: Proposed stacking sequences for Type I and Type II Pb islands. For each type an unrelaxed hard ball model is included, as well as the identification of the step edges for each island type (inset).

The exact mechanism which drives the conversion from one stacking sequence to the other is unclear. For the twin FCC stacking sequences, there is no difference between the islands of each stacking type. This symmetry can be broken if we include the Si(111) substrate underneath the first Pb layer, since the twins are now rotated 180° with respect to

the substrate. A proposed mechanism for the changing twin population would need to use the Si substrate to break the symmetry between the two island types. Different twin populations were not observed for Pb islands grown on Si(111)-7x7 at 110 K. [18] Therefore the α -phase interface, the surface morphology or the temperature could all contribute to the effect.

In single layer islands of Ir/Ir(111) hard ball models were used to show a kinetic process by which islands of the energetically unfavorable sequence are converted into the energetically more favorable sequence. [17] However, the extra geometric complications of the bilayer islands and the Si substrate require advanced energy calculations in order to reproduce these mechanisms. In Rh/Ru(0001) first principles calculations are used to show that single layers of Rh prefer one stacking sequence, while trilayers prefer the opposite sequence. [15] The shift in stacking sequence is mediated by the nearly degenerate energy of the two stacking sequences for double layers. Perhaps similar calculations might illuminate the mechanism for the island conversion in Pb/Si(111).

Conclusions

Pb islands grown on the Si(111)- α phase display two corrugation patterns which are caused by the twin fcc stacking sequences. The fcc sequence for each type relative to the Si substrate has been identified from the relative lengths of the step edges and from the observation of decoration rows which form at boundaries between islands of different types. In addition, the relative population of each island type is shown to change with increasing coverage as the island stacking changes from stacking opposite of the Si stacking direction to stacking in the same direction as the Si.

References

- [1] K. Budde, E. Abram, V. Yeh, M.C. Tringides, *Phys. Rev. B* **61**, R10602 (2000)
- [2] V. Yeh, L. Berbil-Bautista, C.Z. Wang, K.M. Ho, M.C. Tringides, *Phys. Rev. Lett.* **85**, 5158 (2000)
- [3] M. Hupalo, V. Yeh, L. Berbil-Bautista, S. Kremmer, E. Abram, M.C. Tringides, *Phys. Rev. B* **64**, 155307 (2001)

- [4] M. Hupalo, S. Kremmer, V. Yeh, L. Berbil-Bautista, E. Abram, M.C. Tringides, *Surf. Sci.* **493**, 526 (2001)
- [5] C.M. Wei and M.Y. Chou, *Phys. Rev. B* **66**, 233406 (2002)
- [6] E. Ogando, N. Zabala, E.V. Chulkov, M.J. Puska, *Phys. Rev. B* **69**, 153410 (2004)
- [7] W.B. Jian, W.B. Su, C.S. Chang and T.T. Tsong, *Phys. Rev. Lett.* **90**, 196603 (2003)
- [8] M. Hupalo, V. Yeh, T.L. Chan, C.Z. Wang, K.M. Ho and M.C. Tringides, *Phys. Rev. B* **71**, 193408 (2005)
- [9] T.L. Chan, C.Z. Wang, M. Hupalo, M.C. Tringides, W.C. Lu, K.M. Ho (submitted)
- [10] H.Y. Lin, Y.P. Chiu, L.W. Huang, Y.W. Chen, T.Y. Fu, C.S. Chang, T.T. Tsong, *Phys. Rev. Lett.* **94**, 136101 (2005)
- [11] O. Robach, H. Isern, P. Steadman, K.F. Peters, C. Quiros, and S. Ferrer, *Phys. Rev. B* **68**, 214416 (2003)
- [12] K. Umezawa, S. Nakanishi, W.M. Gibson, *Phys. Rev. B* **57**, 8842 (1998)
- [13] A. Krupski and S. Mroz, *Phys. Rev. B* **66**, 035410 (2002)
- [14] A. Krupski, M. Nowicki, *Surf. Sci.* **575**, 147 (2005)
- [15] Y. He, A.P. Seitsonen, H. Over, *Phys. Rev. B* **72**, 075432 (2005)
- [16] C. Busse, C. Polop, M. Mueller, K. Albe, U. Linke, and T. Michely, *Phys. Rev. Lett.* **91**, 056103 (2003)
- [17] C. Busse, T. Michely, *Surf. Sci.* **552**, 281 (2004)
- [18] A. Mans, J.H. Dil, A.R.H.F. Ettema, H.H. Weitering, *Phys. Rev. B* **72**, 155442 (2005)
- [19] M. Hupalo and M.C. Tringides, *Phys. Rev. B* **65**, 205406 (2002)
- [20] P. Feibelman, *Phys. Rev. B* **62**, 17020 (2000)
- [21] M. Nowicki, C. Bombis, A. Edmundts, H.P. Bonzel, *Phys. Rev. B* **67**, 075405 (2000)
- [22] P.B. Howes, K.A. Edwards, D.J. Hughes, J.E. Macdonald, T. Hibma, T. Bootsma, M.A. James, *Phys. Rev. B* **51**, 17740 (1995)
- [23] K.A. Edwards, P.B. Howes, J.E. Macdonald, T. Hibma, T. Bootsma, M.A. James, *Surf. Sci.* **424**, 169 (1999)

CHAPTER 6: DEPENDENCE OF RELATIVE ROTATION ON COVERAGE OF Pb OVERLAYERS ON Si(111)-Pb($\sqrt{3}\times\sqrt{3}$)- α PHASE

M. Yakes¹, M. Hupalo², M.C. Tringides³

(Based on a paper to be submitted to *Physical Review B*)

Abstract

High resolution spot profile analysis low energy electron diffraction (SPA-LEED) and variable temperature scanning tunneling microscopy (STM) have been used to observe the growth of Pb on the Pb/Si(111)- $\alpha\sqrt{3}\times\sqrt{3}$ phase. A change in the rotation of the Pb overlayer relative to the Si substrate with increasing coverage has been observed for Pb islands grown on the Pb/Si(111) α -phase. For separated 2-step islands the $[1\ \bar{1}\ 0]$ axis of the islands is aligned with the $[1\ \bar{1}\ 0]$ axis of the substrate. At higher Pb coverage the islands coalesce and form a bilayer with additional islands grown on top of the bilayer. As the coverage increases the preferred Pb orientation changes from aligned with the substrate to rotated 5.6° with respect to the substrate.

Introduction

The growth of reproducible self-assembled nanostructures with uniform size and geometry has many potential uses in technological applications such as lasers, switches, and sensors. In order to realize the potential of these structures, it is necessary to develop methods to control their geometry, size, and spatial arrangement. The Pb/Si(111) system has shown an intriguing growth mode which is made up of uniform height islands with flat tops and steep edges. [1] These islands are grown in bilayer increments, and their height can be controlled based on the temperature, coverage, and substrate. [2-4]

The driving force of the unusual growth mode of the Pb/Si(111) islands is believed to be related to the confinement of electrons in the direction of the surface normal. This is usually referred to as the Quantum Size Effect (QSE). First principles calculations on free standing Pb films and mixed models have given more support to this conclusion. [5, 6] The

¹ Graduate Student, primary researcher

² Staff Scientist, conducted STM experiments

³ Professor, author for correspondence

QSE effect depends critically on the boundary conditions at the vacuum/island and the island/substrate interfaces. This means that accurate atomic and electronic models are crucial to a complete understanding of the growth mode.

One experimental observation which has helped in the understanding of the atomic and electronic structure of the Pb islands and the Pb/Si interface is the corrugation of the Pb islands grown on the Pb/Si(111)- $\alpha\sqrt{3}\times\sqrt{3}$ phase. The corrugation atop the Pb/Si(111) islands created atop the α -phase has been observed using Scanning Tunneling Microscopy (STM) and high resolution spot profile analysis low energy electron diffraction (SPA-LEED) [7,8]. The observed corrugation in STM comes from some combination of the geometric pattern related to the relaxation of the layers and an electronic effect related to the confinement of electrons within the island. [9,10] The relative contribution of each effect is still the subject of some debate. [7,11] Regardless of which effect is the primary cause for the observed corrugation, it is generally accepted that the observed pattern is the Moiré pattern derived from the lattice mismatch of the Pb(1 x 1) lattice and the Si(1 x 1) lattice. The Moiré pattern and observed corrugation of these islands has also been used as a template to grow self organized Ag clusters on top of the Pb islands. [12]

In previous experiments with SPA-LEED, the orientation of the Pb lattice relative to the Si(111) has been observed as well as a change in the size and direction of the Moiré pattern in STM [7,8]. In STM experiments, it is difficult to obtain reliable statistics on the orientation of the Pb lattice and the size and direction of the Moiré pattern. With the ability to illuminate and probe macroscopic distances (~ 0.5 mm) diffraction is an ideal method for obtaining this structural aspect if the features of the diffraction pattern can be properly identified.

A rotation of the Pb lattice relative to the Si substrate has been observed for islands grown in Stranski-Kratonov growth mode at room temperature and coverage $\theta > 3$ ML. [13] The observed rotation was 6° for Pb overlayers on Si(111)- 7×7 and 3° for overlayers on Pb- $\sqrt{3}\times\sqrt{3}$ - α phase. In Ref. 13 the dense ($\theta > 1$ ML) Si(111)-Pb $\sqrt{3}\times\sqrt{3}$ is referred to as the β phase, however, in recent literature the convention is to refer to it as the α phase. For QSE islands grown on Pb- $\sqrt{3}\times\sqrt{3}$ - α phase, a rotation of 5.6° has been observed. [14] For the

Si(111)- 7×7 phase, this rotation was explained by the geometric coincidence of a rigid Pb lattice and the underlying substrate. This coincidence lattice was found geometrically by comparing lengths of a vector constructed from integer multiples of the substrate unit cell vectors with the bulk Pb lattice constant. If the length of the multiple substrate vector matched some multiple of the Pb lattice constant to within 3%, it was deemed a coincidence lattice and a possible candidate for the Pb rotation vector. Comparing with the experimental results yielded a match to the Si(111)- 7×7 phase. However, the 3° overlayer rotation of the Pb- $\sqrt{3}\times\sqrt{3}$ - α phase was not matched. Later x-ray diffraction data indicates that Pb deposited on the $\sqrt{3}\times\sqrt{3}$ phase destroys the $\sqrt{3}\times\sqrt{3}$ phase and leaves an unreconstructed Si surface. [15,16]

The coincidence of the Pb lattice with the substrate is an example of a coincident site lattice (CSL). CSL's are often seen at grain boundaries in polycrystalline materials. Many heteroepitaxial rotations occur such that a CSL is created between the substrate and the overlayer. The coincident site lattice is derived from two lattices one which is fixed and one which is rotated. For a given angle, periodically one lattice point of the rotated lattice is located close to a lattice point of the second lattice. These points of closest approach form a new lattice on the surface. For heteroepitaxial systems where the two lattices do not have the same lattice constant in general one lattice must be strained by a small amount to achieve perfect coincidence. Since these coincidence points are assumed to have lower strain energy than points far from coincidence for small CSL cell sizes the overall strain energy of the interface is reduced. While for any two given lattices there are an infinite number of possible CSL's, the observed lattice should have a small CSL distance and a small strain. Since CSL theory is a geometric theory and cannot account for atomic relaxations or interatomic potentials, it is not a universal theory and does not account for all overlayer rotations, as seen in the mixed success of describing Pb/Si overlayers grown at room temperature. [17-19]

The rotation of the overlayer lattice relative to the substrate is a common effect in heteroepitaxial systems. Overlayer rotations often appear in systems with large lattice mismatches between the overlayer and the substrate. For example, overlayer rotations are seen in systems with rare gases physisorbed on graphite [20], metal on metal systems

[21,22], and metal-oxides on metal. [23] In these examples rotations occur for both monolayer and multilayer surface coverages. However, in contrast to the case of Pb island growth which occurs at $T \sim 200$ K, all of these example cases are in systems with temperatures greater than 500 K.

Complete overlayers are not required to see rotation. For Ag islands annealed to 210° C on H-terminated Si(111) it was observed that the rotation of the Ag lattice changed depending on the size of island. [24,25] In this case the equilibrium orientation depended on the size and the shape of the island. As the coverage, size and shape of the island changes the rotation angle which gave the lowest interface energy also varied. As the Ag island size increased the islands became better aligned with the coincident-site-lattice energy minimum.

In this paper we identify the origin of the unusual diffraction patterns seen for Pb growth on the Pb/Si(111) α -phase, and discuss the patterns evolution with Pb coverage and film morphology. From these observations, it appears that preferred island orientation changes as the coverage increases and that the island morphology changes from 2-step islands to 2-step islands with higher islands grown on top.

Experiment

Experiments took place in two separate UHV chambers with base pressure 2×10^{-11} Torr. One chamber is equipped with an Omicron SPA-LEED system, Auger spectrometer and mass spectrometer. The other chamber was equipped with an Omicron variable temperature STM and a conventional LEED system. In each experiment the starting point was the Si(111) 7×7 phase. This sample was prepared by flashing the crystal to 1250° C, then cooling the crystal to the temperature of the 7×7 reconstruction. The Pb/Si(111)- α phase was created by depositing 1.3 ML onto the clean Si 7×7 at low temperature and annealing for 15 minutes to 500 K. The sample was then cooled to 120 K followed by heating to 160-200 K for additional Pb deposition for the SPA-LEED and STM experiments. Various coverages ranging from 0.6 ML to 3 ML were added to the Pb/Si(111)- α phase at a flux rate of 0.2 ML/min.

Results

Figures 1 and 2 show three diffraction scans near the (00) spots which show frequently observed diffraction patterns, and three corresponding scans of a Pb (10) spot. Each scan covers 40% of the silicon Brillouin Zone (BZ), and the surface was prepared in a similar fashion to the surfaces in the STM experiments. Figures 1(a) and 1(b) were taken from a surface with 0.6 ML above the Pb/Si(111)- α phase. It has coverage 1.9 ML total. There are six spots located 15% BZ from the (00) spot along the $[1\bar{1}0]$ direction. The 15% BZ value in reciprocal space corresponds to a real space value of 26 Angstroms. It is known at this coverage and deposition temperature that Pb nanoclusters form. [26] These clusters have triangular units of size 2.7 nm. The spots are broad with a width of $6 \pm 1\%$ along the $[1\bar{1}0]$ direction indicating an average domain size of $65 \pm 10 \text{ \AA}$. These clusters are formed on the Pb/Si(111)- α phase before island growth, so it is consistent that these spots identify the presence of the clusters.

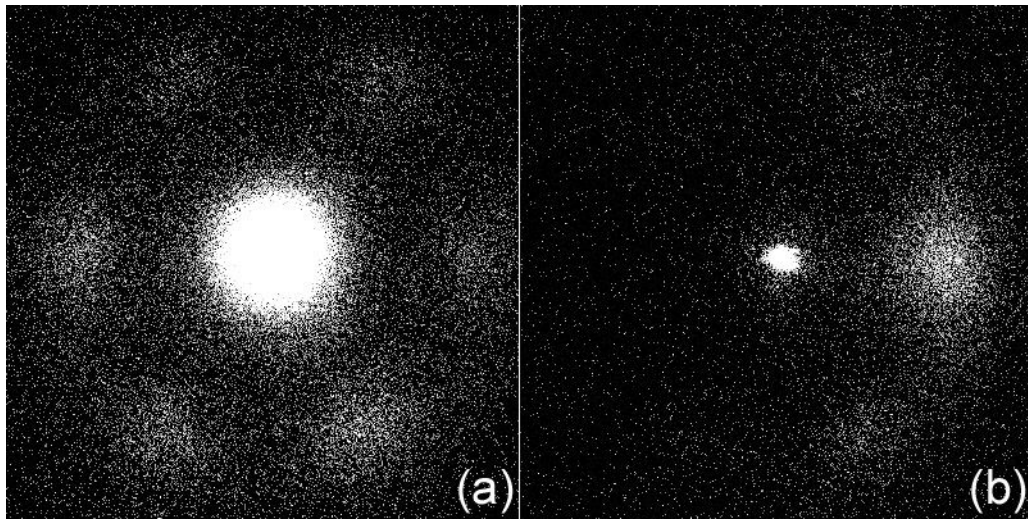


Figure 1: 0.6 ML deposited on the α -phase at 195 K. 2-D 40% x 40% BZ scans (a) centered on (00) beam showing Pb cluster spots. (b) Same experimental conditions as 1(a) centered on Si (10) beam showing no Pb rotation at this coverage.

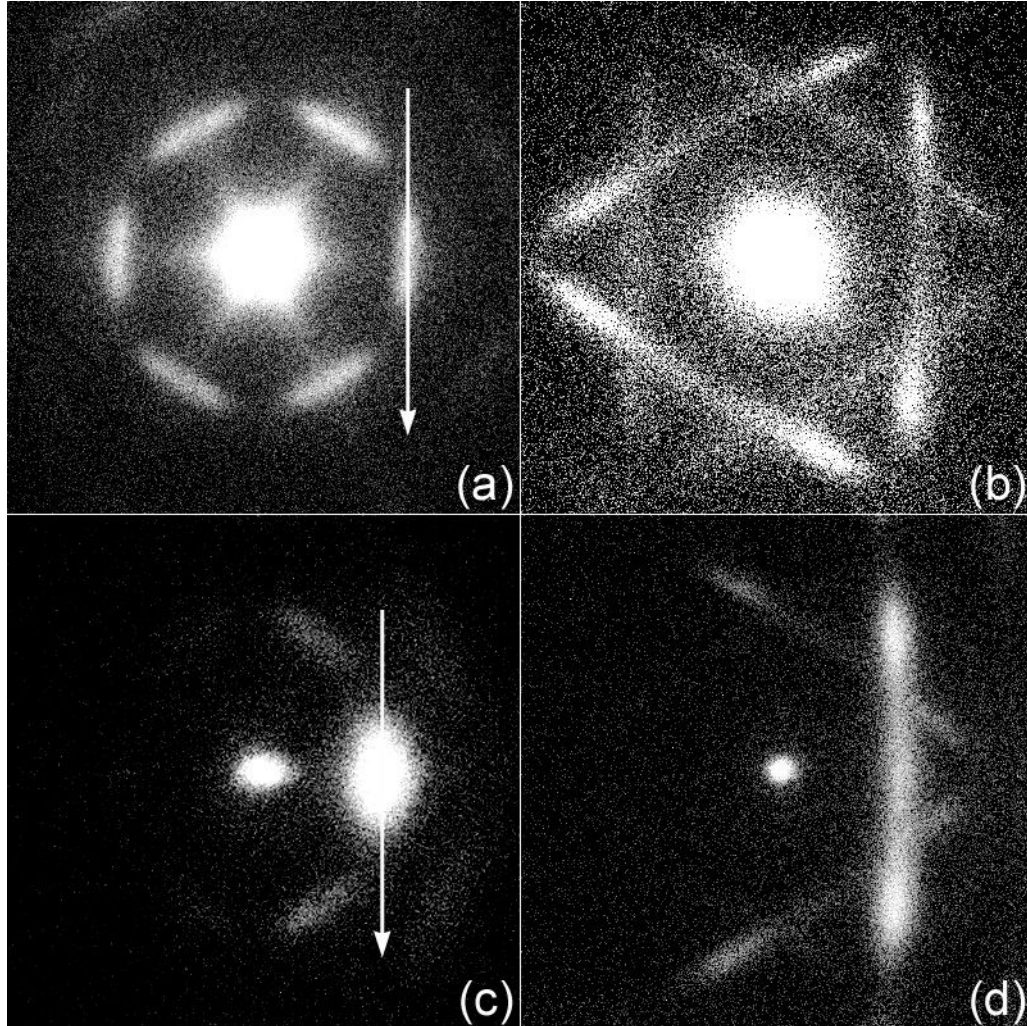


Figure 2: (a)-(c) 1.1 ML deposited on the α -phase at 195 K. (a) centered on (00) beam showing hexagonal corrugation spots. (c) Same experimental conditions as (a) centered on Si (10) beam showing Pb rotation spots. The white arrows indicate the direction of the corrugation (a) and Pb spot (c) 1-D scans seen in figures 5 and 9. (b)-(d) 1.7 ML deposited on the α -phase at 180 K. (b) Centered on (00) beam showing star corrugation spots. (d) Same experimental conditions as (b) centered on Si (10) beam showing Pb rotation spots.

As more Pb is added to the surface with nanoclusters, two step islands begin to form on the surface. Figure 2(a) and 2(c) were taken for a surface with 1.3 ML above the Pb/Si(111)- α phase. It has coverage 2.6 ML total. There are six spots located 11% BZ from the (00) spot along the $[1\bar{1}0]$ direction. These spots can be distinguished from spots originating from Pb nanoclusters using the wavevector of the spots. The nanocluster spots appear at 15% BZ along the $[1\bar{1}0]$ direction instead on these observed spots at 11%. This

11% spot position corresponds to a real space distance of 34.9 Angstroms. We refer to these six spots as the “hexagon” pattern, from the hexagonal shape formed by the six spots near (00). These spots are elongated along the $[\bar{1}\bar{1}2]$ direction with the maximum intensity along the $[1\bar{1}0]$ axis.

Figure 2(b) shows a “star” pattern. Figures 2(b) and 2(d) were taken from a surface with coverage 1.8 ML on top of the alpha phase. The diffraction pattern in Figure 2(b) looks similar to the pattern in figure 2(a) as the “hexagon” spots are still located 11.0% BZ away from the (00) spot along the $[1\bar{1}0]$ axis, in the same position as the spots from the lower coverage scan. However, the hexagon spots now appear to be extended along the $[\bar{1}\bar{1}2]$ direction to form the six point star pattern. Instead of a continuous distribution of intensity along the $[\bar{1}\bar{1}2]$ direction, the intensity now has three lobes, one at the same position as the hexagon intensity, and two new lobes near the points of the star.

STM images verify the island morphologies at coverages corresponding to the hexagon and star patterns. Two STM images at representative coverages are shown in Figure 3. Figure 3(a) shows 1.0 ML of Pb deposited on the α phase at 160 K. The STM image covers an area 80 nm x 80 nm. At this coverage the hexagon pattern appears in the diffraction images. The surface is primarily covered with two step islands. There are also small Si islands (seen as smooth dark orange patches) and small patches of Pb nanoclusters (seen as textured dark orange patches). There are two insets which have the contrast enhanced to show the corrugation patterns. There are two types of corrugation patterns on the surface which can be identified by the relative contrast of the holes in the Moiré pattern, as has been discussed elsewhere. [7] The corrugation lengths are measured as 3.5 nm and 3.6 nm, for the left and right inset, respectively. The orientation of the corrugation is measured as 4.5 degrees away from the $[1\bar{1}0]$ direction for the left inset and 5.4 degrees away from the $[1\bar{1}0]$ for the right inset.

Figure 3(b) shows a 50 nm x 50 nm image with 1.5 ML of Pb deposited on the $\sqrt{3}\times\sqrt{3}$ phase at 180 K. At this coverage the star pattern appears in the diffraction images. The islands have grown together and now cover the surface large “continents”. On top of the second layer larger islands are being grown. Corrugation patterns can be seen both on the

second layer island as well as the larger islands. As in Figure 3(a), portions of the second layer have enhanced contrast to more clearly show the corrugation. In this case the corrugation pattern shows clear changes in length and orientation between the patches. The corrugation lengths are measured as 2.9 nm for the left inset, 2.5 nm for the upper right inset and 3.5 nm for the lower right inset. The rotation angles away from the $[1\bar{1}0]$ direction are 24.0 degrees for the left inset, 3.6 degrees for the upper right inset and 0.5 degrees for the lower right inset.

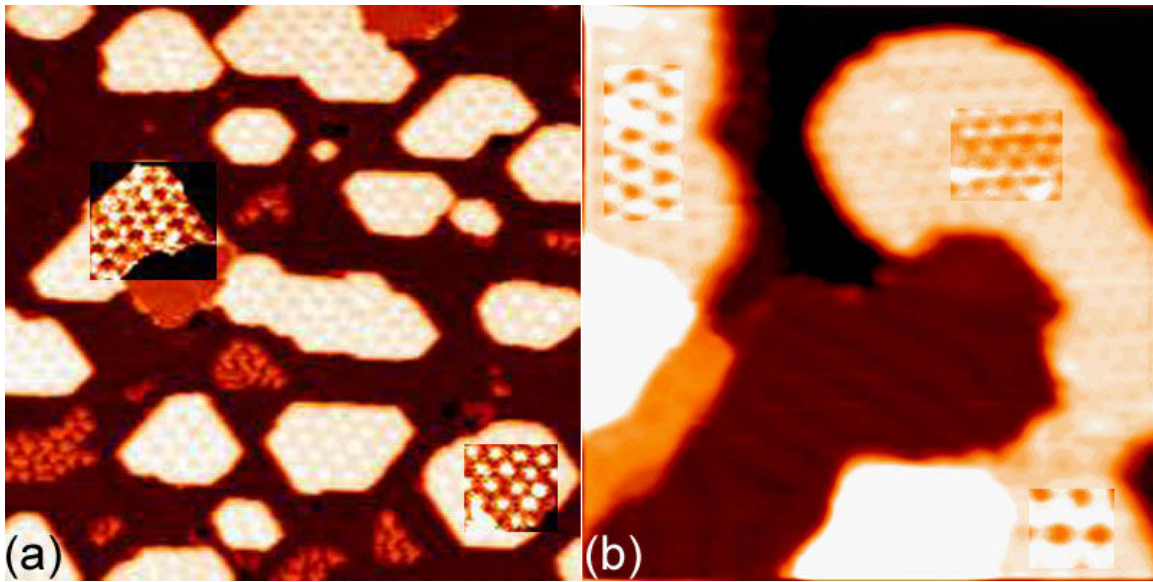


Figure 3: STM images showing surface morphologies at different Pb coverage. (a) 80 nm x 80 nm scan at 1.0 ML coverage deposited at 160 K. The island corrugation is visible on the two step islands, and there is a small coverage of Pb nanoclusters between the islands. (b) 50 nm x 50 nm scan at 1.5 ML coverage deposited at 185 K. The 2-step islands have grown together to form continents. Higher islands have grown on top of the nearly complete bilayer. In each image the contrast in the second layer has been enhanced in the inset sections to show the corrugation pattern more clearly.

In diffraction the surface morphology can be investigated using $g(s)$ curves. The $g(s)$ curve is derived from the intensity ratio of the sharp and broad components of the (00) peak as a function of normalized momentum transfer ($s=K_n/(2\pi/d)$, where K_n is the normal component of the momentum transfer). This ratio oscillates as the momentum transfer changes from in-phase to out-of-phase conditions. The period of the oscillations of the $g(s)$ curve is inversely proportional to the island height. [1,4]

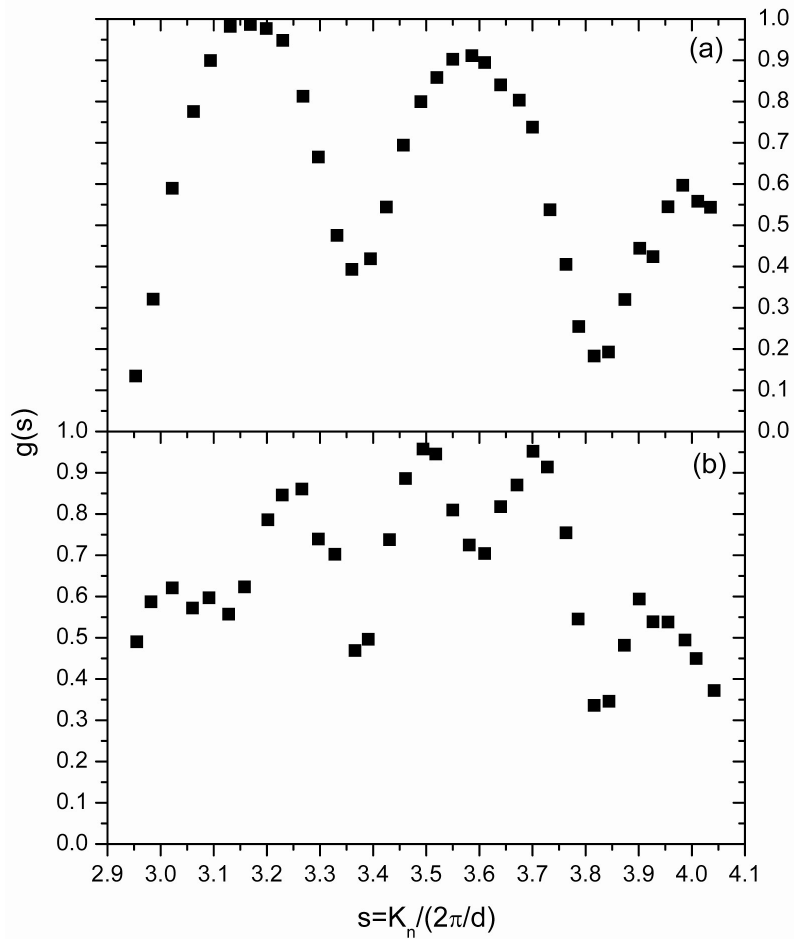


Figure 4: $G(s)$ curve showing 2-step intensity oscillations for Pb islands. (a) Surface prepared by depositing 1.1 ML onto the Pb/Si(111)- $\alpha\sqrt{3}\times\sqrt{3}$ phase at 195 K. The beating period of $1/2$ indicates that the surface is covered primarily with two-layer islands. (b) Surface prepared by depositing 1.7 ML onto the Pb/Si(111)- $\alpha\sqrt{3}\times\sqrt{3}$ phase at 195 K. The higher order periods and reduction in 2-step periods indicate that larger islands are being formed in addition to the two-layer islands.

The $g(s)$ curve for a sample with coverage 1.1 ML is shown in figure 4(a). At this coverage the hexagon diffraction pattern is seen near the (00) spot. The primary oscillation period of $1/2$ is clearly visible from the data, meaning that the surface is predominantly covered with 2-step islands. The observation of 2-step islands is consistent with the observed STM results at this coverage. Figure 4(b) shows the $g(s)$ curve for a surface covered with 1.7 ML of Pb. At this coverage, the star diffraction pattern is seen near the (00) spot. In figure 4(b) the 2-step island oscillation has decreased in intensity as compared to figure 4(a), indicating that 2-step islands are no longer the primary feature on the surface. The $g(s)$ curve

shows lower period oscillations corresponding to higher islands in addition to the 2-step islands. This is consistent with the STM results at this coverage, which show the 2-step islands coalescing into “continents”, with new larger islands growing on top of the larger 2-step islands.

Additional data can be determined using 1-D profiles of the corrugation and Pb spots. Figure 5 shows a series of 1-D scans taken at two coverages, again showing the major features of the 2-D diffraction pattern. 1-D scans provide more detail about the distribution of intensity along the sides of the hexagon and star, as well as the Pb spots. Each scan was taken along the $[\bar{1}\bar{1}2]$ direction centered at the maximum spot intensity along the $[1\bar{1}0]$ direction. These directions are shown by the white arrows in Figures 2(a) and 2(c). Figures 5(a) and (b) are taken from a surface with 1.2 ML on top of the alpha phase, where the hexagon pattern is seen in the 2-D pattern and Figures 5(c) and (d) come from a surface with 1.9 ML on the alpha phase, where the star pattern is seen in the 2-D pattern. Figures 5(a) and 5(c) show the measurement in %BZ of silicon along the $[\bar{1}\bar{1}2]$ direction away from the maximum corrugation intensity along the $[1\bar{1}0]$ direction for the hexagon and star pattern respectively. For the corrugation spots, we would like to convert this distance into an angle of corrugation. To do this the conversion is $\tan \phi = x/11.0$, where x is the %BZ distance along the $[\bar{1}\bar{1}2]$ direction away from the maximum of the “hexagon” spot. The reasons for converting the Brillouin Zone measurement to an angle will become clear in the later discussion.

Figures 5(b) and 5(d) (again corresponding to the hexagon and star patterns) show a cross section of the Pb (10) spot taken along the $[\bar{1}\bar{1}2]$ direction at the maximum spot intensity along the $[1\bar{1}0]$ direction, located 111.6 ± 0.8 % BZ away from the (00) spot position. 111.6 ± 0.8 % BZ corresponds to 3.44 ± 0.02 Å real space distance, indicating that the Pb lattice is compressed in the (111) plane. To convert this measurement in % BZ to the angle of rotation of the Pb lattice, we use the conversion $\tan \theta = x/111.6$, where x is the distance in % BZ along the $[\bar{1}\bar{1}2]$ direction away from the maximum of the Pb (10) spot. Unlike the spots closer to the (00) spot, which will be shown in the discussion section to

measure the size and orientation of the island corrugation, the Pb(10) spot can be used to directly measure the relative orientation of the Pb lattice with respect to the Si lattice.

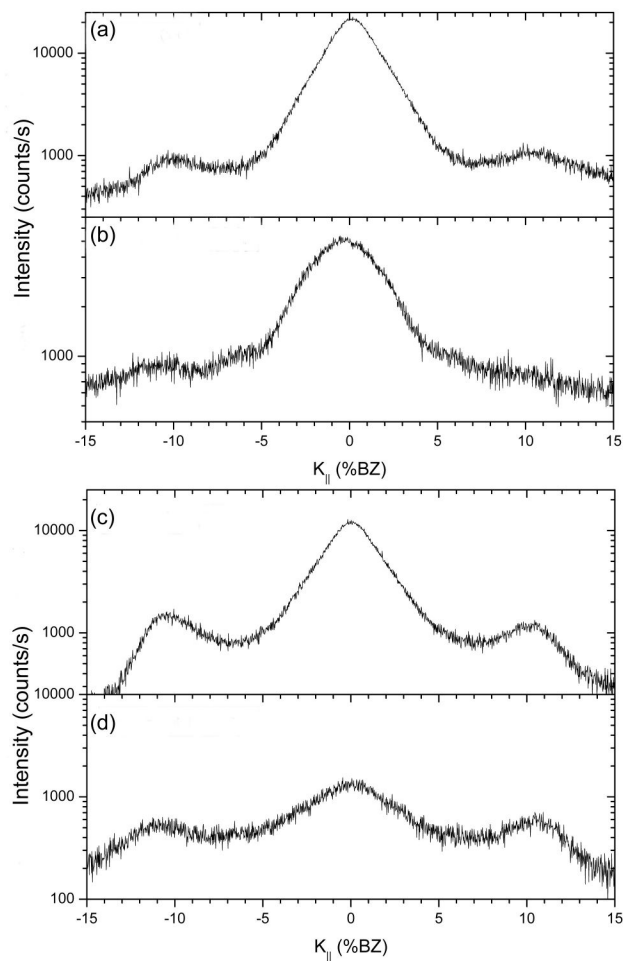


Figure 5: 1-D Scans along $[11\bar{2}]$ directions showing spot profiles of the corrugation spot close to (00) and the Pb spot near (10) . Spot positions are given in %BZ along the $[\bar{1}\bar{1}2]$ axis away from the maximum of intensity along the $[1\bar{1}0]$ axis (see text). Scans (a) and (b) show 1.2 ML deposited on the α -phase at 195 K, while scans (c) and (d) 1.9 ML deposited on the α -phase at 195 K. (a) Pb (10) intensity for “hexagon” pattern. (b) Corrugation intensity for “hexagon” pattern. (c) Pb (10) intensity for “star” pattern. (d) Corrugation intensity for “star” pattern.

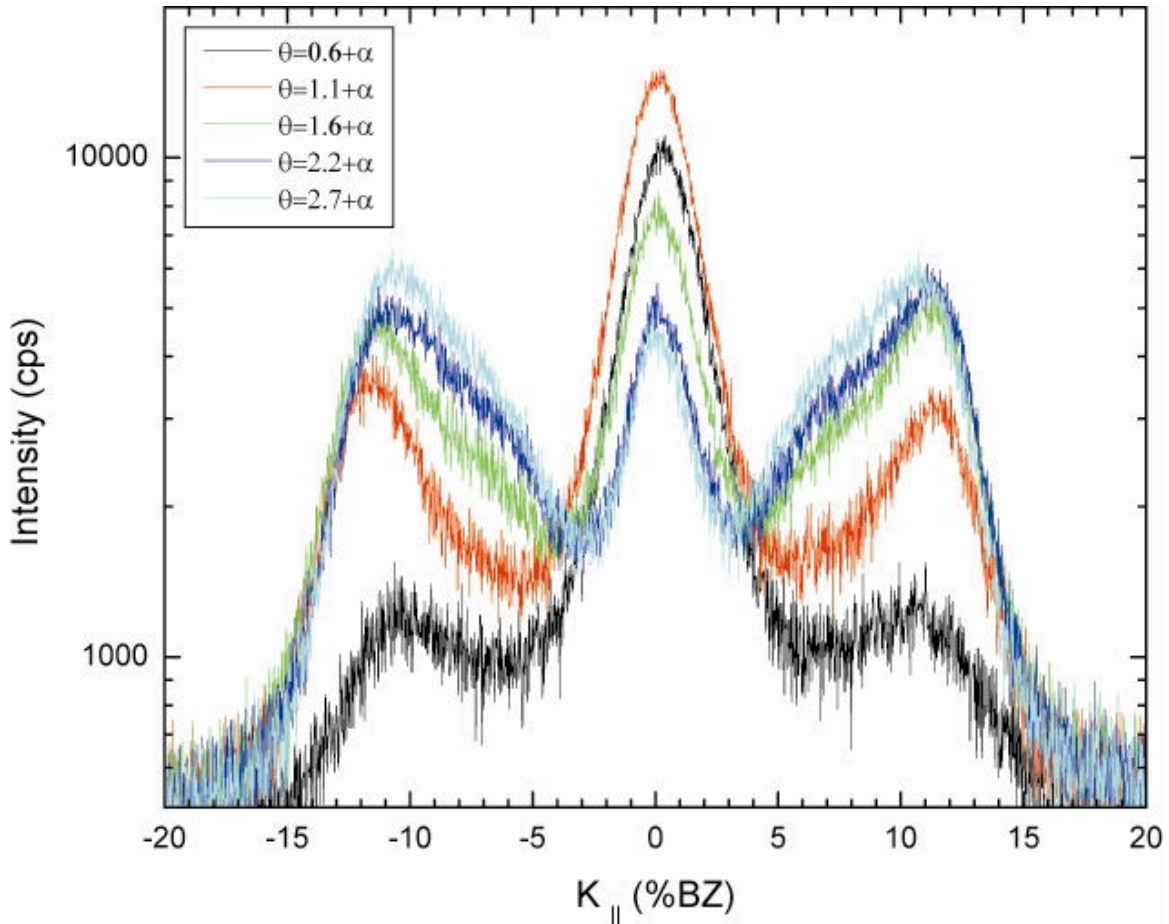


Figure 6: Evolution of Pb spot with coverage 0.6 ML – 2.7 ML on top of the α -phase at 195 K. 40% BZ scans taken along $[11\bar{2}]$ direction centered at the Pb spot maximum along the $[1\bar{1}0]$ direction. As coverage increases the intensity maximum changes from the non-rotated Pb islands to the rotated Pb islands as seen from the intensity ratios of the 0% and +/- 10 % Spots.

The evolution of the Pb spot cross section along the $[\bar{1}\bar{1}2]$ direction with coverage is shown in Figure 6. The evolution of island orientation with coverage can be seen by comparing the peak intensity of spots located near 0% BZ (non-rotated Pb layers) with spots located near 11% BZ (rotated overlayers). At the lowest coverage 0.6 ML where the Pb forms only nanoclusters and small 2 step Pb islands, the peak intensity of the aligned spot is approximately 8 times stronger than the peak intensities for the rotated spot. As the coverage increases, the ratio of the peak intensities of the non-rotated spot to the rotated spots decreases. At the highest coverage of 2.7 ML, the peak intensity of the rotated spots is approximately 50% higher than the non-rotated spot.

Discussion

In order to connect the orientation of the Pb lattice with the size and orientation of the island corrugation, we created a number of hard-ball models, each with a different relative orientation of the Pb lattice with respect to the silicon lattice. For these models we used lattice constants near the bulk values $a_0=3.5$ Å for Pb and $a_0=3.85$ Å for Si (3.85 Å is used instead of 3.84 Å to give an 11-10 Si/Pb ratio). This gives a unrotated Pb/Si coincidence length of 38.5 Å. We also created models using a compressed Pb lattice constant of $a_0=3.46$ Å and Si lattice constant $a_0=3.84$ Å (giving a 10-9 Si/Pb ratio). This is in agreement with the experimental LEED observation of the corrugation maximum occurring at 11.1% BZ and the experimental Pb(10) spot position of 111.6 ± 0.8 % BZ along the $[1\bar{1}0]$ direction, corresponding to a 3.44 ± 0.02 Å lattice. This maximum indicates that the corrugation along the $[1\bar{1}0]$ direction has cell length nine times the length of the Si 1x1 cell, or 34.6 Å.

Each angle of the rotation of the lead lattice produces different Moiré patterns. Since it is believed that these Moiré patterns are the source of the observed island corrugation, the observed corrugation should correspond to the beating periodicity between the two lattices. We expect that the beating periodicity and orientation should change as the orientation of the Pb lattice changes. The model only includes the beating between the first layer lead lattice and the Si lattice; for a rigid Pb lattice the positions of the atoms in the additional Pb layers follow the same beating periodicity. For each model we define the angle θ to be the rotation of the Pb lattice away from the $[1\bar{1}0]$ direction, We measure two quantities, an angle ϕ , which is the angle of rotation of the corrugation away from the $[1\bar{1}0]$ direction and the corrugation length, which is the average length between in-phase conditions of the Moiré pattern. These are determined by measuring the angle and distance between at least 6 in-phase conditions of the Moiré pattern for each model. We estimate the error to be ± 0.2 Å for the corrugation length and ± 1 degree for ϕ .

An example model is shown in Figure 7. Figure 7 shows the Pb lattice rotated by $\theta=9$ degrees with respect to the Si lattice. This example model is smaller than the actual models which were used for measurement. Figure 7 has a 10 x 10 Pb cell of length 38.5 Å, meaning

11 Pb lattice constants match 10 Si lattice constants. The unit cell is highlighted to show the orientation of the Pb lattice with respect to the silicon lattice. By visual inspection, one can see that the resulting Moiré pattern has a corrugation length which is roughly half the length of the Pb unit cell and is also oriented in a different direction than the Pb unit cell. More careful measurements reveal that the length of the beating period is 20.0 Å, and the angle ϕ of the beating period is 3.6° from the $[1\bar{1}0]$ axis in the direction of the Pb rotation.

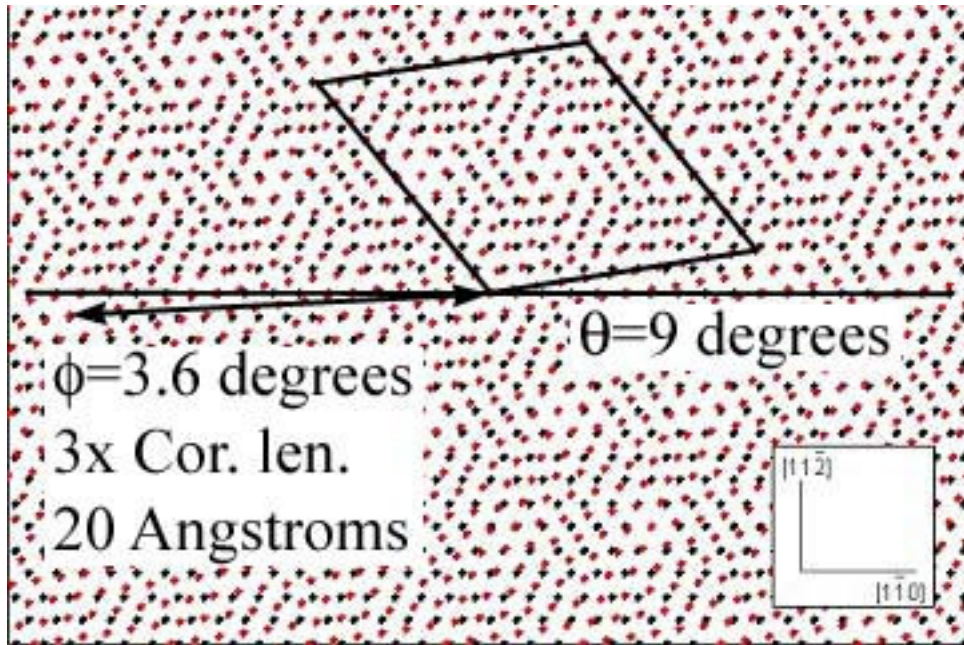


Figure 7: Model of rotated Pb island. This model shows the Pb 1 x 1 lattice rotated 9 degrees with respect to the underlying Si lattice. The corrugation distance and angle with respect to the silicon is measured using multiple in-phase conditions where the Pb and Si lattice positions are located the closest.

Similar measurements of the beating periodicity and direction of models were made with Pb lattice rotations of $0 < \theta < 12$ degrees at 1 degree intervals. Due to the symmetry of the Pb and Si lattice in the first layer, the results for positive and negative rotations of the Pb lattice yield the same results of beating length and angle, with opposite direction. For each model the distance between the corrugation and the angle of the corrugation with respect to the horizontal $[1\bar{1}0]$ axis were measured. The results are tabulated in Table 1 for both Pb unit cell sizes.

Table 1 shows the length of the corrugation and the angle of orientation away from the $[1\bar{1}0]$ lattice. Positive angle of corrugation ϕ is in the same direction as positive angle of Pb lattice rotation. Reciprocal space lengths were calculated using $|Q|=2\pi/a_0$, where $|Q|$ is the length of the lattice vector for each corrugation unit cell in reciprocal space and a_0 is the length of the beating period in the hard ball model. These values are then normalized to the Si Brillouin Zone, where $2\pi/a_{0Si}=100\%$ BZ, and $a_{0Si}=3.84 \text{ \AA}$. ϕ^* uses the six-fold symmetry of the system to give an equivalent rotation which shows that the angle of the corrugation is continuously increasing with increasing Pb rotation. For all rotations, the length in real space of the corrugation unit cell is longer for the 38.5 \AA model than the 34.6 \AA model.

11 Pb Unit cells					10 Pb Unit cells				
θ	Cor L	%BZ	ϕ	ϕ^*	θ	Cor L	%BZ	ϕ	ϕ^*
0	38.4	10.0	0.0	0.0	0	34.5	11.1	0.0	0.0
1	37.6	10.2	11.4	11.4	1	34.2	11.2	10.3	10.3
2	35.9	10.7	21.6	21.6	2	33.3	11.5	19.6	19.6
3	33.7	11.4	-29.6	30.4	3	30.8	12.4	27.3	27.3
4	30.9	12.4	-21.7	38.3	4	29.2	13.2	-24.1	35.9
5	28.6	13.4	-14.7	45.3	5	26.8	14.3	-18.0	42.0
6	25.8	14.9	-9.7	50.3	6	24.6	15.6	-11.8	48.2
7	24.0	16.0	-5.2	54.8	7	22.4	17.1	-6.9	53.1
8	21.7	17.7	0.0	60.0	8	20.9	18.4	-3.7	56.3
9	20.0	19.2	3.6	63.6	9	19.5	19.7	1.7	61.7
10	18.5	20.7	6.7	66.7	10	18.0	21.3	3.7	63.7
11	17.2	22.3	9.4	69.4	11	16.6	23.2	6.6	66.6
12	16.1	23.8	11.9	71.9	12	15.6	24.7	9.3	69.3

Table 1: Measurements done on hard ball rotated Pb models. Cor L refers to the average distance between in-phase conditions of the Moiré patterns in real space. %BZ converts this distance to a percentage of the silicon Brillouin Zone. Angle is the measured angle of the in phase conditions with respect to the $[1\bar{1}0]$ axis, and Ang* converts angle to a continuously increasing angle using the 6-fold symmetry. For details see text.

Figure 8 shows the results of model measurements in Table 1 for the 11-10 and 10-9 models. Figure 8 (a) shows the corrugation angle ϕ^* vs. lattice rotation θ . When the Pb and Si lattices are aligned the corrugation pattern is also along the $[1\bar{1}0]$ direction. As the lead lattice is rotated, the corrugation pattern rotates much more quickly. The 11 Si / 10 Pb corrugation pattern is always rotated more than the 10 Si / 9 Pb pattern. Figure 8(b) shows the corrugation length vs. lattice rotation θ . As the Pb lattice is rotated the length of the

corrugation pattern is reduced. As can be expected from the non-rotated corrugation lengths, the 11 Si / 10 Pb corrugation pattern always has a longer length than the 10 Si / 9 Pb pattern.

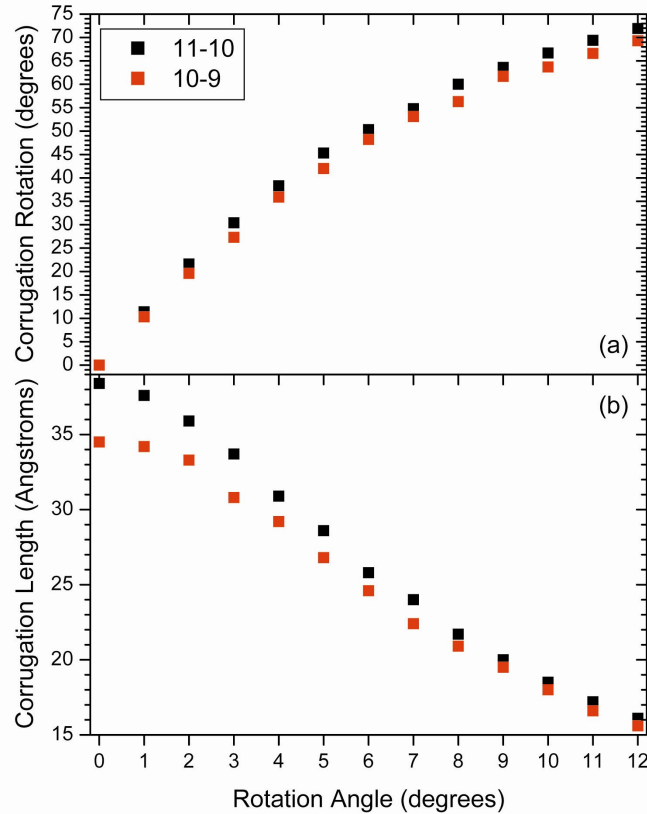


Figure 8: Results of model measurements for 11-10 and 10-9 models. (a) Corrugation angle ϕ vs. lattice rotation θ . (b) Corrugation length vs. lattice rotation θ . For each case, the rotation angle ϕ increases and the corrugation length decreases as the lattice rotation θ increases.

We want to compare the experimental diffraction results with the value expected from our models. The angle of each reciprocal space vector is the same as the angle of the real space orientation. In addition, each vector is rotated by 60, 120, 180, 240 and 300 degrees to account for the six-fold symmetry of the Si(111) and Pb(111) layers, and each vector is also inverted about the $[1\bar{1}0]$ axis to account for positive and negative Pb rotations. A uniform distribution is assumed such that each orientation gives the same intensity. This plot gives a

suggestion of the origin of the hexagon and star patterns. By limiting the allowed Pb rotation angles the hexagon and star patterns are reproduced. Figure 9(a) shows only the models with twists 0 to 3 degrees for the 10 and 11 Pb unit cell models. This reproduces the hexagon pattern. Figure 9(b) shows the vectors given by the models from 0 to 8 degrees for the 10 and 11 Pb unit cell models. This reproduces the star pattern. In all cases the diffraction pattern is smaller in reciprocal space for the 38.5 Å model than the 34.6 Å model. This is because in real space for all rotations, the length of the corrugation unit cell is longer in reciprocal space for the 38.5 Å model than the 34.6 Å model.

To determine whether the 11 Pb atom unit cell or 10 Pb unit cell should be used for all rotations, we compare the experimental measurement with the calculation. For islands which are not rotated the distance along the $[1_{-10}]$ direction is 11.1% BZ, corresponding to the 10 Pb atom model. For the twisted islands, we use the maximum intensity of the points of the star in the 1-dimensional scans. In reciprocal space, the maxima are located at $\phi=43 \pm 2^\circ$, ($\tan \phi = 10.5/11.0$), corrugation length 15.2 \pm 0.3% away from the maximum of the (00) spot intensity. According to our model these occur at a Pb twist of 5.6° . From the results of Table 1, the 38.4 Å models predict a corrugation length for 5.6° twisted islands of 14.3 % BZ and angle 49° . The 34.6 Å models predict a corrugation length of 15.1% BZ and angle 46° . Since the 34.6 Å is in better agreement with the experimental results for non-twisted and twisted islands, it appears that a compressed Pb lattice is favored for all observed Pb island orientations, consistent with the compressed Pb lattice constant derived from the Pb(10) spot position.

We can also use our models and the observed corrugation on the STM images to determine the lattice orientation of the islands in STM images. For Figure 3(a), the measured corrugations and angle ϕ were 3.5 nm and 4.5 degrees for the left inset and 3.6 nm and 5.4 degrees for the right inset. From our models the rotation angle θ is less than 1 degree for each case. This is consistent with the “hexagon” distribution observed from

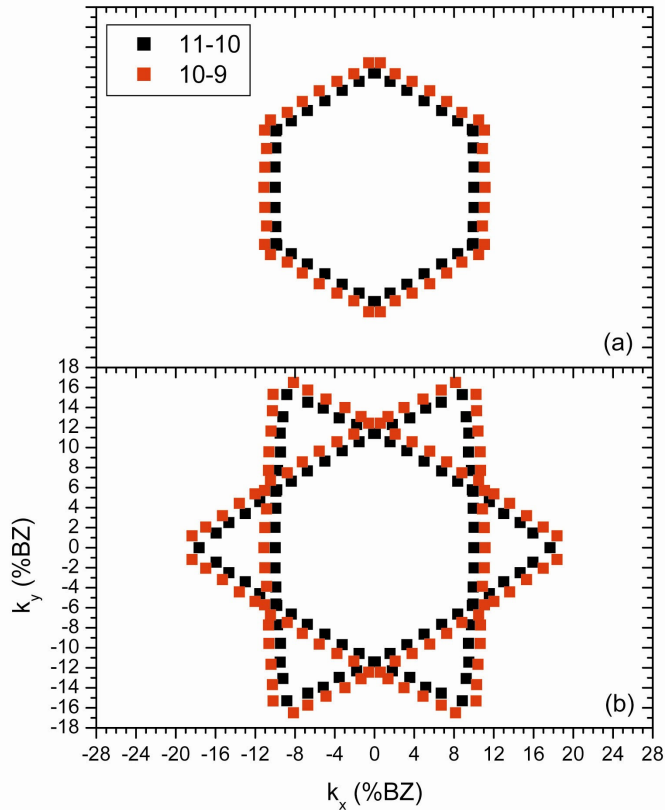


Figure 9: Reciprocal space lattice positions of the corrugation distance and angles with respect to the Si BZ. (a) Pb model rotations 0-3 degrees, reproducing the “hexagon” pattern. (b) Pb model rotations 0-8 degrees reproducing the star pattern.

the diffraction pattern. For Figure 3(b), the measured corrugations and angle ϕ were 2.9 nm and 24 degrees ($\phi^*=36$) for the left inset, 2.5 nm and 3.6 degrees ($\phi^*=56.4$) for the upper right inset and 3.5 nm and 0.5 degrees for the lower right inset. Since the direction of the Pb lattice rotation cannot be determined from the image, ϕ^* is estimated from the model. The corrugation patterns from figure 8(b) are consistent with lattice rotations θ of approximately 4, 6 and 0 degrees, respectively. Since two patterns show θ larger than 3 degrees, this is consistent with the “star” distribution.

The cause of rotation of the overlayers for many heteroepitaxial systems is the reduction of energy at the interface. The simplest explanation would be to look for a CSL between the Si(1x1) and Pb(1x1) substrate with rotation near 5.6° , as done in Bauer *et al* and

Weitering *et al.* [13,14] We performed calculations similar to the ones in these papers to determine if the CSL was a viable explanation for the overlayer rotation. The results of these calculations are shown in table 2.

10 and 9						
a1	a2	theta	dPb	nPb	strain	
9	0	0.00	10.00	10	0.00%	
4	1	10.89	5.09	5	1.84%	
7	2	12.22	9.09	9	1.05%	
3	1	13.90	4.01	4	0.15%	
5	2	16.10	6.94	7	-0.87%	
7	3	17.00	9.88	10	-1.24%	
2	1	19.11	2.94	3	-2.01%	
5	3	21.79	7.78	8	-2.78%	

Bulk Pb						
a1	a2	theta	dPb	nPb	strain	
10	0	0.00	10.97	11	-0.26%	
6	1	7.59	7.19	7	2.78%	
5	1	8.95	6.11	6	1.81%	
4	1	10.89	5.03	5	0.55%	
7	2	12.22	8.98	9	-0.22%	
3	1	13.90	3.96	4	-1.11%	
8	3	15.30	10.81	11	-1.77%	
5	2	16.10	6.85	7	-2.12%	
7	3	17.00	9.75	10	-2.48%	

Table 2: Possible CSL models derived from Si(1x1) and Pb(1x1) lattices. Two values are used for the lattice constant of Pb, 3.456 Å following the observed LEED values and 3.50 Å to match the bulk Pb value. In the table, a1 and a2 are the lattice vectors of silicon, theta is the rotation angle away from $[1\bar{1}0]$, dPb is the length of the CSL in lattice constants of Pb, and strain is the expansion or contraction necessary to achieve perfect coincidence. In each case the observed rotation of 5.6° is not allowed by the CSL model.

The calculations were done taking two lattice constants of Pb, 3.46 Å following the observed LEED corrugation value and 3.50 Å to match the bulk Pb value. In each case a Si lattice was created of size 10 x 10 and 11 x 11 to match the un-rotated CSL value. The distance from the origin to each lattice point and the angle of rotation from the $[1\bar{1}0]$ direction were calculated. The strain was calculated from this distance and the nearest multiple of the Pb lattice constant, using the formula $s=(d-a)/a$, where d is the distance between the Si lattice points and a is the lead lattice distance. If the strain is less than +/- 3%,

and the CSL length is less than the unrotated CSL length, the model is allowed and included in the table. For the smaller Pb value given by the diffraction patterns, the smallest allowed CSL rotation angle is 10.9° . For the 3.5 \AA lattice constant the smallest value is improved at 7.6° , but is still too large to explain the 5.6° rotation. Therefore this rotation cannot be explained by the simple CSL model with the 1×1 lattices of Pb and Si.

Different observed rotations of the Pb overlayers have been observed for different substrates. [27] The Pb lattice is also slightly compressed in the $[1\bar{1}0]$ plane such that a commensurate Moiré pattern is observed between the overlayer and substrate in both LEED and STM. Therefore, it would seem to indicate that the interface energy at the overlayer/substrate interface is a reasonable conclusion for the cause of the rotation this system. However, since the simple CSL model does not seem to work, to fully verify this conclusion advanced theoretical calculations of the strain energy with respect to island size and rotation are required. If promising results are found, the rotation and compression of Pb islands may provide additional tunable parameters for QSE driven nanostructure growth.

Conclusions

A change in the rotation of Pb islands relative to the Si substrate with increasing coverage has been observed for Pb islands grown on the Pb/Si(111) α -phase. The Pb lattice is also slightly compressed in the (111) plane with respect to the bulk value. For lower Pb coverage the $[1\bar{1}0]$ axis of the islands is most often aligned with the $[1\bar{1}0]$ axis of the substrate. At higher Pb coverage the islands coalesce and form a bilayer with additional islands grown on top of the bilayer. At this coverage the islands prefer a rotation of 5.6° relative to the substrate.

References

- [1] K. Budde, E. Abram, V. Yeh, M.C. Tringides, *Phys. Rev. B* **61**, R10602 (2000)
- [2] V. Yeh, L. Berbil-Bautista, C.Z. Wang, K.M. Ho, M.C. Tringides, *Phys. Rev. Lett.* **85**, 5158 (2000)
- [3] M. Hupalo, V. Yeh, L. Berbil-Bautista, S. Kremmer, E. Abram, M.C. Tringides, *Phys. Rev. B* **64**, 155307 (2001)

- [4] M. Hupalo, S. Kremmer, V. Yeh, L. Berbil-Bautista, E. Abram, M.C. Tringides, *Surf. Sci.* **493**, 526 (2001)
- [5] C.M. Wei and M.Y. Chou, *Phys. Rev. B* **66**, 233406 (2002)
- [6] E. Ogando, N. Zabala, E.V. Chulkov, M.J. Puska, *Phys. Rev. B* **69**, 153410 (2004)
- [7] W.B. Jian, W.B. Su, C.S. Chang and T.T. Tsong, *Phys. Rev. Lett.* **90**, 196603 (2003)
- [8] M. Hupalo, V. Yeh, T.L. Chan, C.Z. Wang, K.M. Ho and M.C. Tringides, *Phys. Rev. B* **71**, 193408 (2005)
- [9] I.B. Altfeder, D.M. Chen, K.A. Mateev, *Phys. Rev. Lett.* **80**, 4895 (1998)
- [10] I.B. Altfeder, V. Narayanamurti, D.M. Chen, *Phys. Rev. Lett.* **88**, 206801 (2002)
- [11] T.L. Chan, C.Z. Wang, M. Hupalo, M.C. Tringides, W.C. Lu, K.M. Ho (submitted)
- [12] H.Y. Lin, Y.P. Chiu, L.W. Huang, Y.W. Chen, T.Y. Fu, C.S. Chang, T.T. Tsong, *Phys. Rev. Lett.* **94**, 136101 (2005)
- [13] H.H. Weitering, D.R. Heslinga, T. Hibma, *Phys. Rev. B* **45**, 5991 (1992)
- [14] S. Stepanovskyy, V. Yeh, M. Hupalo, M.C. Tringides, *Surf. Sci.* **515**, 187 (2002)
- [15] P.B. Howes, K.A. Edwards, D.J. Hughes, J.E. Macdonald, T. Hibma, T. Bootsma, M.A. James, *Phys. Rev. B* **51**, 17740 (1995)
- [16] K.A. Edwards, P.B. Howes, J.E. Macdonald, T. Hibma, T. Bootsma, M.A. James, *Surf. Sci.* **424**, 169 (1999)
- [17] E. Bauer and J. H. van der Merwe, *Phys. Rev. B* **33**, 3657 (1986)
- [18] A. Trampert, K.H. Ploog, *Cryst. Reg. Technol.* **35**, 793 (2000)
- [19] F. Gray and J. Bohr, in *Phase Transitions in Surface Films 2*, ed. H. Taub (Plenum, New York, 1991)
- [20] C. G. Shaw, S. C. Fain, Jr., and M. D. Chinn, *Phys. Rev. Lett.* **41**, 955 (1978)
- [21] J.S. Tsay, C.S. Shern, *Surf. Sci.* **396**, 319 (2000)
- [22] H. Zajonz, D. Gibbs, A.P. Baddorf, V. Janz, D.M. Zehner, *Surf. Sci.* **447**, L141 (2000)
- [23] H.C. Galloway, P. Sautet, M. Salmeron, *Phys. Rev. B* **54**, R11145 (1996)
- [24] J.K. Bording, B.Q. Li, Y.F. Shi, J.-M. Zuo, *Phys. Rev. Lett.* **90**, 226104 (2003)
- [25] B.Q. Li, J.-M. Zuo, *Surf. Sci.* **520**, 7 (2002)
- [26] M. Hupalo and M.C. Tringides, *Phys. Rev. B* **65**, 205406 (2002)

[27] V. Yeh *et al* (unpublished)

CHAPTER 7: UNUSUAL TEMPERATURE STABILITY OF PB NANOWIRES GROWN ON SI(111)-IN(4x1) PHASE

M. Yakes¹, J. Chen², M. Hupalo³, M.C. Tringides⁴

(Based on a paper submitted to *Applied Physics Letters*)

Introduction

In order to fully utilize the potential of self-assembled nanostructures, it will be important to generate methods to create structures that have uniform size and geometry. A physical phenomenon that has great promise as a tool in assembling uniform structures is the electronic growth of structures due to the quantum size effect (QSE). [1] An outstanding example of the QSE is the growth of uniform height Pb islands on the Si(111) substrate. [2,3] Many physical properties of these Pb films in addition to the stability temperature have been shown to oscillate in bilayer increments with increasing film thickness. [4]

The Si(111)/In(4x1) reconstruction forms long chains which run along the [110] direction, with separation between the chains of 13.3 Å. [5] Recently Pb islands which have been grown on the anisotropic Si(111)/In(4x1) reconstruction have been shown to exhibit preferred width in one lateral direction as well as in the direction normal to the surface. The preferred geometry in the lateral direction is believed to be derived from strain driven growth due to the anisotropic substrate. These preferred geometries yield the growth of Pb nanowires on the surface which have preferred height and width and variable length. [6]

The composition of the interface is known to have many affects on both the growth morphology and physical properties of QSE driven nanostructures. Islands which were grown on the Si(111)/Pb($\sqrt{3} \times \sqrt{3}$)- β phase have been shown to have different preferred heights to islands grown on the Si(111)-7x7 reconstruction. [7,8] Also, uniform thin films of Pb grown Si(111)/Pb($\sqrt{3} \times \sqrt{3}$)- β , Si(111)/In($\sqrt{3} \times \sqrt{3}$)- β and Si(111)/Au(6x6) have been

¹ Graduate Student, primary researcher and author for correspondence

² Graduate Student, participated in LEED experiments

³ Staff Scientist, conducted STM experiments

⁴ Professor

shown with photoemission to have different transition temperatures their quantum well states. [9]

Pb islands with QSE driven electronic growth are metastable, i.e. undergo an irreversible transition to roughened films upon annealing above a transition temperature which depends on the coverage and film morphology. An obstacle to be overcome if these films are to be used in technological applications is increasing the temperature range in which these QSE islands are stable. Pb islands grown on Si and Pb/Si alloy interfaces have shown a maximum transition temperature of 250 K. It has already been shown that the critical temperature can be increased with the addition of oxygen on top of already grown islands. [10] It is believed that the oxygen atoms present on the surface increase the kinetic barriers for the Pb atoms within the island to escape. Also, as mentioned above uniform Pb films grown on Si surfaces reconstructed with other metals such as In and Au have shown changes in the transition temperature with respect to Pb/Si alloy interfaces, including T_c 's greater than 300 K. This change in T_c is thought to be thermodynamically based due to an altering of the phase of the confined electrons due to the change in the metal/semiconductor interface.

In this paper, we examine the thermal stability of Pb nanowires formed on the Si(111)/In(4x1) substrate using STM and diffraction. We discuss how these islands differ from previously examined Pb islands on Si or Pb/Si substrates, namely the structure of the wetting layer and the anisotropy in island size.

Experiment

Experiments took place in two separate UHV chambers with base pressure 2×10^{-11} Torr. One chamber is equipped with an Omicron SPA-LEED system, Auger spectrometer and mass spectrometer. The other chamber was equipped with an Omicron variable temperature STM and a conventional LEED system. In each experiment the starting point was the Si(111) 7×7 phase. This sample was prepared by flashing the crystal to 1250° C, then cooling the crystal to the temperature of the 7×7 reconstruction. The In (4x1) reconstruction was obtained by depositing 1 ML In and annealing to 400°C. In the STM experiments 2.5-3 ML of Pb was deposited at 0.2ML/min to form Pb islands. For the SPA-

LEED experiments, the sample was cooled to 185 K for Pb island deposition and scanning. Approximately 3.2 ML Pb at approximately 0.1 ML/min was deposited on the 4x1 at this temperature to form islands. After deposition the sample was cooled to 120 K (LT). After experiments were done the crystal was annealed to 215 K, 242 K, 265 K and 285 K. Each anneal took approximately 10 minutes and after annealing the sample was again cooled to LT to freeze in the island configuration and reduce coarsening. At each temperature a 2-D scan at 38 eV of the (00) spot, a 240 % BZ 1-D scan at 38 eV and a 40% scans of the (00) profile along [110] at 40-75 eV (for the g(s) curves) were taken.

Results

Figure 1 shows STM images taken at 185 K. Figure 1(a) shows a 105 nm x 105 nm image of 2.5 ML of Pb grown on In(4x1) at 185 K. In addition to Pb nanowires the 2-layer wetting layer is seen between the islands. The second layer is seen to be incomplete, with trenches that descend to the first lead layer. The average separation between islands in this image is approximately 170 Å along the $[\bar{1}\bar{1}2]$ direction as determined by an autocorrelation function of the STM image. The preferred width of these islands is 66.5 Angstroms or approximately 5 times the width along the $[\bar{1}\bar{1}2]$ direction of the 4x1 substrate. These islands have a preferred height of two Pb layers above the 2-layer Pb wetting layer, or 4 layers total.

Figure 1(b) shows a 200 nm x 200 nm image the surface seen in figure 1(a) after overnight RT anneal. The width of the islands in figure 1(b) is the result of a triple STM tip. While this tip creates difficulty in measuring the lateral size, the height information and separation between islands is preserved. Figure 1(c) shows a 1-D scan along the direction of the line in figure 1(b). The uniform height of the islands of 9 Å can clearly be seen, and this height can be verified as three Pb layers above the wetting layer by comparing with the Si step height of 3 Å. This marks a change in the island morphology from the low temperature growth. The top layer of Pb has been removed from the wetting layer, leaving three layers of the Pb nanowires exposed. Using an autocorrelation function for images taken after the room temperature anneal, the average separation between islands is determined to be approximately 840 Å.

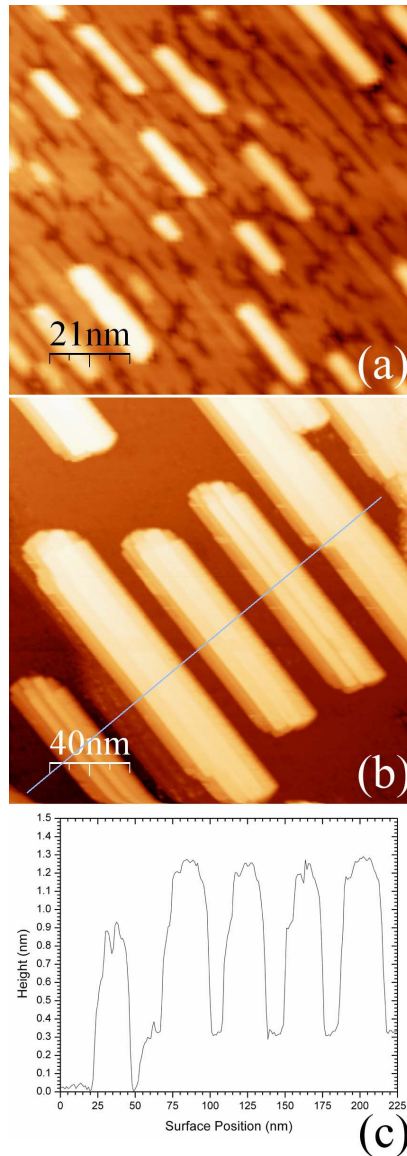


Figure 1: (a) 105 x 105 nm image showing 2.5 ML of Pb deposited on the Si(111)-In(4x1) phase. 4 step nanowires are present separated by a two layer wetting layer. (b) 200 nm x 200 nm scan of surface (a) after anneal to room temperature. “Ghosts” of each island indicate a multiple STM tip, however the 4-layer preferred height is still visible. (c) 1-D scan of STM image along direction indicated in (b) Comparison with the Si step height confirms single layer wetting layer and 4 layer islands at room temperature.

Figure 2 shows 40% x 40% silicon Brillouin Zone (BZ) 2-D scans around the (00) spot. The temperature of each scan is labeled in the figure. There are 6 “arms” which radiate from the specular beam along the $[1\bar{1}0]$ directions. These arms come from the anisotropic separation between the Pb islands. In the STM images in Figure 1, the separation between

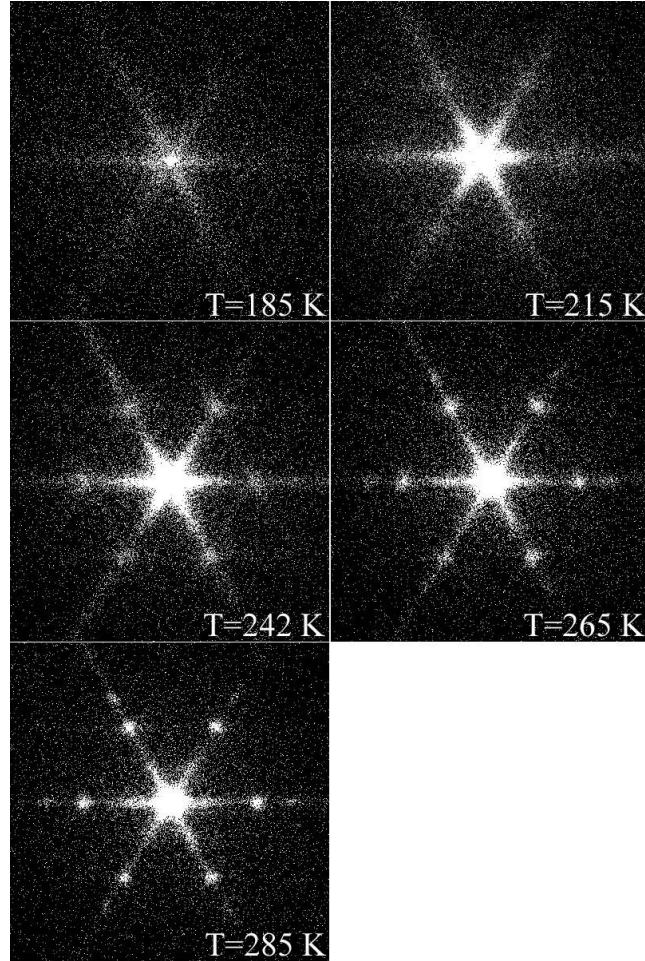


Figure 2: 40% x 40% BZ images at 5 increasing annealing temperatures. Arms caused by anisotropic island separation are visible for all temperatures, but reduce in length with increasing temperature. Corrugation spots are visible at 11% and 14% BZ along horizontal ($[110]$) direction for high temperatures.

islands across the short $[1\bar{1}0]$ axis of the nanowires is less than the separation along the long direction. Since the size of the ring around the (00) spot increases with decreasing island separation, the arms radiate along the direction with short separation. The three-fold symmetry of the $\text{Si}(111)$ surface and the three possible directions of the growth of the $\text{In}(4\times 1)$ chains gives the 6 arms seen in the diffraction pattern. As the temperature increases, the intensity of the arms increases and the length of the arms decrease. For increasing temperature there are strong spots near 11% and weaker spots near 15% along the $[110]$ direction.

Figure 3 shows 120% BZ scans along the [110] direction for each temperature shown in Figure 2. There are a number of notable features seen in the 1-D scans. As in Figure 2, as temperature increases the intensity of all spots increase, however the relative intensity of the (00) spot to the 4x1 spots stays roughly constant. The In 4x1 spot profiles change with increasing temperature. At T=185 K the spots appear to be sharp with no satellite. However, when comparing the satellite intensity of the (00) spot with the intensity of the 4x1 spots any satellite intensity would be buried in the background. At T=215 K and T=242 K, each fractional order spot has a satellite spot on either side of it. For all temperatures the splitting of the 4x1 spot matches the splitting of the (00) spot. This is most clearly seen in comparing the 4x1 spot splitting at 242 K in the figure with the measured k_1 of the (00) spot. For each 4x1 spot and for the specular beam, the maximum of each satellite spot is 2.1% away from the primary spot. At T=265 K and 285 K the spots appear much wider than at lower temperatures. This means that the satellite spots are now close to the instrumental limit of 0.5% BZ and can only be seen as an increase of width for the 4x1 spots.

As in the 2-D patterns, there are two additional spots which do not belong to the 4x1 reconstruction, one near 10% and one near 14%. The relative intensity of these spots with respect to the 00 spot does not change as temperature is increased; all the spots in the diffraction pattern get progressively stronger with temperature. The 10% spot can be explained by the lattice mismatch between the Pb(111) lattice (3.5 Å) and the In(4x1) lattice (3.84 Å) along the [110] direction. The 15% spot corresponds with a second periodicity in the corrugation pattern observed in STM of 27 Å. This periodicity is observed in a [110] direction which is not along the grooves formed by the 4x1 reconstruction. [6] This periodicity cannot be explained by a simple lattice mismatch argument between the In 4x1 unit cell (15.36 Å along the [110] direction) and the Pb(111) unit cell and must come from some other periodicity.

Using SPA-LEED, when the terrace width is comparable to the transfer width of the instrument, the surface morphology can be investigated using $g(s)$ curves. The spot profile contains two components, a sharp peak arising from long range order on the surface and a broad component which arises from the separation between islands. The intensity of each

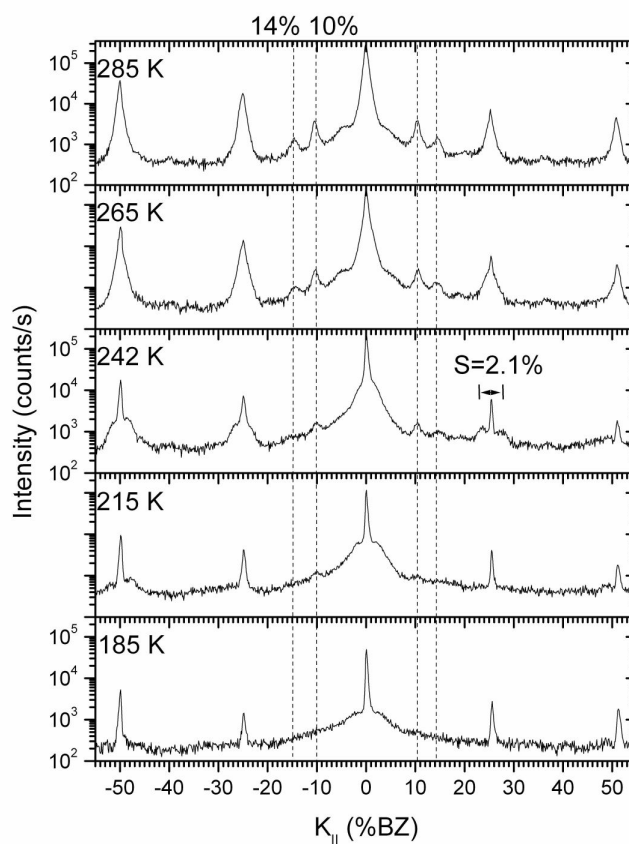


Figure 3: 240% scan along [110] direction for increasing annealing temperature. The 4x1 spots appear split at $T=215$ K and 242 K due to the two layer system. Corrugation spots at 10% and 14% are clearly visible.

component depends on the electron beam energy, so varying the energy can give information about the surface morphology. The $g(s)$ curve is derived from the normalized intensity of the sharp and broad components of the (00) peak as a function of normalized momentum transfer ($s=K_n/(2\pi/d)$), where K_n is the normal component of the momentum transfer). When the electron energy is in phase such that the electron wavelength is some multiple of $\frac{1}{2}$ the separation from the island tops to the layer underneath, the ratio will be at its maximum. When the electron energy is out of phase the ration will be at a minimum. Therefore, the period of the oscillations of the $g(s)$ curve is inversely proportional to the island height.

Figure 4 shows the $g(s)$ curves for all 5 temperatures. In each case the 4 fold oscillations are clearly seen. The distance between the maxima and minima are $\frac{1}{4}$ of the

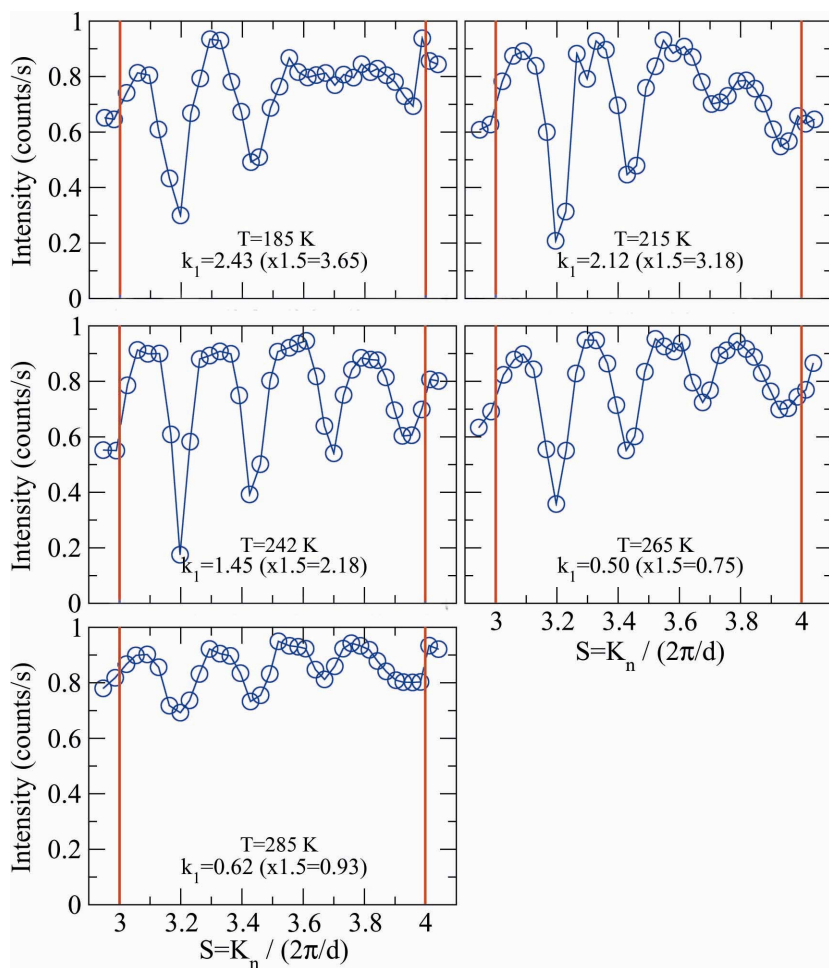


Figure 4: $G(s)$ curves taken for 3 ML coverage on the Si(111)-In(4x1) phase with increasing coverage. The oscillation period of $0.25 S$ indicates that the height difference in the two layer system is 4 layers at all temperatures. Changing values for k_1 show that the average size of the islands is increasing with increasing temperature.

single unit of normalized momentum transfer. At the lowest temperature the last two oscillations are suppressed. As the beam energy increases above 60 eV (3.6 in the units of normalized momentum transfer) the specular beam intensity is very low, less than 1000 cps as compared to greater than 10^5 cps for other energies and temperatures. The low (00) beam intensity causes the results of the $g(s)$ curve to be unreliable; for this curve the section between 3.0 and 3.5 will be more reliable in determining the island heights. At 215 K and 242 K the oscillations are very strong, and then get weaker as temperature is increased to 265 K and 285 K, though the oscillations are still clearly seen at the highest temperature both in the $g(s)$ curve and the specular width (σ_0) profiles which are not shown. This indicates that

the average separation of the islands is less than 0.5% BZ, or greater than 700 Å in real space.

The fourfold oscillation curves mean that the two reflecting surfaces for electrons are the island tops and the 4x1 interface. This is different from islands grown on the 7x7 or β phases, where the reflecting surfaces are the island tops and the top of the wetting layer. This indicates that the structure of the wetting layer is different from the structure of the wetting layers in these systems. Earlier STM results show that the 1st Pb layer follows the 4x1 periodicity, then the second Pb layer forms single layer islands two times this periodicity. Phase boundaries between these double wide rows result in single layer trenches being formed in the second layer.

Figure 5(a) shows a 61 nm x 59 nm image of the wetting layer at 185 K after the formation of Pb islands. The wetting layer is two Pb layers thick and forms single layer grooves along the [110] direction following the 4x1 substrate. Using the autocorrelation function one can determine the average separation of the grooves in the [112] direction. The autocorrelation function of the STM image taken in figure 5(a) is shown in figure 5(b). Taking the autocorrelation function of multiple images of the wetting layer gives the average groove separation to be 51 Å. Figure 2(c) shows a diffraction pattern taken at 185 K after deposition of 2 ML Pb. At this coverage the Pb(10) spots which indicate crystal formation are not observed in the 2-D diffraction pattern, indicating that the structure of the wetting layer is amorphous. The 4x1 spots appear to have weak satellites located 7.8% BZ away from the fractional order 4x1 peaks. Since the wetting layer follows the periodicity of the underlying substrate these splittings are a result of the two level system formed by the wetting layer and the 1 layer trench underneath. The 7.8 % splitting is in agreement with the 7.5% BZ value expected from the observed STM trench separation of 51 Å.

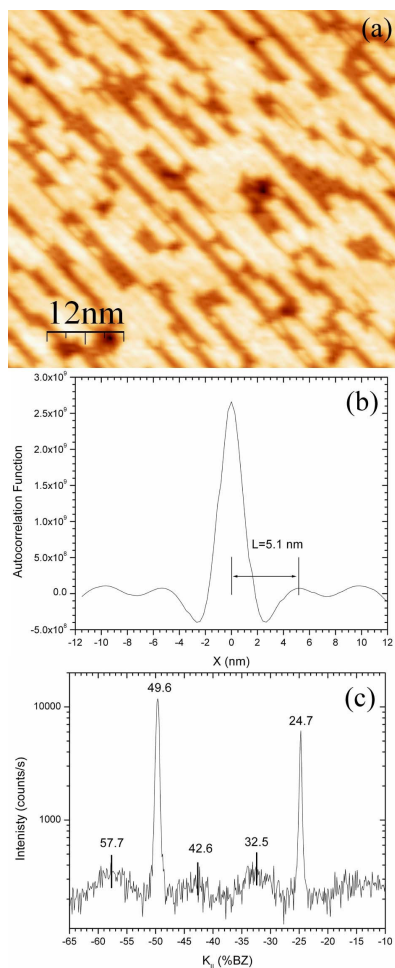


Figure 5: (a) 61 nm x 59 nm image of the 2-layer wetting layer. Trenches reaching down into the first layer are visible as dark lines in the pattern. (b) Autocorrelation function of the STM image in figure (a) showing the average trench separation of 51 Å. (c) 55% BZ scan showing 7.5% splitting of 4×1 spots in 1-D diffraction pattern, in excellent agreement with 51 Å splitting seen in STM.

Discussion

It is well known that changing the substrate that QSE driven thin films are grown on adjusts the properties of the thin films. For Pb islands grown on Si(111) 7×7 or Si(111) β -phase, the highest temperatures where preferred heights are observed is 250 K. For Pb grown of the 7×7 these islands are 7 layers high while for the Pb they are 5 layers high. For layer by layer growth of Pb on different substrates, the maximum critical temperatures for the film depended strongly on the material used for the reconstruction of the substrate. Films grown on Si(111)/Pb($\sqrt{3} \times \sqrt{3}$)- β had a maximum T_c of 250 K for 6 layer thick films. The

critical temperature of the 6 layer film is consistent with the critical temperature of 6-layer islands (wetting layer + 5 additional Pb layers) grown on Si(111)/Pb($\sqrt{3} \times \sqrt{3}$)- β phase. Films grown on Si(111)/Au(6x6) had a higher maximum T_c of 320 K for 6 layer films. For Pb grown on Si(111)/In($\sqrt{3} \times \sqrt{3}$)- β phase the maximum T_c was 250 K, nearly the same as for Pb, however, this is for 8 layer films. From the photoemission data there is no expectation that In would cause the increase in T_c for the films.

It is unclear what is the cause of the increased stability of the islands grown on the In(4x1) reconstruction. In the uniform films grown in Ref. [9], the change in stability temperature was attributed to a phase shift in the QSE oscillations due to the changing boundary conditions at the interface. Increased temperature stability for the Pb islands can also be achieved by depositing oxygen gas on top of already grown Pb islands. [10] This increased stability is believed to be caused by the oxygen increasing the kinetic barrier for atoms to leave the island tops. The anisotropic shape of the Pb nanowires is believed to be caused by a change in the kinetic barriers for Pb atoms on the surface due to anisotropic strain on the surface. If this strain also influences the kinetic barriers on the island tops this could also lead to an increased stability of the Pb islands. However since the separation between islands increases with increasing temperature, this indicates that there is substantial coarsening occurring, which means that the thermodynamic contribution is the likely cause for the increased stability.

Figure 6 shows a 25 nm x 22 nm STM image of the wetting layer at 185 K after annealing to room temperature. The surface is in the same condition as the high temperature islands in Figure 1(b). The 2nd layer seen in figure 5(a) at low temperature has been removed from the wetting layer as well as the trenches. The remaining Pb layer follows the 4x1 periodicity. The distance between dark lines on the STM image is 14 Å, consistent with the 13.6 Å distance of the 4x1 unit cell along the [112] direction. This results in two Pb layers being exposed at T=185 K, while three Pb layers are exposed after room temperature anneal as in figure 1. Since the $g(s)$ curves shown in figure 4 show 4 oscillations within one period of the normalized momentum transfer, it is measuring the distance from the island tops to the

island interface, and is not sensitive to the wetting layer either above or below the wetting layer transition.

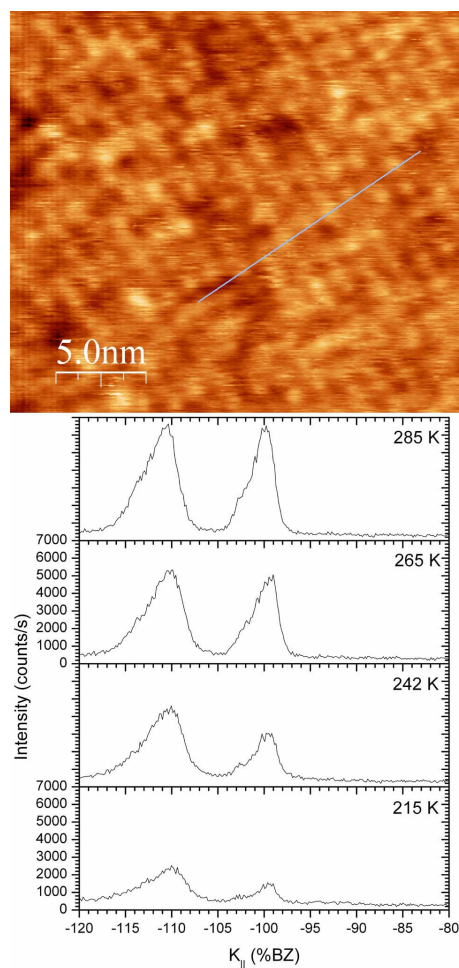


Figure 6: (top) 25 nm x 22 nm STM image showing wetting layer after annealing to room temperature. There is no longer evidence of trenches along the $[110]$ direction. (bottom) 40% BZ scan of the $(1,0)$ 4×1 spot during annealing. Increased intensity of the $(1,0)$ 4×1 spot (at 100% BZ) with respect to the $\text{Pb}(1,0)$ spot (at 110% BZ) indicate that the periodicity of the wetting layer is increasing, as would be expected with a thinner wetting layer.

The $\text{Pb}(1,0)$ spot at 110% BZ and the $\text{Si}(1,0)$ spot at 100% BZ in diffraction are also shown in Figure 6 after various temperature anneals. Since the periodicity of the first and second layers follow the periodicity of the 4×1 substrate, no additional spots from the wetting layer are observed in diffraction. However, we see evidence of the wetting layer transition

by looking at the relative intensity of the two spots with increasing temperature. While the overall intensity of all spots is increasing, the relative intensity of all of the 4×1 spots increase with respect to the Pb spot with increasing temperature. At $T=215$ and 242 K, the intensity of the Si (1,0) spot is roughly half of the Pb(1,0) spot, while at 265 and 285 K, the two spots have roughly equal intensity. This indicates that as the temperature increases more of the first layer, which has the same periodicity as the substrate, is being exposed. This results in increased intensity of the 4×1 spots. This leads to interesting and unsolved questions about the structure of the Pb wetting layer, and its effect on the temperature stability of the Pb nanowires.

Conclusions

Pb nanowires of uniform height and preferred thickness have been grown on the Si(111)/In(4×1) reconstruction. These islands have been shown with STM and SPA-LEED to have increased temperature stability as compared to Pb islands grown on other substrates. 4-layer islands have been shown with STM and SPA-LEED to maintain their stability after annealing to 285 K. As the temperature increases, the separation between islands decreases. The wetting layer has been studied in detail, showing different morphology as the temperature is increased. At 185 K, the wetting layer is two layers thick, with trenches along the $[110]$ direction that descend to the first Pb layer. The absence of Pb spots indicates that the structure of the wetting layer is amorphous. As the temperature increases, the second layer is removed and only the first layer remains.

References

- [1] Z. Zhang, Q. Niu, C.-K. Shih, *Phys. Rev. Lett.*, **80**, 5381 (1998)
- [2] K. Budde, E. Abram, V. Yeh, M.C. Tringides, *Phys. Rev. B*, **61**, 10602 (2000)
- [3] S.H. Chang, W.B. Su, W.B. Jian, C.S. Chang, L.J. Chen, T.T. Tsong, *Phys. Rev. B*, **65**, 245401 (2002)
- [4] C.M. Wei and M.Y. Chou, *Phys. Rev. B*, **66**, 233408 (2002)
- [5] S. Mizuno, Y.O. Mizuno, and H. Tochiohara, *Phys. Rev. B*, **67**, 195410 (2003)
- [6] M. Hupalo and M.C. Tringides, *Phys. Rev. B*, **73**, 041405 (2006)

- [7] V. Yeh, L. Berbil-Bautista, C.Z. Wang, K.M. Ho and M.C. Tringides, *Phys. Rev. Lett.*, **85**, 5158 (2000)
- [8] M. Hupalo, V. Yeh, L. Berbil-Bautista, S. Kremmer, E. Abram and M.C. Tringides, *Phys. Rev. B*, **64**, 155307 (2001)
- [9] D.A. Ricci, T. Miller, T.-C. Chiang, *Phys. Rev. B*, **95**, 266101 (2005)
- [10] S. Stepanovskyy, V. Yeh, M. Hupalo, M.C. Tringides, *Surf. Sci.*, **515**, 187 (2002)

CHAPTER 8: CONCLUSIONS

An important goal in present day surface science is to grow uniform sized self-assembled nanostructures. One system which has displayed a number of interesting surface structures is Pb grown on a Si(111) substrate. The first part of the thesis discusses the “Devil’s Staircase” (DS) of linear phases studied with Scanning Tunneling Microscopy (STM) and Spot-Profile Analysis Low Energy Electron Diffraction (SPA-LEED). The DS is one of the outstanding predictions in theoretical physics and is expected to exist in systems with two competing interactions. At low temperatures (<120 K) over 15 different DS phases can be observed by small Pb depositions (<0.01 ML). In addition, a DS phase diagram with the transition temperatures of the DS phases, a family of hexagonal phases and a meandering phase. The second part of the thesis explores multiple structural features of uniform height Pb nanocrystals on Pb and In induced reconstructions of Si(111) using SPA-LEED and STM. Pb islands grown on these substrates grow with preferred heights due to the Quantum Size Effect (QSE). Pb islands of 2 and 4 layer height were grown on the Pb- $\alpha(\sqrt{3}\times\sqrt{3})$ phase. The observed corrugation pattern on the island tops revealed the rotation of the Pb crystals with respect to the silicon substrates. Also, using the two types of corrugation patterns (arising from the two equivalent fcc stacking sequences of Pb(111) crystals) were used to determine the population of each stacking sequence with changing Pb coverage. At coverage 1 ML, the islands were preferentially aligned in the opposite stacking sequence as the Si substrate, while at higher coverages the islands were preferentially aligned with the Si substrate. Finally, Pb islands were grown on the anisotropic Si(111)-In(4x1) substrate. In addition to a preferred height of 4 ML, these islands grow as nanowires with a preferred width of 66 Å as a result of strain driven growth from the anisotropic substrate. Islands grown on the In(4x1) substrate also retain their preferred height to room temperature in contrast to previously observed stability temperatures of 250 K or less for islands grown on other substrates. This is important because it has implications on the role of the substrate in determining the changing stability with island height of the Pb nanostructures.

Although we've learned a great deal about the interesting physics in the Pb/Si(111) system, there are still many unanswered questions. As mentioned in the DS chapters, the phase diagram outlined in Chapter 4 is not well understood. There is no adequate explanation for the shift in preferred binding site between the phases with coverage $\theta < 1.25$ ML and $\theta > 1.25$ ML. Intuitively one would expect the transition temperature of the DS phases to depend on the period of the phase, or alternatively on the length of the stair in the $\Delta\mu$ vs. θ plot shown in the introduction. However the observed U-shaped transition temperature of the phase diagram in Chapter 4 clearly counters this expectation. This could be related to the transition to the hexagonal phases, but it is unknown. It is also not understood why only certain hexagonal phases are observed out of all the possible phases of the same geometries.

There are also a number of outstanding questions related to the Pb islands grown on various substrates. Clearly the change in stacking sequence and change in rotation minimize the energy in the sample, but why these effects happen at coverages near 2 monolayers is an open question. For the nanowires, it is unknown why the magic width of 66.5 Angstroms is preferred, or what causes the increased temperature stability of these islands. Is it the indium substrate itself or is it related to the magic width? Clearly there is no danger of running out of things to explore in more detail anytime soon.

In a longer view, we are taking baby steps on the path to the larger goal of designer self-assembled nanostructures. This is a formidable task which I do not expect to be fully achieved in the near future. However, it is certainly a goal worth pursuing and I am very confident that some of the lessons we have learned will make a contribution to achieving this lofty goal.

ACKNOWLEDGEMENTS

There have been very few times in my life when I have had a good opportunity to thank all the people that have helped me achieve any success that I have had. I think that I have had more than my fair share. I have been extremely fortunate to have been influenced by so many wonderful people along the way.

To list the contributions of all the great teachers I have had in my life would require a separate thesis. Of the many excellent ones I've had Joe Huntley, Dave Hartwig, Greg Carlson, David Landry, Bob Dennison, John Brandenberger, David Cook, Jeff Collett, Matt Stoneking, Andrew Zangwill, and Ed Conrad have probably been the most influential, though I am sure that this list is not exhaustive.

I have been privileged to work with many outstanding scientists during my time at Iowa State. Myron Hupalo has been a great source of guidance for me when I have had troubles ranging from an angry SPA-LEED machine to navigating the job waters. We have had a very nice collaboration with Zdenek Chvoj and Zdenka Kuntova from the Czech Academy of Science. Some of my favorite grad school memories are discussing problems with them over lunches. Jizhou Chen spent hours listening to me talk out my crazy ideas for how to explain many of the results in this thesis, and he always offered good suggestions. Vincent Yeh basically taught me everything I know about the SPA-LEED, and I thank him for many fruitful discussions. One thing I never suspected before entering graduate school was that your advisor is about a million times more important to your grad school experience than which school you end up choosing. The single best decision I made in graduate school was to join Michael Tringides group. Michael is not only an accomplished scientist and an infinite source of new ideas but also one of the nicest people I have ever met.

Any success I have had or am going to have in my career and my life is a direct reflection on my family. Any failures are on me. I could not imagine a more supportive set of parents than my mom and dad, Ramona and Jim. I also have two wonderful sisters, Erin and Kellie, who I am extremely proud of. It is amazing to know that there are two such great people that I know I can always count on. I also have a fantastic extended family which now

includes an adopted family which I picked up about the time I started doing the work in this thesis. This adopted family comes from my beautiful and brilliant wife Betsy. Graduate school and life have been quite an adventure, and I am very happy that we can take it together.